Assessing the role of surface electric fields on the interfacial degradation in silicon solar cells

Donghao Liu

A Thesis Presented for the degree of

Doctor of Philosophy

Supervised by Professor R S Bonilla and Dr Matthew Wright

St Catherine's College

University of Oxford

October 2024

Abstract

Enhancing the reliability and longevity of solar modules is critical for expanding solar power to a multi-terawatt scale target worldwide. A major problem in maintaining high efficiency is the recombination of the photoexcited charge carriers at different interfaces. Within industrial silicon solar cells, there are three main device architectures in actual use: passivated emitter and rear cell (PERC), tunnel oxide passivated contact solar cells (TOPCon), and silicon heterojunction solar cells (SHJ). All these architectures suffer from different instabilities of efficiencies under prolonged illumination. This work investigates the mechanisms involved in interface-related degradation in these three architectures, specifically associated with hydrogen in silicon, especially considering the effects of surface electric fields.

Through the current-voltage measurement for the PERC and TOPCon cells during bias annealing, I have shown the first bias-controlled hydrogen-induced contact resistance change in TOPCon cells. I demonstrate that the degradation occurs purely at the n-type Si / Ag interface on both cell architectures.

Through the application of the surface electric fields on TOPCon and SHJ lifetime specimens during light soaking, I show that light-induced instabilities can be varied by the polarity and strength of the surface polarisation on the dielectric layer. Here, I demonstrate that the charged hydrogen ions, which respond readily to electric fields, are responsible for these observed instabilities. In addition, three mechanistic models are proposed to explain the hydrogen dynamics in these advanced solar cell architectures with surface polarisation.

This work contributes to the body of evidence aimed at understanding hydrogen kinetics at different interfaces and providing valuable insights into the mechanisms behind these light-induced instabilities of these architectures. Besides that, applying surface electric fields via the corona charge or direct bias shows a potential method for detecting and controlling the kinetics of hydrogen in actual PV systems.

Preface

This thesis is an account of the work I have carried out as a postgraduate student at the Department of Materials, University of Oxford. I have not previously submitted any part of this thesis for a degree at this University or elsewhere. The work of other authors is duly acknowledged in the text, and appropriate references are given.

During the course of this thesis, I have written or contributed towards the following publications:

1. **Donghao Liu**, Mohsen Goodarzi, Joshua Deru, Peter R. Wilshaw, Phillip Hamer, Ruy Sebastian Bonilla; Investigating the link between LeTID and hydrogen-induced contact resistance in PERC devices. *AIP Conf. Proc.* 24 August 2022; 2487 (1): 130008. https://doi.org/10.1063/5.0089337
2. **Donghao Liu**, Matthew Wright, Mohsen Goodarzi, Peter R. Wilshaw, Phillip Hamer, R.S. Bonilla, Observations of contact resistance in TOPCon and PERC solar cells, Solar Energy Materials and Solar Cells, 246 (2022) 111934. https://doi.org/10.1016/j.solmat.2022.111934
3. **Donghao Liu**, Matthew Wright, Brendan Wright, Pietro P Altermatt, Phillip Hamer, Ruy S. Bonilla, The Impact of Surface Polarisation on the Degradation of Tunnel Oxide Passivating Contacts in Silicon Solar Cells. Solar Energy Materials and Solar Cells 282 (2025): 113340. https://doi.org/10.1016/j.solmat.2024.113340

Acknowledgements

During the whole DPhil study, I was highly fortunate to be part of this talented team. This thesis would not be possible without the huge support from the whole group. I want to thank my supervisor Ruy Sebastian Bonilla firstly. He not only helped me find the research direction but also gave me confidence with his constant affirmation and encouragement. I also want to thank my co-supervisor Matthew Wright for helping me in building the experiment and developing such an engaging thesis. Both of them are highly knowledgeable and patient to share their wisdom with me. I would also like to thank Radka Chakalova for all the assistance in cleanroom processing in Begbroke. I would also like to thank Professor Peter Wilshaw for welcoming me to the group for the first year. Besides that, I want to show my appreciation to the other team members: Shona McNab, Eleanor Shaw, Mingzhe Yu, Xinya Niu, Yifu Shi, John O'Sullivan, Jingyan Chen, Anastasia Soeriyadi, Mohsen Goodarzi, Phillip Hamer and all the Part II students for providing their great insights and help for this work. Thanks to my friends, Zheng Zhang, Peng Tang, Xiaonan Luo, Taobo Hao, Xuewei Li, Chengyu Ji, Yuxuan Wang, Yixuan Li and all other friends, you guys gave me a highly wonderful life in the UK for these years. Last but most importantly, a huge amount of appreciation goes to my father Qi Liu and my mother Hongmei Li for their great support and love.

List of acronyms and abbreviations

AlO_x	Aluminium Oxide
a-Si	amorphous silicon
BSF	Back surface field
c-Si	crystalline silicon
CB	Conduction band
Cz	Czochralski, referring to one of the silicon casting processes.
EFID	Electric field induced degradation
FEP	Field-effect passivation.
FF	fill factor
FZ	Float Zone, referring to one of the silicon casting processes.
HICR	Hydrogen induced contact resistance
IV	Current-voltage
KP	Kelvin Probe
LID	Light induced degradation
LeTID	Light and elevated temperature degradation
mc	multi-crystalline, referring to a kind of raw silicon material.
PECVD	Plasma enhanced chemical vapour deposition.
PL	Photoluminescence
PERC	Passivated emitter and rear cell
POLO	Polysilicon on oxide
RIE	Reactive Ion Etching
sccm	standard centimetre cubed per minute, flow unit.
SiN_x	Silicon nitride, refers to the non-stoichiometric form of this dielectric film
SiO_x	Silicon oxide, refers to the non-stoichiometric form of this dielectric film
SHJ	Silicon heterojunction solar cells
SRD	Surface-related degradation
TOPCon	Tunnel oxide passivated contact solar cells
TLM	Transmission line method

List of symbols

T	Temperature [°C] or [K]
D_{it}	Density of interface states ($cm^{-2}eV^{-1}$)
η	Efficiency (%)
n_0, p_0	Electron (hole) concentration at thermal equilibrium (cm^{-3})
n_i	Intrinsic carrier concentration (cm^{-3})
Δn,Δp	Excess electron (hole) concentration (cm^{-3})
V_{OC}	Open circuit voltage (V)
J_0	Surface recombination current density (fA/cm^2)
τ_{eff}	Effective minority carrier lifetime (ms) or (μs)
R_S	series resistance ($\Omega \cdot cm^2$)
R_c	contact resistance (Ω)
ϕ_B	Schottky Barrier Height [eV]
ϕ_F	Fermi Energy [eV]

List of Figures

Table of contents

Chapter 1 Introduction

1.1 The Demand for Global Renewable Energy

The growth of population and the development of technology have led to the great energy demand for human beings. The world population is predicted to increase to 9.8 billion in 2050 and 11.2 billion in 2100 [1]. With the increase in population, world energy consumption will increase 48% from 2012 to 2040 [2]. According to the Statistical Review of World Energy 2023 report by the Energy Institute [3], fossil fuels remain the main energy source, with oil, coal and natural gas contributing 31.57%, 23.49% and 26.73%, respectively, of the total consumption in 2022, due to their low cost and mature technology. The extraction and use of fossil fuels will cause significant damage to the natural environment, such as ecosystem damage and groundwater contamination [4, 5]. The energy reserve for these fossil fuels is limited and these resources would run out in about 100 years [6]. Additionally, the emission of CO_2 and CH_4 from fossil fuel usage will exacerbate the greenhouse effect and thermal pollution [7]. One way to solve these problems is to conduct a global energy transition from fossil fuels to sustainable energy. As shown in Figure 1, nuclear energy, hydroelectricity and renewable energy share the rest of the global primary energy consumption market. Nuclear energy shows great potential, but it needs stringent control in the actual use and disposal of radioactive waste. Hydroelectricity is geographically restricted. Among all the renewable energy sources, solar energy has no risk of depletion. It is environmentally friendly and thus shows great potential to meet the needs of humans in the future. Besides that, it has good potential for aerospace applications and mature production processes. It is highly plausible that solar energy will become the dominant sustainable energy supply source in the future.

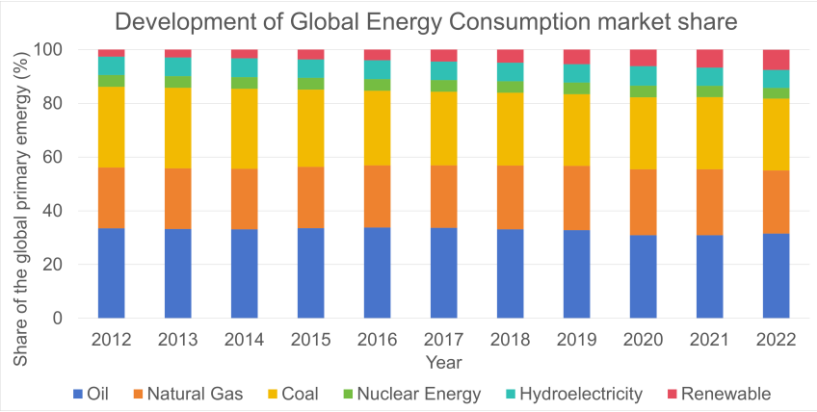

Figure 1. Development of world energy consumption based on Energy Institute data [3].

1.2 Photovoltaic Technology

Since the birth of the first practical silicon solar cells in 1954, photovoltaic cell technology has gone through enormous development [8]. The single junction solar cells can be divided into three types: Crystalline silicon cells, Thin-film technologies and Emerging photovoltaic. The first type is based on silicon, and the main application is the centralised photovoltaic power stations. Figure 2 shows the development of the crystalline silicon solar based on the record efficiencies achieved in lab-scale devices. The silicon technology is the most mature and currently dominates the market. The details of this kind of cell will be discussed in the following chapter. The second type Thin-film technologies use compound semiconductors (such as CdTe and CuInGaSe) to form the junction part. Compared with silicon solar cell, thin film solar cell can tolerate a higher defect density than Si-based [9]. However, in practical applications, the photoelectric conversion efficiency is lower than that of crystalline silicon, and their cost is expensive relative to Si. The use of rare earth elements and toxic materials to form the junction leads to high costs and environmental pollution. Although it has a better tolerance for defects, the fundamental material limits it for large-scale application [10]. The development of better and cheaper solar technology has progressed to the exploitation of Emerging photovoltaic, which introduces organic semiconductors and nanotechnology into fabrication techniques to reduce the cost. Perovskite solar cells were discovered in this wave of innovation and demonstrated a rapid increase in energy conversion efficiency, rising from 3.8% in 2009 [11] to 26.41% in 2024 [12]. Perovskite solar cells have the advantages of fast efficiency improvement, low cost, and material designability. However, the stability of Perovskite cells is poor, and this cell can quickly decompose under humid and light conditions, which would reduce the efficiency of the device [13, 14]. Currently, the stability level of max power point for perovskite solar cells is generally several thousand hours. In contrast, the service life of crystalline silicon solar cells is 20 to 25 years [15, 16]. Silicon solar cell is the best choice for meeting the actual demand for the energy in the future. Although lots of work have been focused on development of high efficiency crystalline silicon solar cells with different structures [17, 18], the degradation in these architectures is the factor affecting the service life of the solar cells in actual use. Therefore, studying the mechanism of degradation in these architectures is important to keep cells with high efficiency in long time use.

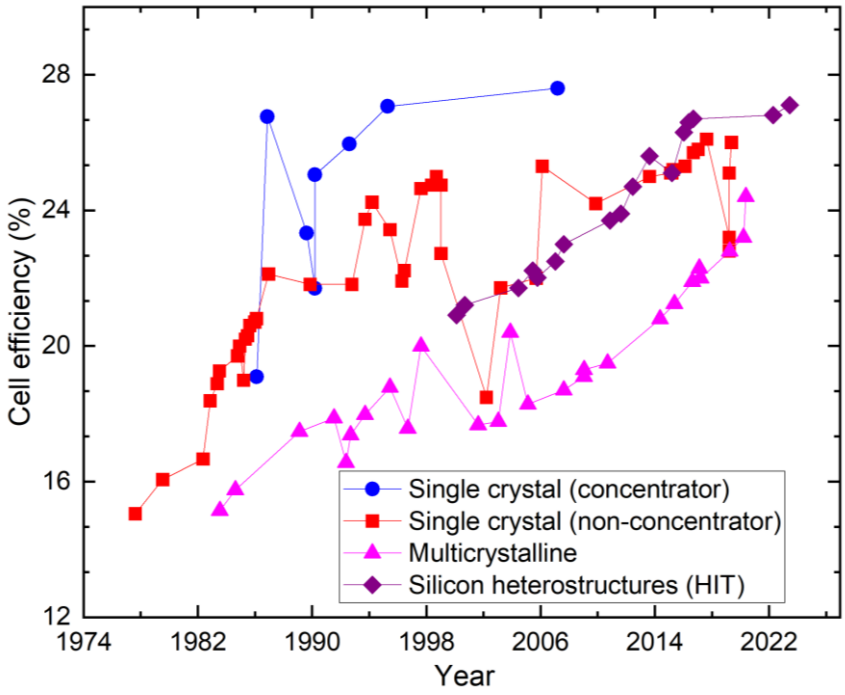

Figure 2. Development of best research Crystalline Si solar cells efficiency on NREL data [18].

1.3 Hydrogen in silicon solar cells

Although many potential materials can absorb sunlight in a solar cell, the photovoltaics market is entirely dominated by silicon. Thus far, silicon solar cells are the only proven technology to facilitate large-scale production (> 100 GW / year) at low cost [19, 20]. Within industrial silicon solar cells, there are three main device architectures: passivated emitter and rear cell (PERC), tunnel oxide passivated contact (TOPCon) solar cells, and silicon heterojunction (SHJ). In 2023, these architectures represented 70%, 15% and 7% of the total market, respectively [21]. Common to all structures is the incorporation of atomic hydrogen for passivating defects. In PERC and TOPCon structures, hydrogen is incorporated by depositing hydrogen-containing dielectrics, such as SiN_X or AlO_X, and firing at high temperatures [22-24]. Following firing, hydrogen moves from the dielectric to passivate defects either at the crystalline silicon surface or inside the bulk silicon material. In SHJ cells, hydrogen is incorporated by hydrogenated amorphous silicon layers, cured at temperatures < 300 ℃ [25, 26] . Although hydrogen is critical for passivating defects, it can also cause undesirable recombination [27].

The three aforementioned silicon cell structures display different characteristics under the influence of illumination and elevated temperature. Hydrogen is believed to play a critical role in all three. In the PERC

structure, high-temperature illumination induces a bulk degradation effect called light and elevated temperature degradation (LeTID) [28]. Although the exact mechanism causing this degradation is not fully understood, mounting evidence suggests that the recombination is caused by an excess of hydrogen in the silicon bulk [29, 30].

Under similar illumination and elevated temperature conditions, several reports have demonstrated deterioration in the surface passivation of lifetime structures using the TOPCon architecture. TOPCon cells include a thin tunnelling SiO_X deposited on top of the Si absorber, which is then capped by an n+ doped poly-Si serving as the electron collector, and a SiN_X layer used both for hydrogenation and antireflection. This degradation, unlike the LeTID bulk defects, manifests as a surface degradation [31-33]. Mounting evidence has suggested that this degradation correlates with an accumulation of hydrogen at or near the interface with the c-Si [34].

In the third leading cell architecture, SHJ, exposure to extended illumination can cause an increase in efficiency [35-37]. Rather than surface or bulk degradation, the carrier generation from illumination can lead to improved surface passivation [38], which leads to an increase in cell V_{OC}. The current hypothesis to explain this phenomenon is a migration of hydrogen ions in the a-Si to the interface to passivate defects. Therefore, the movement of hydrogen at or near the surface, as well as into the bulk, can lead to light-induced instabilities in all these three main industrial silicon cell architectures. Although mounting evidence can infer the involvement of hydrogen, in all three cases, there remains ambiguity about the exact nature of hydrogen involvement and the underlying mechanisms.

1.4 Aim of this thesis

This thesis aims to study the involvement of hydrogen in various light-induced instability modes in silicon solar cells by applying surface electric fields. Specifically, I have studied this phenomenon in three distinct components critical to the operation of silicon cell architectures:

1. Contact resistance changes in PERC and TOPCon solar cells.
2. Surface-related degradation in TOPCon lifetime structures.
3. Light-induced enhancements in SHJ lifetime structures.

In all cases, degradation is studied in the presence of a surface electric field, either induced by an applied bias in a cell architecture or surface corona charge in a lifetime structure. The applied field helps gain insights into the involvement of hydrogen ions in the aforementioned degradation modes.

1.5 Structure of this thesis

The structure of this thesis is as follows. Chapter 2 provides an overview of the commercial silicon solar cells and interface-related degradation observed in PERC, TOPCon and SHJ architectures. Chapter 3 describes the experiment methods used in the project, including the procedures for the sample preparation and characterisation method employed. Chapter 4 demonstrates that hydrogen induced contact resistance (HICR) changes are observed in both PERC and TOPCon solar cells linked to hydrogen dynamics at the interface. Through the modification of the PERC cell, a new current measurement pathway is created to isolate the impact of the contact resistance change from the different cell components during bias annealing. HICR in both PERC and TOPCon solar cells is attributed to increased contact resistance between the Ag contact and the n-type silicon. Furthermore, a comprehensive model of the kinetics of hydrogen in PERC cells with applied bias is presented here. Chapter 5 demonstrates the impact of surface polarisation, induced by corona charging, on the firing-induced surface-related degradation (SRD) of thin oxide / n+ doped poly-Si passivating schemes. The electric field at the surface during light soaking can accelerate the deterioration seen in the surface passivation of fired samples, most likely through the migration of hydrogen ions. Chapter 6 proposes a new approach to studying the role of hydrogen in light-soaking enhancement in SHJ cells. Applying surface electric fields via the corona charge method can provide insights into the role of hydrogen in the observed light soaking enhancement. Chapter 7 draws conclusions from all previous chapters and suggests future works to deepen and exploit the understanding provided by this work.

Chapter 2 Literature Review

Degradation in silicon solar cells has been long evidenced in industrial and research settings. Studying the mechanism behind these degradations is essential to maintain cell efficiency and thus boost the deployment of solar energy. This chapter provides an overview of the commercial silicon-based solar cells and interface-related instabilities observed in industrial solar cell architectures. It also provides background information about the involvement of hydrogen in these degradation modes.

2.1 Silicon solar cell working principles

The working principle underpinning all silicon cell architectures is the photovoltaic effect. Figure 3 shows the schematic of the structure and band diagram of the silicon solar cell under illumination. When photons with energy larger than the silicon band gap (1.12 eV at 300K [39]) are absorbed, electrons are excited from the valance band to the conduction band and leave a positively charged counterpart (hole) in the valence band, forming an electron-hole pair. This process is called generation. The mobile excited electrons and the generated holes will generate the current inside the cell. However, without the presence of a driving force, the generated electrons and holes diffuse randomly inside the cell and can recombine before they can be extracted. Recombination refers to the opposite process than generation, where energy is lost due to the electron giving their gained energy to another process (heat or light). The recombination of electrons and holes hence reduces the solar cell energy conversion efficiency. To output power requires the generated electrons and holes to be separated and collected at metal contacts, which is achieved through the p-n junction in silicon cells. N-type silicon is doped with elements with 5 valence electrons, such as phosphorus, to introduce excess free electrons at room temperature, while p-type silicon is doped with elements with 3 valence electrons, such as boron or gallium, to introduce excess free holes at room temperature. When the two types of silicon are contacted together, a p-n junction is formed. Due to the doping concentration gradient at the junction, a built-in voltage is formed and stops the majority carriers from crossing and allows the collection of minority carriers instead. The photo-generated minority carrier will drift across the p-n junction and get extracted to the external circuit.

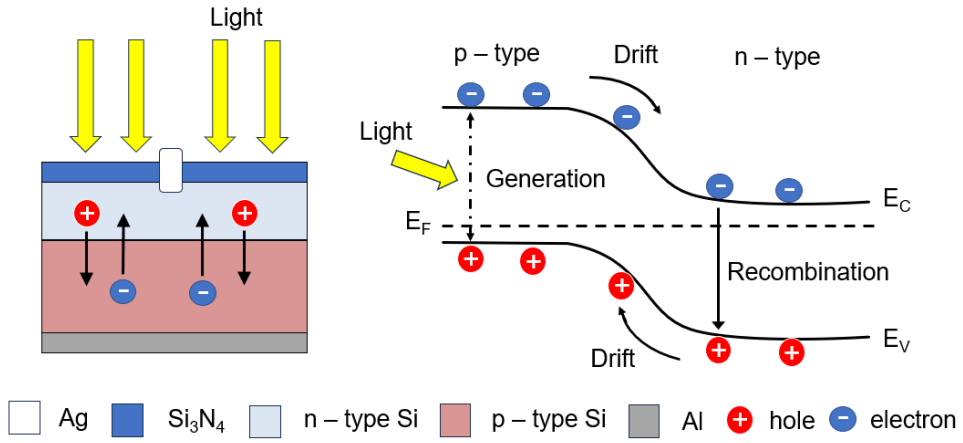

Figure 3. Schematic of structure and energy band diagram of silicon solar cell under illumination, including the generation and migration of electrons and holes across the junction.

2.2 Carrier recombination in silicon solar cells

Recombination describes the process in which electrons lose energy. When Si is under equilibrium conditions, without any injection of carriers, the generation rate G is equal to the recombination of carrier rate R, so the net recombination rate (U):

$$U = R - G = 0 \tag{2.1}$$

At thermal equilibrium conditions the product of the concentration of the holes and electrons is equal to the square of the intrinsic carrier concentration n_i .

$$n_0 p_0 = {n_i}^2 \tag{2.2}$$

Where n_i is a fundament property describing the number of electrons in the conduction band of the undoped silicon. The equilibrium concentration of the electrons and holes are n_0 and p_0 respectively. In doped silicon the concentration of the dopants exceeds n_i, and the carrier concentration is calculated as:

$$n_0 = N_D, \quad p_0 = \frac{{n_i}^2}{n_0} \quad (\text{n} - \text{type silicon}) \tag{2.3a}$$

$$p_0 = N_A, \quad n_0 = \frac{{n_i}^2}{p_0} \quad (\text{p} - \text{type silicon}) \tag{2.3b}$$

where N_D is the donor dopant concentration and N_A is the acceptor dopant concentration.

When photons with sufficient energy impinge onto the silicon, $G \neq R$ and excess carriers are generated. The total electron (n) and hole concentration (p) are:

$$n = n_0 + \Delta n\,, \quad p = p_0 + \Delta p \tag{2.4}$$

where Δn and Δp indicate the concentration of the excess generated electrons and holes respectively. The electron and hole are generated as a pair at the same time through the injected photon, so $\Delta n = \Delta p$. Once there is no extra energy to excite the electrons, excess carriers are in the metastable state and will diffuse and recombine again. The average time for the existence of these carriers is termed the carrier lifetime (τ) and calculated as:

$$\tau_{n-type} = \frac{\Delta p}{U}, \qquad \tau_{p-type} = \frac{\Delta n}{U} \tag{2.5}$$

The carrier lifetime is used to evaluate the net recombination, and it is related to the average distance travelled before the recombination as:

$$L = \sqrt{D\tau} \tag{2.6}$$

where L is the minority carrier diffusion length and D is the minority carrier diffusion coefficient. To achieve high-efficiency solar cells, it is essential to maximise the diffusion length. The recombination mechanisms can occur in different parts of the cell. The effective lifetime can be calculated from both the bulk and surface components in a solar cell. Thus the effective lifetime (τ_{eff}) is given by:

$$\frac{1}{\tau_{eff}} = \frac{1}{\tau_{bulk}} + \frac{1}{\tau_{surface}} \tag{2.7}$$

where τ_{bulk} and $\tau_{surface}$ are the lifetime dependence only on the bulk and surface as discussed in following sections.

2.2.1 Bulk Recombination

Bulk recombination can be intrinsic, which is a process independent of extrinsic material properties, and it includes Auger and Radiative recombination. It can also be an extrinsic process caused by the impurities or defects inside the crystal structure, defined by the Shockley-Read-Hall (SRH) recombination [40]. The total bulk lifetime is the sum of these three independent rates and can be expressed as:

$$\frac{1}{\tau_{bulk}} = \frac{1}{\tau_{rad}} + \frac{1}{\tau_{Aug}} + \frac{1}{\tau_{SRH}} \tag{2.8}$$

Figure 4 shows the schematic of these three types of bulk recombination and their mechanisms are discussed in the following.

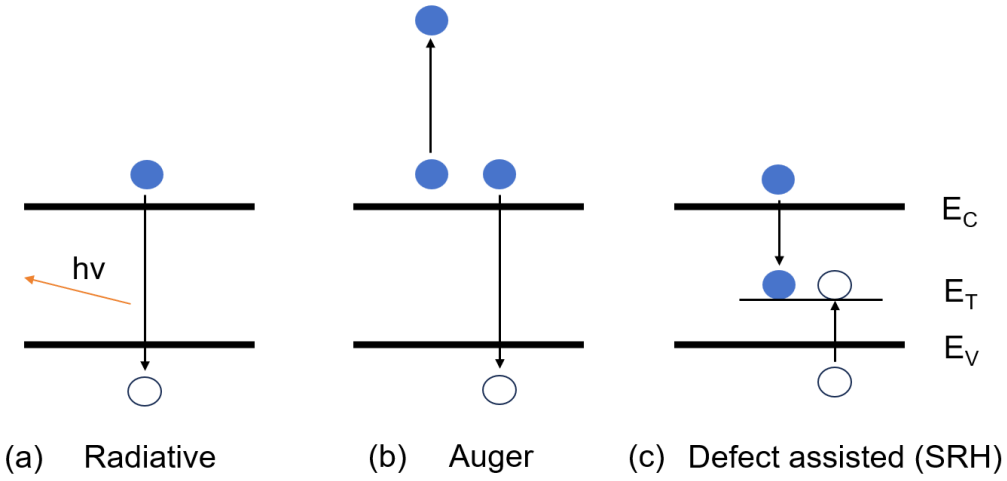

Figure 4. Schematic of (a) Radiative, (b) Auger and (c) SRH recombination. E_C is the conduction band and E_V is the valence band, while E_T is the trap state. Blue circles represent the electrons, and the white circles represent the holes.

2.2.2 Radiative Recombination

Radiative recombination occurs when the electron from the conduction band directly meets a hole at the valence band and the released energy is emitted as a photon. The net radiative recombination rate is given as [41]:

$$U_{rad} = B_{rad}(np - {n_i}^2) \tag{2.9}$$

Where B_{rad} is the radiative recombination coefficient, which is carrier density-independent and specific to the material. The minority carrier radiative lifetime is given as:

$$\frac{1}{\tau_{rad}} = \frac{1}{B_{rad}(n_0 + p_0 + \Delta p)} \tag{2.10}$$

Radiative recombination dominates in the direct band gap materials, but is of less importance in the indirect bandgap materials such as silicon [41]. In indirect band gap silicon, the electron needs the participation of a phonon to transform its momentum to the maximum of the valence band state, due to the difference in k-space. Due to the low radiative efficiency in silicon caused by the indirect gap, Auger recombination dominates the intrinsic recombination process, and thus has a greater impact on the practical limits of silicon.

2.2.3 Auger Recombination

Auger recombination is a three-particle process which includes the collision between the two similar carriers. When the electron at the conduction band combines with the hole in valence band, the released energy

is transmitted to either an electron in the conduction band or the neighbouring hole in the valence band, instead of generating a photon. The Auger recombination rate is proportional to the density of all three carriers. It can be divided into two processes: an electron and two holes (ehh) and a hole and two electron (eeh) process. The net Auger recombination rate is defined by the sum of these processes:

$$U_{Aug} = C_p(np^2 - n_0{p_0}^2) + C_n(n^2p - {n_0}^2p_0) \quad (2.11)$$

Where C_n and C_p are the Auger capture probability coefficient for eeh and ehh process, respectively. Due to the strong dependence on the carrier density for the net Auger recombination rate, the Auger lifetime decreases with the increase of the doping concentration. Thus, doping in silicon drastically impacts the rate of Auger recombination. The coefficient C_n and C_p were originally considered as fixed value and calculated only for the high injection and doping conditions [42]. However, it has been reported that the experimental Auger lifetime is lower than the theoretical calculation [43]. Hangleiter and Hacker reported that the discrepancy between the experimental and theory was caused by considering the coefficients C_n and C_p as the constant value [44]. The Coulombic interactions between the charge carriers at low injection level was subsequently introduced in the Auger model [44], and enhancement factors g_{eeh} and g_{ehh} were added to account for the probability of these three carriers at a given location for the low-level injection (LLI) condition. Therefore, the net recombination rate was recalculated as:

$$U_{Aug,LLI} = g_{ehh}C_p(np^2 - n_0{p_0}^2) + g_{eeh}C_n(n^2p - {n_0}^2p_0) \quad (2.12)$$

Richter et al[45] proposed a combined Auger and Radiative lifetime model depending on the dopant and injection level, which includes Altermatt's parametrisation [46] of the enhancement factors for LLI. The Auger lifetime is recalculated as:

$$\tau_{Aug} = \frac{\Delta p}{\left(np - {n_{i,eff}}^2\right)(2.5 \times 10^{-31}g_{eeh}n_0 + 8.5 \times 10^{-32}g_{ehh}n_0 + 3 \times 10^{-29}\Delta p^{0.92})} \quad (2.13)$$

Where

$$g_{eeh} = 1 + 13\left\{1 - tanh\left[\left(\frac{n_0}{N_{0,eeh}}\right)^{0.66}\right]\right\} \quad (2.14)$$

$$g_{ehh} = 1 + 7.5\left\{1 - tanh\left[\left(\frac{p_0}{N_{0,eeh}}\right)^{0.63}\right]\right\} \quad (2.15)$$

$$N_{0,eeh} = 3.3 \times 10^{17} cm^{-3} \ \ and \ \ N_{0,ehh} = 7 \times 10^{17} cm^{-3} \tag{2.16}$$

Tim Niewelt [47] improved this model based on Coulomb-enhanced Auger recombination for all doping and injecting conditions and the Auger lifetime is calculated as:

$$\tau_{Aug} = \frac{\Delta p}{g_{eeh} C_{eeh} (n^2 p - {n_0}^2 p_0) + g_{ehh} C_{ehh} (np^2 - n_0 {p_0}^2)} \tag{2.17}$$

Where C_{eeh} is $3.41 \times 10^{-31} cm^{-6} s^{-1}$ and C_{ehh} is $1.17 \times 10^{-31} cm^{-6} s^{-1}$ [48].

2.2.4 Defect-Assisted Recombination

Defect-assisted recombination, also called Shockley-Read-Hall Recombination, is when a trap state captures the mobile carriers in the band gap. These trap states are caused by the impurities, dislocations, and vacancies during the material processing. The recombination rate of this process was first modelled by Shockley and Read [40] and developed by Hall [49]. Based on the model, the net SRH recombination rate is associated with the defect density (N_t), the capture cross section for electrons and holes ($\sigma_{n,p}$), and the energy level of a specific recombination centre (E_t). The capture cross section is defined as the area surrounding the defect, where the carriers have a high probability of being captured. The net SRH recombination rate is:

$$U_{SRH} = \frac{np - {n_i}^2}{\frac{p + p_1}{N_t \sigma_n v_{th}} + \frac{n + n_1}{N_t \sigma_p v_{th}}} \tag{2.18}$$

Where v_{th} is the thermal velocity of carriers and p_1 and n_1 are the SRH trap occupancy factors, respectively.

$$p_1 = p_0 e^{\frac{E_T - E_F}{k_B T}} \tag{2.19}$$

$$n_1 = n_0 e^{\frac{E_T - E_F}{k_B T}} \tag{2.20}$$

The SRH lifetime is:

$$\tau_{SRH} = \frac{\tau_{p0}(n_0 + n_1 + \Delta p) + \tau_{n0}(p_0 + p_1 + \Delta p)}{p_0 + n_0 + \Delta p} \tag{2.21}$$

Where τ_{n0} and τ_{p0} are lifetime parameters for holes and electrons, respectively:

$$\tau_{n0} = \frac{1}{N_t \sigma_n v_{th}} \tag{2.22}$$

$$\tau_{p0} = \frac{1}{N_t \sigma_p v_{th}} \tag{2.23}$$

The presented model for SRH recombination assumes the defects only produce a single energy level trap in the band gap. However, defects such as grain boundary could produce a range of traps at different energy levels throughout the band gap [50-52].

2.2.5 Surface Recombination

The semiconductor surface is the termination surface of the lattice. A large number of defects are introduced as the recombination centres for mobile carriers. These defects could be impurities deposited from the external environment, unsaturated bonds (dangling bonds) and manufacturing process induced defects [22, 53, 54]. Therefore, the semiconductor surface is highly sensitive to external factors, which is the fundamental reason why the performance of semiconductor devices is greatly affected by the surface. Dangling bonds at the surface create states with varying energy levels throughout the band gap. The predominant recombination mechanism at the surface is still defect-associated, so the net surface recombination rate also follows SRH theory:

$$U_S = \frac{n_s p_s - {n_i}^2}{\frac{p_s + p_1}{N_{st} \sigma_n v_{th}} + \frac{n_s + n_1}{N_{st} \sigma_p v_{th}}} \tag{2.24}$$

Where n_s and p_s are the electron and hole concentrations at the surface. The state for the recombination is concentrated in two-dimensional space, so N_{st} is the density of the states per unit area (cm^{-2}), instead of unit volume (cm^{-3}) in bulk. In the real surface, there is a continuous distribution of these energy states in the band gap. Therefore, the density of the energy state is referred as D_{it} as a function of energy, and the net surface recombination rate across the band gap (E_V to E_C) is defined as:

$$U_s = (n_s p_s - {n_i}^2) v_{th} \left(\int_{E_V}^{E_C} \frac{D_{it}(E)}{\frac{p_s + p_1}{\sigma_n(E)} + \frac{n_s + n_1}{\sigma_p(E)}} dE \right) \tag{2.25}$$

The surface recombination velocity (SRV) is a parameter to describe the recombination rate of the carriers at the surface, which is defined as:

$$SRV = \frac{U_S}{\Delta n_d} \tag{2.26}$$

Where Δn_d is the excess carrier concentration near the surface.

The bulk and surface recombination are all defect-associated recombination, the difference between them is defined by the depth region where the surface recombination becomes the bulk recombination. The calculated SRV above assumes that the conduction band and valence band all are flat through the whole semiconductor with uniform defect density and dopant. However, in the actual semiconductor, a space charge region will exist and cause band bending due to the accumulation of charge at the surface [22]. The recombination occurring in the band bent region is defined as the surface recombination while the recombination in the flat region is defined as the bulk recombination.

2.3 Surface passivation in silicon solar cells

To reduce the impact of defect-assisted recombination, gettering [55] and passivation methods [22, 56] are employed. The gettering method is achieved through the diffusion of impurities to regions where the performance of the cell is less detrimental. This technique is important in the solar cells' development, but not related to the work presented in this thesis. The passivation method can be divided into two categories: Field effect passivation (FEP) and chemical passivation. For the chemical passivation method, the mitigation of the recombination is achieved by using the chemical species to satisfy unsaturated bond and eliminate defect states. Field effect passivation is achieved by creating an electric field near the surface, where the charge carriers of similar polarity would be prevented from approaching. These two passivation methods are normally employed in conjunction in actual cell manufacturing [56-58].

2.3.1 Chemical Passivation

Two main methods are employed for the chemical passivation of silicon solar cells. One method is depositing a capping dielectric layer. The other one is using hydrogen to passivate the unsatisfied states. The main dielectric layers used in silicon solar cells are SiO_2, SiN_X and AlO_X. At first, these layers work as the anti-reflection layer . The reflectance of the polished Si wafer can be over 30% [59], while the reflectance of the wafer with an anti-reflective coating layer can be well below 0.5% through the reduction of the light reflection at the interface [60]. In the actual solar cell production line, the anti-reflective coating process is always combined with the surface texturing process, which creates the pyramids on the surface to increase the possibility for the reflected light bouncing back to the surface [61]. Besides that, the deposited dielectric layer

can combine with the dangling bonds at the surface, which reduces the density of the defects states. The SiO_2 is used in silicon cell architectures due to its low D_{it} at the silicon surface providing good passivation quality [22]. However, it does not have good antireflection ability on its own. It is normally capped with a SiN_X layer that provides fixed positive charges and free hydrogen atoms during PECVD deposition [22, 62]. The mobile hydrogen atoms can diffuse to the interface and saturate silicon dangling bonds at the interface, reducing the interface state density. Hydrogen plays an important role in the chemical passivation in silicon solar cells and will be discussed in Section 2.6.1.

2.3.2 Field effect Passivation

In the previous section, it has been noted that there is an intrinsic concentration of the fixed charges incorporated during the synthesis of dielectric layers [62-64]. The positive charges in the SiN_X layer form a built-in electric field on the surface of the silicon wafer, which reduces the concentration of one carrier type and thus the probability of carriers recombination on the surface. However, since the existence of the positive charge, it only has a good passivation effect on the n-type silicon surface. When applied to the highly doped p+ surface, it does not show effective passivation. For p-type Si, an AlO_X layer containing a high concentration of negative charge states and hydrogen atoms is used [62, 64, 65]. The combination of the SiN_X/SiO_X and AlO_X/SiO_X layers used opposite cell sides can lead to effective passivation. However, the intrinsic charges in the dielectric layers are not optimal to fully exploit FEP [56, 66]. Extrinsic charges could be applied to control the carrier concentration at the surface and enhance passivation. There are two main techniques to apply FEP: Diffusion of a doping profile in the near-surface region and adding additional charges via the extrinsic process. The diffusion of the doping profile will create an internal electric field to control the migration of the charge carriers [57]. This method is not used in this thesis and would not be explained in further detail. Adding the extrinsic charges to the capping dielectric layer, through corona discharge for example, is used in various literature works [67-69], and exploited here. For this technique, the charges are generated by the application of the high voltage in the order of kV to a pin-like electrode. This electrode ionizes the molecules around it and generates a corona-shaped plasma. The ionized atoms scatter and drift to the sample placed on the ground plate, which generates the surface electric field. The positive voltage applied on the pin-like electrode attracts the electron to the source and the positive ions will drift to the sample. The negative voltage attracts the positive ions and the free electrons collided with the ambient air molecules will drift to the samples. It has been shown

that the positive charges are the hydrated hydrogen atoms ($(H_2O)_nH^+$) and the negative charges are CO_3^- ions [70]. Corona discharge is used throughout this thesis to generate the surface electric field to investigate the hydrogen kinetics in different cell architectures.

2.4 Overview of Silicon Solar Cell Architectures

The first practical single crystalline silicon solar cell with 6% efficiency was made in Bell Labs in 1954 [71]. To reduce climate change and meet renewable energy needs, a variety of high-efficiency silicon solar cells have been developed today, including passivated emitter and rear contact (PERC) solar cells, tunnel oxide passivated contact (TOPCon) solar cells and silicon heterojunction (SHJ) solar cells. Figure 5 show the schematic of these cells' structures. According to the ITRPV 2023 report [21], among all these architectures, PERC still dominates the market share of around 70%, while TOPCon and SHJ have a market share of around 15% and 7%, respectively. According to the forecast, the dominance of PERC will end around 2025. The TOPCon cell would take the market share of 60% in 2033, while the SHJ cell would take the 19% market then. In the following section, the evolutionary development of these high-efficiency cells is discussed.

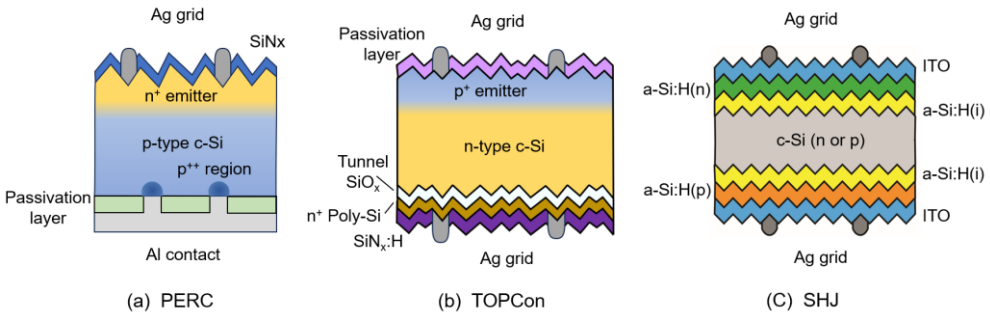

Figure 5. Schematic of commercial silicon solar cell structure (a) Standard PERC (b) Standard TOPCon solar cell (c)Standard SHJ solar cell.

2.4.1 Passivated Emitter and Rear Contact solar cell

The PERC solar cell is developed from the aluminium back surface field (Al-BSF) cell depicted in Figure 6.a. p-type silicon is used as the main substrate and phosphorus diffused emitter forms the p-n junction, while the front surface is textured and then passivated with hydrogenated Silicon Nitride (SiN_X) layer. For the rear side, Al paste is screen-printed with base silicon to create the back surface field and fully back Al contact. Even with the improvement of the doping concentration and firing process, the efficiency of the Al-BSF cell

can achieve 20.29% [72], which is still far from the Shockley-Queisser limit efficiency of 29.4% for an ideal single-junction crystalline silicon solar cell [47, 73]. The efficiency of Al-BSF is limited by the high rear side recombination and just 65% of the long-wavelength light can penetrate and reach the rear side due to the internal reflection [74], as shown in Figure 6.a. The fundamental difference with the PERC architecture is the addition of a dielectric layer, such as SiN_X/AlO_X stack, with local contacts on the rear side [75]. This is displayed schematically in Figure 6.b. There are two benefits of this rear passivation layer, i) surface recombination is supressed compared with Al-BSF and ii) improved reflection increases the amount of long wavelength light than can be absorbed in the silicon. The localised p++ region reduces the resistance loss between the silicon and metal contact, as shown in Figure 6.b. Due to the high compatibility with previous Al-BSF industry production lines and high efficiency with a 24.5 % record [76], the PERC cell dominates the market up until 2023. However, the back surface of the PERC cell still has around 5-10% of the area in contact with metal [77], which will still cause minority carrier recombination. Therefore, the passivating contact architecture is introduced as a next-step evolution to reduce the metal silicon contact losses.

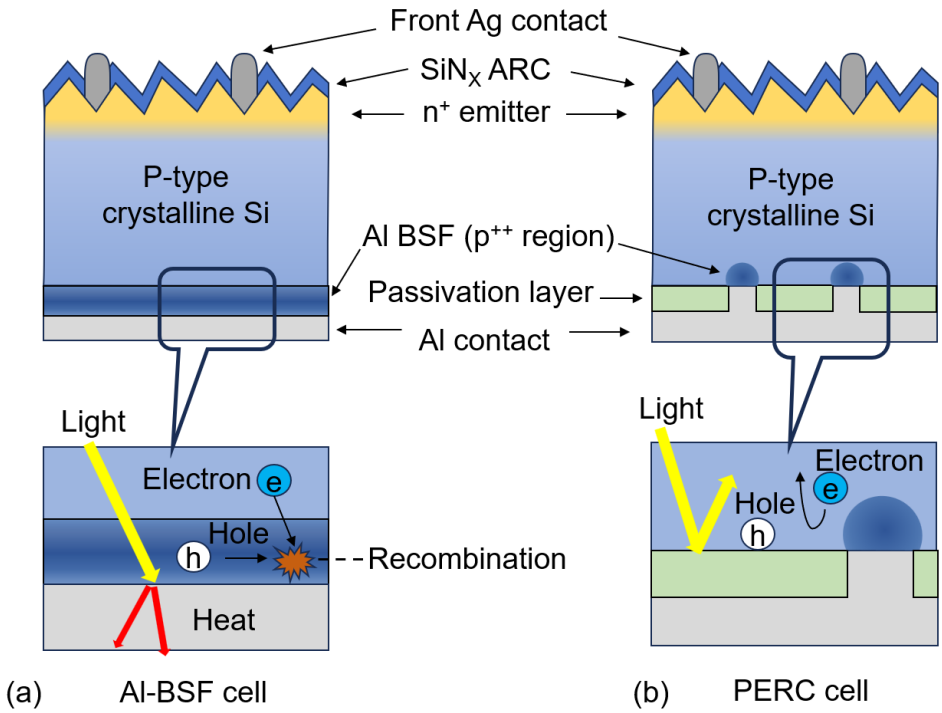

Figure 6. Schematic of (a) Al-BSF cell and its rear side structure, (b) PERC cell and its rear side structure.

2.4.2 Tunnel oxide passivated contact solar cell

Silicon solar cells with passivated contacts are a promising approach for higher efficiency. Amongst the viable approaches, tunnel oxide passivated contact (TOPCon) solar cells have recently gained substantial interest as future market-dominant cell architecture [78, 79], due to the excellent rear surface passivation. The key to this technology is the passivated contact provided by the combination of an ultra-thin oxide of ~ 2 nm [80] and heavily doped polysilicon layer [79, 81, 82]. The excellent passivation on the rear side provides effective chemical and field effect reductions to charge loss. N-type silicon is used as the main substrate and the front surface is achieved through the combination of the p+ emitter and a passivating stack formed by an AlO_X/SiN_X double layer, depicted in Figure 5.b. For the rear side, the thin oxide / doped polysilicon passivation scheme is capped with a hydrogen-containing dielectric, such as SiN_X:H or AlO_X:H layer. For TOPCon cells, the thin layer of SiO_2 film on the back surface completely isolates the interaction between silicon and metal. Due to this design, a very low surface recombination current density (J_0) and low contact resistivities are achieved, which facilitates high V_{OC} and fill factor (FF) [81]. TOPCon has achieved a record efficiency of 26.89% with a mass production efficiency of 26.01% in Jinko Solar, which is close to the theoretical efficiency limit for TOPCon at 28.7% [83]. Additionally, the mass production for this design shows great compatibility with PERC, which could allow for easy implementation with a few additional tools. Silicon cells adopting this contacting scheme may also be referred to as polysilicon on oxide (POLO), as the current transport can occur via both tunnelling and pin-hole mechanisms depending on the thickness of the interfacial oxide layer[84, 85].

2.4.3 Silicon heterojunction solar cell

The last cell architecture to be discussed is the silicon heterojunction solar cell. SHJ solar cells have recently achieved a world record efficiency of 26.81% [86] and are thus gaining significant interest as a possible approach to replace the incumbent PERC cells in mass production. The high performance of this architecture is achieved by the structure of crystalline silicon wafers passivated by stacks of intrinsic and doped amorphous silicon (a-Si) [87-89]. Figure 5.c depicts the structure of this cell architecture. The intrinsic amorphous silicon film and the p-type doped amorphous silicon film are deposited on the rear side in sequence. On the front side, the intrinsic amorphous silicon film and the n-type doped amorphous silicon film are deposited. The difference in the doping provides carrier selectivity. Due to the poor conductivity of the amorphous silicon films, a transparent conductive oxide (TCO) film is deposited on both sides of the cell to

allow for lateral conduction to the contacts. An Ag grid screen printed is used to form double-sided electrodes. Bilayers of intrinsic and doped amorphous silicon (a-Si:H) work as the exceptional passivation and charge-selection layers, due to their large bandgap (~1.7 eV, compared with 1.12 eV for c-Si) and their good compatibility for doping [90]. This design can lead to low surface recombination current density (J_0) which facilitates high V_{OC}, and low processing temperature [91]. Since n-type monocrystalline silicon is usually used as the substrate for SHJ cells, the cell is not limited by the LID effect caused by the boron doping. Since the surface is deposited with the TCO film without an insulating layer, there is no chance of the surface layer being charged, structurally avoiding the occurrence of PID [92]. Even with the challenge of the high cost of tools for cell production and the great consumption of silver, it shows great potential as the future market dominant to pave the way to >25% silicon solar panels.

2.5 Light-induced instabilities in commercial solar cells

The stability under prolonged light illumination is an important criterion for solar cell devices. Studying the mechanism behind these changes is essential to maintain cell efficiency and thus boost the development of solar energy. The different architectures have different response for the light-induced changes. PERC and TOPCon cells suffer from degradation with illumination, while the light-induced enhancement is observed in SHJ cells.

2.5.1 Light and elevated temperature induced degradation

Light induced degradation (LID) is one of the main types of degradation in field operation, which is caused by the increase of the excess minority carrier recombination under injection carrier such as illumination or biasing current [93-95]. Various studies have been carried out on understanding of the mechanism of the LID [96-98] , while the formation of the boron-oxygen defects in silicon cells has been considered as the prominent cause for the LID [99, 100]. It showed that LID caused by Boron-Oxygen defect (BO-LID) can be regenerated by annealing at elevated temperatures with carrier injection [101-103]. This regeneration process can be achieved in seconds with high injection carrier.

However, Ramspeck et al. reported an unusual LID in mc-Si PERC solar cells in 2012 [104]. Normal LID caused by Boron-Oxygen defect can achieve the saturation of the degradation at room temperature in the time scale of a few days or months. However, this unusual LID achieves the saturation of the degradation at

elevated temperature (above 75 °) with time scale of months to years. The time scale for this LID cannot be explained by the BO-Oxygen defect and then this LID is referred as Light and elevated temperature induced degradation (LeTID). LeTID is observed in a wide range of silicon solar cell architectures [28], including boron-doped Cz-Si [105, 106], boron-doped float-zone silicon [107, 108] and n-type Cz-Si [109-111]. This degradation can cause significant reductions in V_{OC} [28, 112, 113], which is detrimental for modules installation in the field [113, 114]. Gallium doping p-type silicon solar cell show a more stable performance compared with boron-doped solar cell, due to the absence of BO-related degradation [115-117]. However, LeTID is still observed in Ga-doped p-type silicon solar cells [116, 118, 119], which put more evidence that LeTID is not caused by the Boron-Oxygen defect. The actual mechanism behind the LeTID is still not clear, but there have been several reports showing the hydrogen involvement in the formation of LeTID, including varying the firing conditions [120], SiN_X stoichiometry [103] and thickness [121]. It has been reported that the impact of LeTID can be mitigated through thermal treatment in the range of 300 °C – 500 °C, which recovers the V_{OC} of the cells effectively [122]. However, this thermal treatment also causes an increase of the series resistance (R_S), which leads to the deterioration of the FF [30, 123, 124].

Chan et al. have reported that the application of the forward current on mc-Si PERC can cause a decrease of R_S, while the removal of the forward current can cause an increase of R_S [124]. This unstable change of R_S with the varying applied bias conditions cannot be fully explained by a thickening of the glass layer at the Ag / Si interface, which is hypothesised by Peral et al [123]. Hamer et al. showed that the application of a current during the thermal process can lead to the increase of R_S by an order of magnitude and it can be mitigated again with the injected current in the opposite direction, which showed that the direction of the applied field has a profound impact on the series change of the cell [30]. These observations indicated that the change in R_S with varying applied conditions should be related to the mobile charged particles inside the cells, while hydrogen is the most likely candidate due to its high mobility at room temperature [125]. Therefore, there should be some link between the hydrogen involvement and the formation of LeTID inside the silicon solar cells.

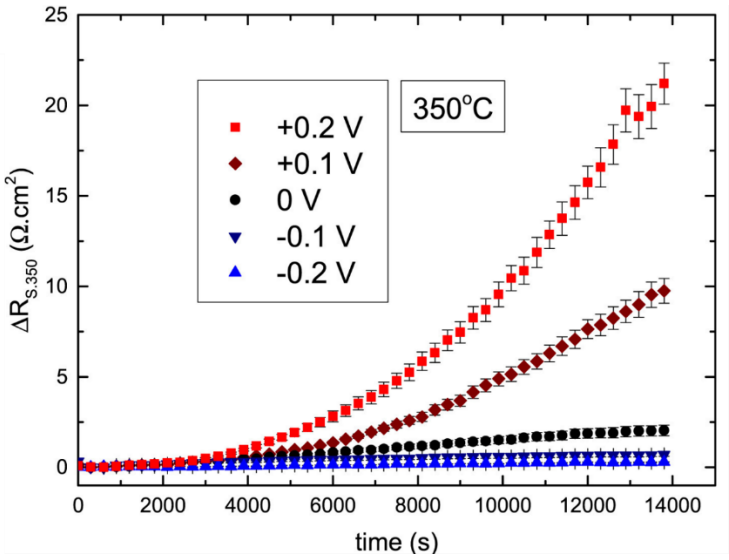

Figure 7. In-situ series resistance change of p-type PERC samples with applied bias between -0.2 and 0.2 V in the dark at 350 °C. Reproduced after [30].

2.5.2 Firing induced degradation

There have been several reports about firing-induced instabilities in thin oxide/ n+ doped poly-Si layers both in n-type and p-type wafers [32, 126-129]. This degradation is attributed to the deterioration of surface passivation after an industrial-type firing step, correlated with an increase of J_0 [127, 130]. Di et al. investigated such lifetime instabilities following light soaking for samples capped with SiN_X deposited through plasma-enhanced chemical vapour deposition (PECVD) and low-pressure chemical vapour deposition (LPCVD) methods [33]. They demonstrated that the firing of a hydrogen-containing dielectric is required to induce such lifetime instability. By subsequently removing the passivation stacks and replacing them with superacid passivation, they concluded that the firing-induced instability is related to a deterioration of surface passivation, rather than in bulk, and that this degradation is related to hydrogen. To investigate the cause of this surface-related degradation (SRD), Di et al. investigated the concentration of hydrogen near the interface using secondary ion mass spectrometry (SIMS) [34], depicted in Figure 8. They concluded that the increase in J_0 correlates with an increase in hydrogen concentration near the c-Si / SiO_X interface, implying the formation of hydrogen-induced defects.

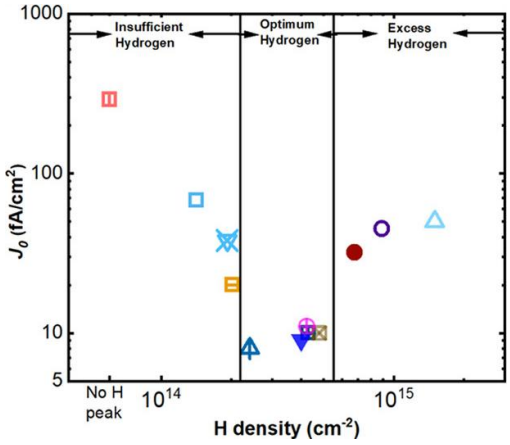

Figure 8. J_0 values measured after firing as a function of hydrogen density estimated by integrating the hydrogen signal between sputter depths of 50 and 150 nm, reflecting the hydrogen density around the SiO_X interlayer. Reproduced after [34].

Therefore, developing a method to control the hydrogen diffusion inside TOPCon is essential to mitigate SRD. It has been reported that the post-metallisation annealing in the range of 300 °C – 400 °C can help to mitigate this SRD in samples with thin oxide / doped polysilicon layers [131]. This mitigation treatment condition is similar to the mitigation method for LeTID in PERC. For PERC cells, the instability of the contact resistance change during degradation can be controlled by the application of an electric field, which is related to the diffusion of hydrogen [30, 125, 132]. For TOPCon cells, it has also been reported that similar instability in contact resistance is observed and that electric fields can modulate the degradation [133]. Besides that, the presence of a surface electric field can impact the surface passivation after the firing of hydrogen-containing dielectrics [134]. Based on these works, Hydrogen is believed to be responsible for SRD in TOPCon cells, and hence the application of electric field shows great potential as an approach to modify the diffusion of H and study the mechanisms behind it.

2.5.3 Light-induced enhancement in SHJ cells

There have been several reports about light-soaking enhancement in SHJ cells [35, 37, 135]. Mahtani et al. reported the improvement of the lifetime for SHJ samples in the presence of doped layers with light illumination with 1-sun intensity. This enhancement did not happen on the samples with only an intrinsic amorphous layer on both sides [35], depicted in Figure 9. Kobayashi et al. reported an improvement of efficiency for SHJ cells around $0.3\%_{abs}$ after 15 hours 1-sun light soaking treatment, which was caused by increased V_{OC} and FF [135]. Wright et al. reported that application of 100-sun illumination at 200 °C can

increase the efficiency of SHJ cells up to 0.7%abs after 30 seconds treatment, which shows great potential to be tailored to time scales compatible with mass production [37]. However, the mechanism behind light soaking enhancement in SHJ cells remains unclear. The current hypothesis is that hydrogen migrates to the a-Si:H/c-Si interface to improve surface passivation due to the electric field induced by the doped layers [136]. The involvement of the hydrogen seems to play an important role in these architectures but little understanding is yet available.

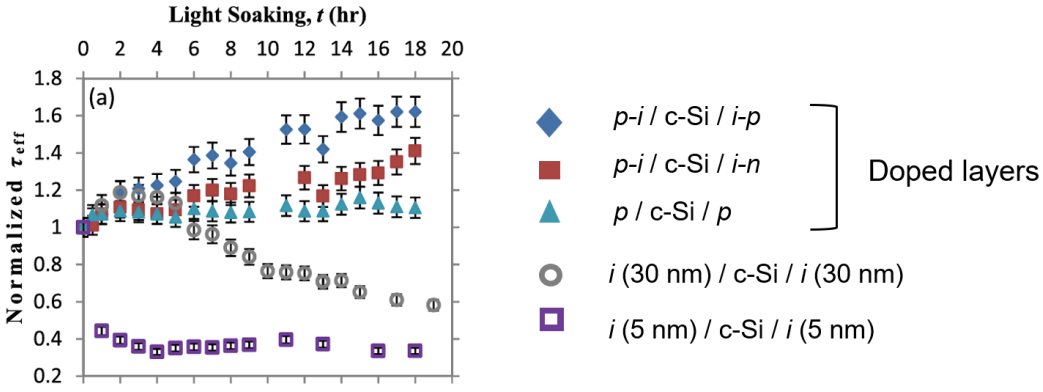

Figure 9. Light induced normalized effective lifetime change as a fuction of light soaking time to the a-Si:H/c-Si heterointerface using intrinsic layers, doped layers, and doped—intrinsic bilayers of a-Si:H specimens. Reproduced after [35].

2.6 Hydrogen in high efficiency silicon solar cells

2.6.1 An overview of hydrogen passivation

Passivation of the silicon surface and bulk defects is critical to achieve high efficiencies, since the quality of it determines the cells' minority carrier lifetime. The introduction of H into Si is exploited in the mass production of commercial silicon solar cells, due to its good performance-enhancing ability. Hydrogen passivation is achieved through the introduction of atomic H from a hydrogen-containing layer. For PERC and TOPCon cells, SiN_X:H and AlO_X:H dielectric layers deposited by PECVD are the main hydrogen sources during the metal contact firing step [23, 24, 137, 138]. For SHJ cells, hydrogenated amorphous silicon (a-Si:H) layers work as the hydrogen source and atomic hydrogen atoms are released through the breaking of the Si-H bond during thermal annealing [139, 140]. Due to its high mobility and reactivity, hydrogen shows a range of complex reactions with defects, dangling bonds, contaminants, and dopants when it is introduced into semiconductors [141-144]. The boron-oxygen complexes, which lead to the LID, can be deactivated

effectively by hydrogen passivation and this deactivation process is reversible at the low temperature (70°C) [145-147]. The low-temperature mobility of H in Si is relevant for the degradation and enhancement phenomena in these architectures.

2.6.2 The charge states of hydrogen

The hydrogen passivation technique is well-developed and leads to a significant increase in the cell's effective lifetime [58, 148]. To better understand and control this passivation method, it is important to understand the transport of hydrogen inside the cells. The charge state of the interstitial hydrogen is an important parameter [149]. Hydrogen can passivate the boron atoms in the p-type silicon wafer and phosphorus atoms in the n-type silicon wafer with different charge states [146, 150]. Hydrogen migrates in a silicon wafer mainly in the interstitial form and monomers exist in three charge states: positive (H^+), neutral (H^0) and negative (H^-). The charge state is controlled by the local concentration and distribution of electrons and holes [125, 151]. Several groups reported that the charging state of monoatomic hydrogen is dependent on the fermi level under various conditions [152-154]. Hamer et al. simulated the model of the distribution of intrinsic hydrogen atoms with different charge states between 300°C and 700°C [132], showing that the transport of hydrogen under non-equilibrium strongly depends on electric fields and temperature. The hydrogen state will be switched into different states when it goes over a cross-over point in the silicon bulk as shown in Figure 10. The application of the electric field can control the migration of the hydrogen with different charge states. When a forward bias is applied, H^+ will be pushed into the p-type bulk part and H^- will diffuse into the surface part. Due to the existence of the built-in voltage in the junction, only H^0 is free from the electrostatic effects and diffuses through the depletion region before it can switch into H^+ by thermal ionization reaction [155, 156].

$$H^0 \rightarrow H^+ + e^- \qquad (2.27)$$

The switch between H- and H+ states is achieved by the driving force to establish a local equilibrium concentration in the substrate. Generally, H^+/H^0 species exist and diffuse in p-type silicon and H^-/H^0 species exist and diffuse in n-type silicon. The majority of impurities inside the silicon solar cells are dopant elements, boron and phosphorus atoms. For the p-type silicon, hydrogen with a positive charge state can interact with the boron atoms [132].

$$H^+ + B^- \rightleftarrows HB \qquad (2.28)$$

The interaction is dependent on the temperature and dopant concentration. This pair might dissociate rapidly during annealing above 200°C with boron concentration up to $10^{16}cm^{-3}$. Besides H-B, there are other hydrogen complexes in p-type silicon such as H-Fe and H-Cr, which will dissociate into monoatomic hydrogen below 500°C when the dopant concentration is less than $10^{17}cm^{-3}$ [157]. For n-type silicon, hydrogen will interact with the phosphorus dopant atoms [132].

$$H^- + P^+ \rightleftarrows HP \tag{2.29}$$

Because electrons attract positively charged hydrogen ions and holes attract negatively charged hydrogen ions, the interaction of dopant elements with charged hydrogen ions is minority carrier concentration dependent [132]. The neutralization and reactivation of dopant elements depends on the temperature and dopant concentration. Therefore, controlling the concentration of hydrogen with different charge states is essential to achieve high-efficiency solar cells. The previous models and theory all are based on one assumption that the mobile hydrogen atoms all are in the interstitial form. In the actual cells, the existing state of hydrogen atoms is controlled by the temperature and only a small portion of interstitially formed hydrogen atoms exist below 600 °C [158]. When the temperature is below 600 °C, hydrogen exists in the form of hydrogen complexes inside the silicon wafer such those mentioned before, as well as hydrogen dimers (H_2). The efficacy of hydrogen passivation is strongly dependent on the hydrogen charge states at different layers.

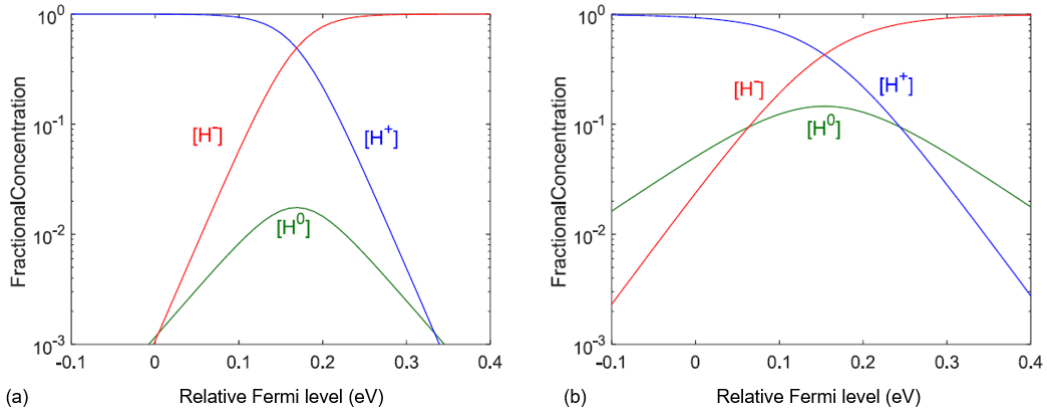

Figure 10. Fractional concentration of hydrogen with different charge states as a function of Fermi level (relatively to the middle of the band gap) (a) at 300°C (b) at 700°C. Reproduced after [132]

2.6.3 Hydrogen-related defects in silicon

The hydrogen passivation method is perceived as a standard performance-enhancing process for commercial Si solar cells. However, it has been reported that H can sometimes cause a negative impact when

introduced into Si. There are multiple reports that H plays an important role in the activation of LeTID in p-type mc-Si and cast Mono-Si [29, 159, 160]. The degradation of p-type mc-Si was first seen through a noticeable efficiency loss of around 7% in fabricated cells. Although the actual mechanism behind the LeTID is still not clear, H was identified as a possible cause for LeTID. Interstitial hydrogen would be introduced into the silicon wafer at various concentrations from the hydrogenated dielectric layer during the fast-firing process[161, 162]. It is observed that this degradation process can be activated once the peak temperature exceeds 700°C [163]. The extent of the LeTID can increase with the firing temperature and an absence of the degradation is observed for unfired samples [163, 164]. The LeTID for the fired samples can be mitigated through the thermal treatment in the range of 300 °C – 500 °C. However, this post-firing treatment would cause an undesired increase in contact resistance and the front Ag-Si interface is most affected [124]. Bredemeier et al reported that the recovery can be caused by the diffusion of species to or from the surface[100]. Considering the required diffusivity for this phenomenon, they suggested that these species should be metal impurities or H. The contact resistance change caused by the metal impurities during firing has been explained as a thickening of the glass layer at the Ag / Si interface by Peral et al. [123]. In their test, a glass layer is formed between the Ag and Si substrate from the added glass frit to the paste during the firing process. The composition of glass layer is dependent on the composition of the silver paste, the Si surface morphology and firing conditions, which can contain lead monoxide (PbO), silicon dioxide (SiO_2), boron oxide (B_2O_3), and zinc oxide (ZnO). Figure 11 shows the front contact change with different fired conditions. When the sample is underfired shown in Figure 11.a, small Ag precipitates are distributed inside the glass layer. The electron needs the extra energy to jump to adjacent Ag precipitates and be collected at the Ag bulk, which leads to high resistance. When the sample is optimally fired shown in Figure 11.b, the Ag bulk has good contact with the emitter substrate, so the electron can be directly transferred to the Ag bulk after crossing the Schottky barrier. If the thickness of the glass between them is small enough, some electrons might tunnel across the silver and be collected by Ag bulk. When the sample is overfired shown in Figure 11.c, large Ag colloids are formed and distributed inside the glass layer, with current flow being limited to Thermionic-field emission [165]. Although firing could change the resistance by redistribution of Ag colloids and glass colloids, the resistance change from that cannot be affected by the applied electric field. The correlation between the change of the series change and applied bias shows that the LeTID is consistent with Hydrogen dynamics [30]. The LeTID should be caused the hydrogen-related defects.

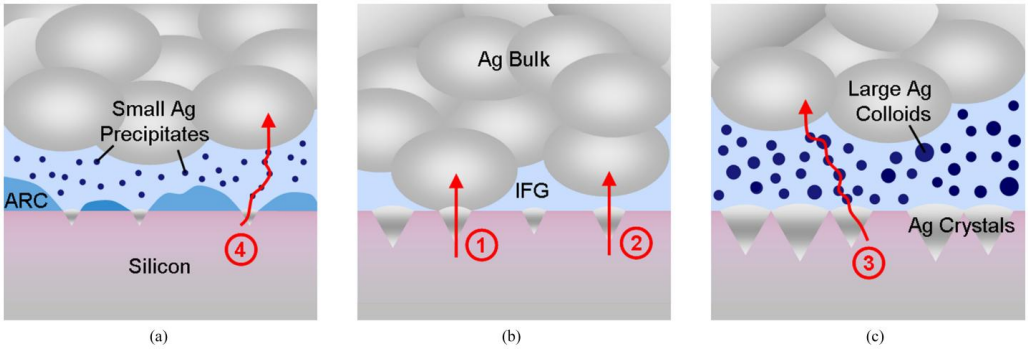

Figure 11. Front contact structure with different fired conditions. (a) Underfired (b) Optimally fired (c) Overfired. Reproduced after [123].

H-related defects were observed in different architectures discussed in the previous literature. The firing-induced degradation at the n+ poly / SiO_X / c-Si interface have been reported which significantly reduces the surface passivation of the TOPCon cells [32, 166]. It is hypothesised that hydrogen plays a role in this surface-related degradation [34]. However, the role of hydrogen in this severe surface degradation remains unclear. Most of the published work show the link between the H and these degradations. It is not yet widely known how the H is responsible for these degradations. As such, it is important to find method to study the kinetics of hydrogen in these architectures.

2.7 Summary of the presented literature

Studying the mechanism of the degradation and finding methods to mitigate it are essential to achieve high-efficiency solar cells. The three dominant silicon cell architectures, PERC, TOPCon and SHJ, suffer from different degradation and enhancement effects, and H plays an important role in all of these phenomena. In this chapter, the influence of hydrogen is explored all three architectures.

Although light and elevated temperature induced degradation (LeTID) in p-type multicrystalline-Si passivated emitter and rear cell (PERC) has been reported widely, the actual mechanism behind that is still not clear. One approach to mitigate LeTID is a thermal treatment in the range of 300 °C–500 °C, but this will cause severe deterioration of the FF, dominated by an increase in series resistance (RS). The existing understanding is that this undesired resistance change is at front contact and linked to hydrogen. However, the origin of this change and how it is linked to hydrogen are missing from the growing body of literature. Due to the great mobility and different charge states, using an electric field to control the migration of hydrogen to study the contact resistance change is a good method to understand the kinetics of hydrogen in LeTID, which

is good for the development of processing strategies that mitigate degradation and enhance stability in PERC cells.

For TOPCon cells, surface-related degradation (SRD) is triggered in fired samples by the presence of elevated temperature and illumination. In literature, several reports have indicated that the degradation may be caused by an accumulation of hydrogen near the interface. However, there is limited direct evidence unambiguously proving that excess hydrogen is the cause of the SRD. Using surface polarisation to control the migration of hydrogen shows good potential to study the nature of SRD in TOPCon cells.

For Silicon heterojunction (SHJ) solar cells, light soaking has been shown to improve surface passivation, while high temperatures are known to degrade the interface passivation in SHJ cells. Interestingly, the surface passivation only improves in the presence of doped amorphous silicon (a-Si) films. The current hypothesis is that during light soaking, hydrogen ions are released from the a-Si and migrate towards the c-Si / a-Si interface in the presence of the doped layer and passivate dangling bonds. In this area, it is possible to test this hypothesis by investigating light soaking improvements in surface passivation in the presence of surface electric fields induced by corona charging. The stability under prolonged light illumination is an important criterion for solar cell devices. Finding method to study the kinetics of hydrogen in these architectures are important to keep cells with good stability.

Chapter 3 Experimental methods

This chapter discusses the equipment used for the fabrication and characterisation of the different silicon solar cell architectures. A general overview of the processes used for specimen preparation and characterisation is provided. The hydrogen dynamics in PERC, TOPCon and SHJ are investigated in this thesis. Due to the difference in the architecture and degradation phenomena, the processing treatments specific to each architecture will be discussed alongside the results in subsequent Chapters.

3.1 Silicon materials

Three different types of silicon solar cells were used: Passivated Emitter and Rear Contact (PERC) solar cells, Tunnel Oxide Passivated Contact (TOPCon) solar cells and Silicon heterojunction (SHJ) solar cells. All the samples used were received from commercial companies or institutes. The PERC and TOPCon specimens were fired in industrial furnaces at 800 – 850 ℃ [167, 168]. The schematic structures for these three solar cell architectures are shown in Figure 12 to Figure 14, and Table 1 summarises the different substrates used during this project.

PERC: Experiments in this work were carried out on standard commercial full-size p-type mono PERC cells obtained from UNSW and Trina Solar. The 156 mm × 156 mm cells were laser cleaved into 1.5 cm × 1.5 cm for further current-voltage measurement. Figure 12.a shows the schematic of the original PERC cell. A boron-doped p-type Cz-Si is used as the main substrate and a phosphorus-diffused emitter is used to form the p-n junction. The front surface is textured and then passivated with SiN_X layer. A dielectric layer (SiN_X/AlO_X) stack with local contacts is formed on the rear side. Both metal contacts are formed via industrial screen printing and firing. Figure 12. b shows the schematic of a modified PERC cell structure with a front Al contact added, which is designed to measure different components of series resistance in PERC separately.

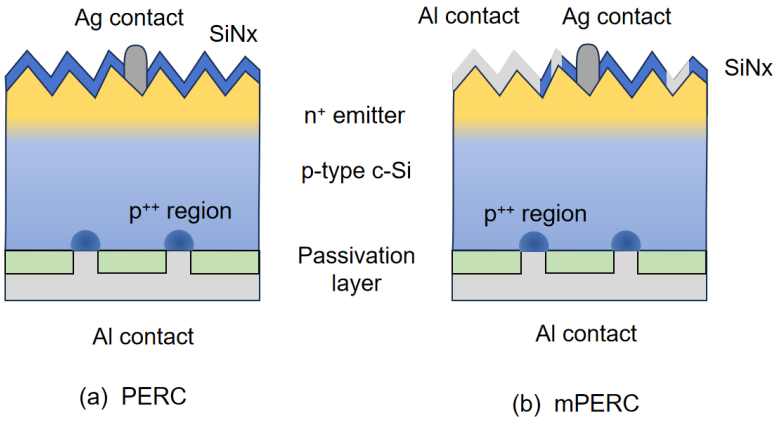

Figure 12. Schematic of PERC cell structure. (a) Original PERC cell (b) Modified PERC cell, where m indicates the PERC specimen after modification with the existence of the front Al contact.

The modified PERC sample geometry and modification process are shown in Figure 13. One silver finger and a small portion of the busbar at the front surface are painted with photoresist and left to dry overnight. The rear back aluminium contact is fully covered in photoresist for protection. The extra silver remaining at the front surface is etched off with nitric acid and DI water solution, with a 2:3 ratio by volume. A photoresist layer is painted on top of the existing photoresist line to isolate the silver finger with a larger area, and a circular line of photoresist is drawn around the photoresist-coated region and left to dry for ~ 30 minutes. Reactive Ion Etching (RIE) is used to etch off the front silicon nitride layer with 25 sccm CHF_3 and 25 sccm Ar for ~10 minutes. 100 nm of aluminium are deposited on the front surface through thermal evaporation. Lastly, the front aluminium and silver contacts are exposed through etching off the remaining photoresist via acetone in an ultrasonic bath at 40 ℃.

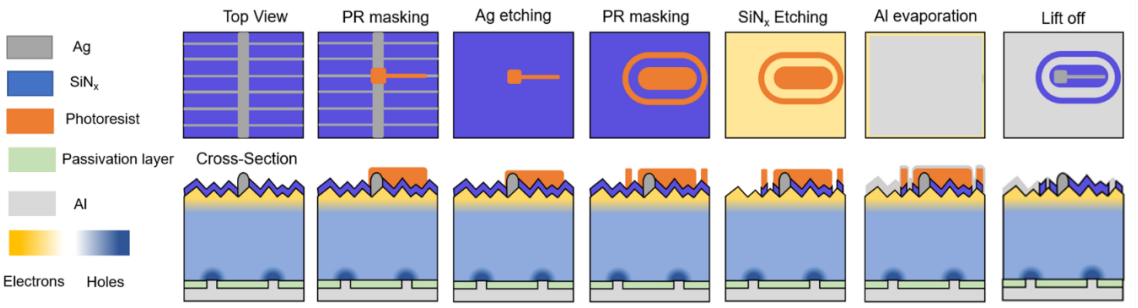

Figure 13. Schematic of the modified geometry process for PERC specimen

TOPCon: Experiments in this work were carried out on six kinds of TOPCon specimens. The first one is the standard commercial n-type TOPCon solar cells as shown in Figure 14.a, which was obtained from Trina and labelled as TOPCon cell. N-type phosphorous-doped Cz-Si is used as the main substrate and the front surface is achieved through the combination of the p+ emitter and a passivating stack formed by an AlO_X/SiN_X

double layer. For the rear side, the thin oxide (1~2 nm) / doped polysilicon passivation scheme is capped with a hydrogen-containing SiN_X:H layer. The metal contacts are formed via industrial screen printing and firing in Trina. The 156 mm × 156 mm cells were laser cleaved into 1.5 cm × 2 cm for further current-voltage measurement.

The second sample structure is the n-type TOPCon cell precursor without metallisation, obtained from Trina and labelled as TOPCon cell precursor as shown in Figure 14.b, which has been fired in Trina. The third type is the nnnTOPCon lifetime specimens with the structure of n-type Cz-Si substrate combined with symmetrical thin SiO_X / n-type poly-Si layers on both sides as shown in Figure 14.c. This type was obtained from Trina and ANU separately and firing in their institutions respectively. The fourth type is the pnpTOPCon lifetime specimens with the n-type Cz-Si substrate combined with symmetrical thin SiO_X / p-type poly-Si layers on both sides as shown in Figure 14.d, which was obtained from Fraunhofer ISE and fired there. The fifth type is the pppTOPCon lifetime specimens with the p-type Cz-Si substrate combined with symmetrical thin SiO_X / p-type poly-Si layers on both sides as shown in Figure 14.e, which was obtained from Fraunhofer ISE and fired there. The sixth type is npnTOPCon lifetime specimens with the structure of p-type Cz-Si substrate combined with symmetrical thin SiO_X / n-type poly-Si layers on both sides as shown in Figure 14.f, which was obtained from ANU and fired there. The received 156 mm × 156 mm wafers were laser cleaved to 4 cm × 4 cm size for further light soaking treatment and lifetime measurement.

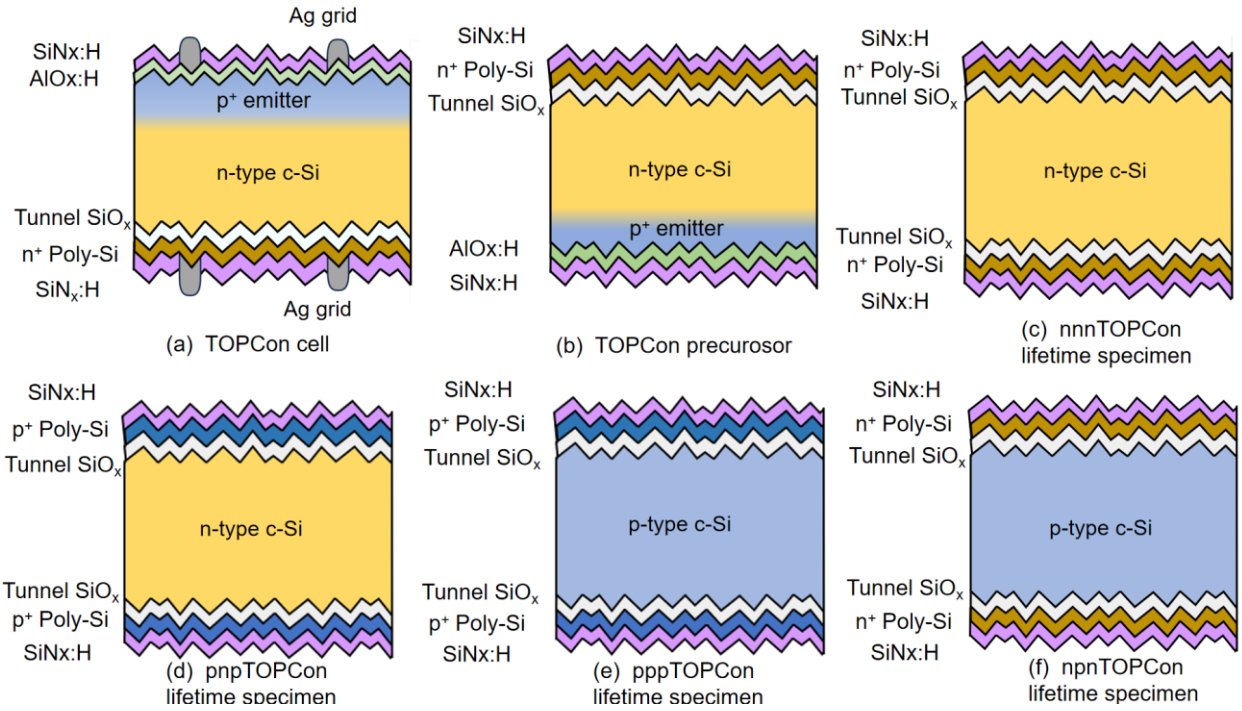

Figure 14. Schematic of the structure of the tested TOPCon specimens. (a) Standard n-type TOPCon cell (b) n-type TOPCon cell precursor without metallisation. (c) nnnTOPCon lifetime specimens, where nnn indicates the n-type Cz-Si substrate combined with symmetrical thin SiO_X / n-type poly-Si layers on both sides. (d) pnpTOPCon lifetime specimens, where pnp indicates the n-type Cz-Si substrate combined with symmetrical thin SiO_X / p-type poly-Si layers on both sides. (e) pppTOPCon lifetime specimens, where ppp indicates the p-type Cz-Si substrate combined with symmetrical thin SiO_X / p-type poly-Si layers on both sides. (f) npnTOPCon lifetime specimens, where npn indicates the p-type Cz-Si substrate combined with symmetrical thin SiO_X / n-type poly-Si layers on both sides.

SHJ: Experiments in this work were carried out on two types of n-type SHJ specimens sourced from EPFL. The samples were fabricated using 200 ± 10 µm thick, n-type silicon wafers with base resistivity of 2.0 ± 0.3 Ω.cm. The first type is a symmetrical lifetime structure with both sides passivated with a bilayer consisting of intrinsic amorphous silicon a-Si(i) /n-type doped amorphous silicon (a-Si(n)), as labelled as nnSHJ as shown in Figure 15.a, which has been fired in EPFL. The second type was cell precursor with a-Si(i)/ a-Si(n) on the front surface and a-Si(i)/ with p-type doped amorphous silicon (a-Si(p)) on the rear, as labelled as npSHJ as shown in Figure 15.b, which has been fired in EPFL. The 4-inch wafers were cut into quarters for further processing.

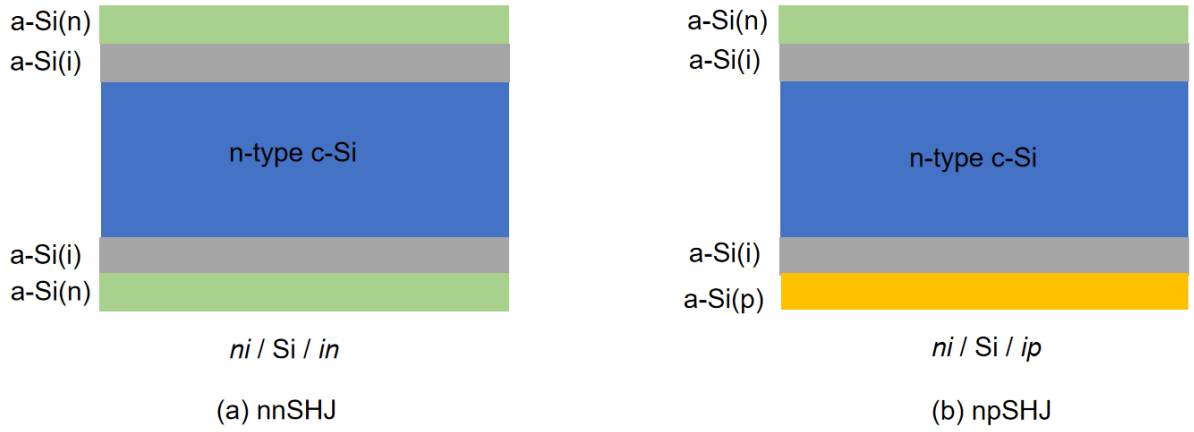

Figure 15. Schematic of the structure of tested SHJ lifetime specimens. (a) nnSHJ lifetime specimen, where nn indicates the symmetrical lifetime structures with both sides passivated with a bilayer consisting of a-Si(i) and a-Si(n). (b) npSHJ lifetime specimen, where np indicates the lifetime structures with a-Si(i)/ a-Si(n) on the front surface and a-Si(i)/ a-Si(p) on the rear side.

Table 1. Summary of silicon solar cell specimens used in this project.

Type	**Substrate Wafer**	**Dopant**	**Resistivity (Ω.cm)**	**Thickness (μm)**	**Sample size (cm)**	**Firing condition**	**Source**	**Identifier**
p-type PERC cell	p,Cz	B	1.2	180	1.5 × 1.5	Fired in UNSW	UNSW	PERC_UNSW
p-type PERC cell	p,Cz	B	0.9	170	1.5 × 1.5	Fired in Trina	Trina	PERC_Trina
n-type TOPCon cell	n,Cz	P	1.1	170	1.5 × 1.5	Fired in Trina	Trina	TOPCon cell
n-type TOPCon precursor	n,Cz	P	0.3-2.1	170	4 × 4	Fired in Trina	Trina	TOPCon precursor
n-type TOPCon	n,Cz	P	0.3-2.1	170	4 × 4	Fired in Trina	Trina	nnnTOPCon_ Trina_

lifetime specimen								
n-type TOPCon lifetime specimen	n,Cz	P	0.3-2.1	150	4 × 4	Fired in Fraunhofer	Fraunhofer ISE	nnnTOPCon_ Fraunhofer
n-type TOPCon lifetime specimen	n,Cz	P	1.5	280	4 × 4	Fired in ANU	ANU	pnpTOPCon
p-type TOPCon lifetime specimen	p,Cz	B	1.7	280	4 × 4	Fired in ANU	ANU	pppTOPCon
p-type TOPCon lifetime specimen	p,Cz	B	0.8	150	4 × 4	Fired in Fraunhofer	Fraunhofer ISE	npnTOPCon
n-type SHJ lifetime specimen	n,Cz	P	2.4	210	4 × 4	Fired in EPFL	EPFL	nnSHJ
n-type SHJ lifetime specimen	n,Cz	P	2.5	210	4 × 4	Fired in EPFL	EPFL	npSHJ

n-type Si wafer	n,Cz	P	30-60	675	4 × 4	Unfired	Oxford	n-Si wafer_Oxford

For dopant, B represents Boron and P represents phosphorus

3.2 Surface electric field generation

In this work, the control of the migration of hydrogen is achieved through a surface electric field. For industrial silicon solar cells, metal contacts are already present, and the electric field is achieved through the direct application of the voltage between the contacts. For the samples without metal contact, corona discharge is used to generate the surface electric field. Corona discharge technology can establish a metastable electric field across the hydrogen-containing dielectric layer without metal contact deposition [169]. The extrinsic surface charge can control hydrogen migration within the dielectric layer.

3.2.1 Dielectric synthesis via Plasma Enhanced Chemical Vapour Deposition

Plasma enhanced chemical vapour deposition (PECVD) is a vacuum synthesis technique that uses plasma to ionise gases, chemically nucleating and growing thin films on a substrate [170, 171]. SiO_X layer is deposited on the a-Si(n) side of the SHJ lifetime samples (SHJ_J and SHJ_K) at low temperatures via PECVD using the Oxford Instruments PlasmaLab 80+ system shown in Figure 16. Firstly, the chamber temperature is raised to 200 °C. Amorphous silicon degrades when the temperature exceeds 200 ~ 220 °C so this work required the development of a dielectric deposition method conducted at low temperatures. The SHJ_J and SHJ_K lifetime substrates are placed in the reaction chamber and the chamber is vacuumed to a pressure < 10^{-5} torr, ensuring that impurities in the environment do not interfere with the quality of the deposited film. Then, a gas mixture of Silane (SiH_4) and Nitrous Oxide (N_2O)) is introduced and reacted via plasma to promote the reaction:

$$SiH_4 + N_2O + \text{RF power} \rightarrow SiO_x + H_2 + N_2 \quad (3.1)$$

SiO_X layer is deposited on top of n-type doped amorphous silicon layers. Details about the parameter choice and procedure used for the low temperature PECVD SiO_X will be described in Chapter 6 since it required an optimisation process.

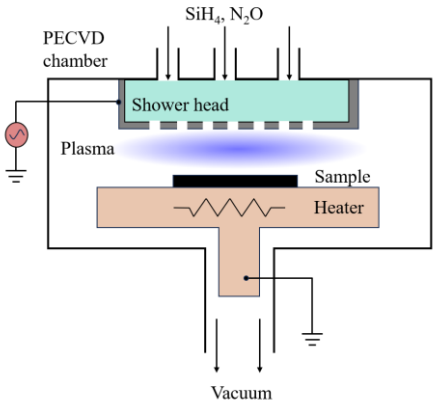

Figure 16. Schematic diagram illustrating the PECVD system used in this work.

3.2.2 Corona Discharge

Corona discharge is used as a method to build a surface electric field on the top dielectric layer of either TOPCon or SHJ lifetime [68, 169]. A corona discharge is achieved through the ionisation of the air molecules via the application of a high voltage to a metal pin as shown in Figure 17. The voltage applied is in the range of 0 ~30 kV. The ionised air molecules near the electrode form the corona-like shape plasma and drift the ionised air molecules to the sample which is placed on a ground plate. The polarity of the surface electric field on the substrate samples depends on the deposited charged ions. Corona with a positive voltage will deposit H_3O^+ molecules on the sample surface, while a negative voltage will deposit CO_3^- molecules [70, 172].

In this work, the lifetime specimens are placed below the tip of the source electrode and several modifications are applied to the standard corona discharge rig reported in [68, 169]. This work aims to achieve samples with different magnitudes of surface electric fields at different temperatures combined with light soaking. To achieve it, a new corona rig is developed to apply the continuous constant corona charge with different light illumination simultaneously shown in Figure 17. A lamp source (halogen or LED lamp) is added outside the corona charge box without impacting the inside corona-like shape plasma. The illumination intensity can be achieved between 0 and 1 sun through the change of distance between the lamp and the test specimen or lamp source. The hot plate is placed under the ground plate to achieve annealing between room-

temperature and 200°C. A mechanically affixed thermocouple and thermometer were used to adjust desired temperatures on the ground plate. The distance and the voltage are changed between the sample and tip to achieve variation of the surface electric field. To control the overall magnitude of the surface electric field on the specimen, the corona charge current is monitored before and after the corona discharge treatment through the current meter. The control of the corona charge current through the specimen is to ensure the same corona deposition rate is achieved on all samples even though they are made at different temperatures, with different illumination intensities, and different corona voltages.

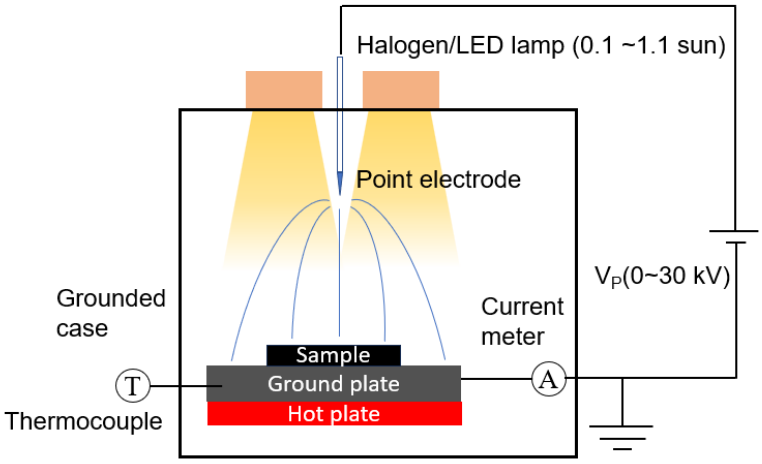

Figure 17. Schematic of corona charge box combined with light soaking annealing system.

3.3 Temperature-Dependent Current-Voltage Measurement

A six-terminal probe station is specially set up for this work and used to do in-situ dark current-voltage (I-V) measurement of PERC (PERC and PERC_m) and TOPCon solar cells with an extra bias added at elevated temperature in-between each I-V test, as shown in Figure 18.a. The solar cell is placed on the Al stage for the bias annealing and the IV measurements are taken before and after the treatment. The applied and measured current-voltage signals were supplied by two Keithley Source Meter Series 2401 separately, labelled SMU 1 and SMU 2 in Figure 18.a. Four probes connected with SMU 1 are used for the four terminal series resistance measurement of the cells during the bias annealing gap shown. Two probes are connected with the top metal contact of the cells and the other two are connected with the Al stage. Two probes connected with SMU2 are used to apply constant bias (voltage or current) during annealing. The hot plate underneath can offer various annealing temperatures and an electronic thermocouple is affixed to ensure that the temperature on the Al stage/silicon solar cells is controlled. In this project, a controlled I-V sweep measurement with extra applied

bias was performed periodically shown in Figure 18.b. During the bias annealing step, only SMU2 works and applies constant bias on the specimen. Once the bias annealing is finished, SMU2 is off and SMU1 is the only source taking the IV measurement. LabVIEW is used to control the signal for SMU 1 and SMU 2 in one program with different parameters set up. The detailed measurement set up and measurement paths for the PERC and TOPCon specimens will be discussed in brief within each results chapter.

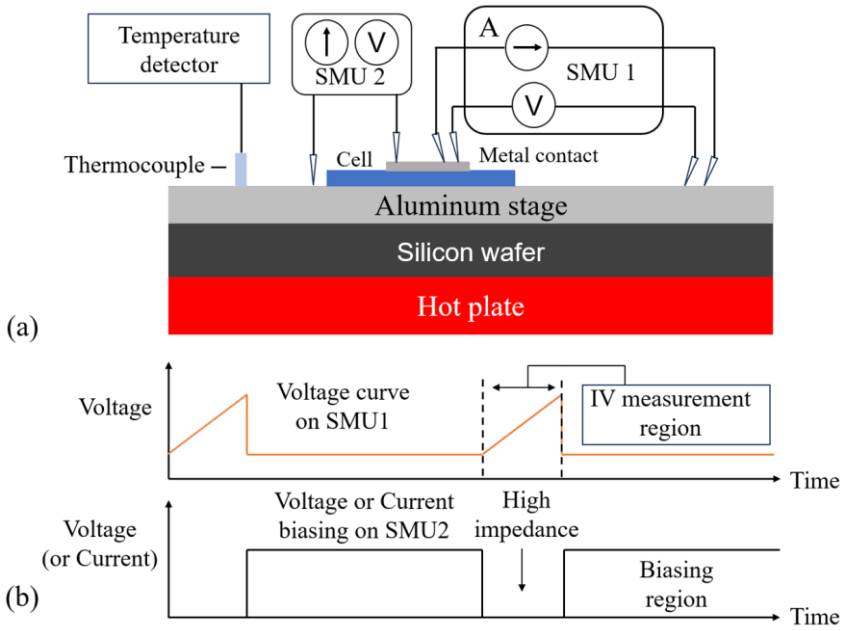

Figure 18. Schematic of measurement set up (a) Six-terminal probe station (b) Bias-Stress Measurements Workflow for SMU1 and SMU2 during treatment and measurement.

3.3.1 Four terminal resistance measurement

Four terminal resistance measurement is a method that separates the current-carrying and voltage-sensing electrodes, compared to the normal two-terminal sensing method [173, 174]. In the two-terminal sensing method shown Figure 19.a, the current meter measures the current through the whole loop, the measured resistance is the total resistance of the circuit.

$$R_{total} = R_{sample} + 2R_{wire} + 2R_{contact} \quad (3.2)$$

In the four-terminal sensing method shown in Figure 19.b, the two outer lines are used to provide a constant current and the two inner lines measure the voltage across the samples. The influence of resistance from the wire and contact is minimised in this set up. Due to the high resistance of the voltage meter, the wires

only carry a minuscule current and the voltage drop is negligible. Through the four-terminal method, more accurate resistance change can be recorded.

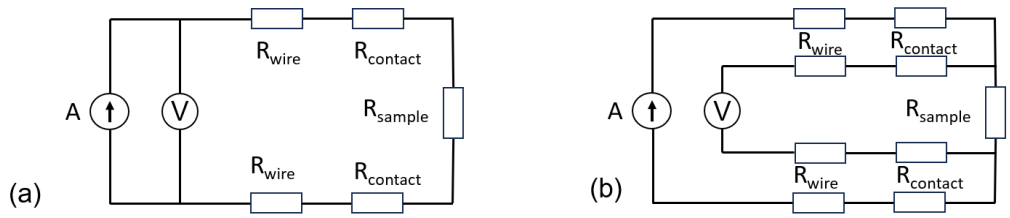

Figure 19. Schematic of resistance measurement (a) two terminal measurement (b) four terminal measurement [175].

3.3.2 Transmission Line Method

The transmission line method (TLM) was used to measure the contact resistance between the metal contact and a semiconductor, as well as the sheet resistance in the surface layer [176, 177]. Figure 20.a shows the simple resistor geometry in cross section. The measured total resistance consists of several components:

$$R_T = 2R_m + 2R_c + R_{semi} \tag{3.3}$$

Where R_m is the resistance of the contact metal, R_c is the contact resistance at metal/semiconductor interface and R_{semi} is the resistance of the semiconductor. In most situations, the resistance of the metal is low compared to the contact and semiconductor, so the R_T can be expressed as:

$$R_T = 2R_m + 2R_c + R_{semi} \approx R_{semi} + 2R_c = \frac{R_{sh}}{W}L + 2R_c \tag{3.4}$$

Where R_{sh} is the sheet resistance of the semiconductor, L is the length between the two contacts and W is the width of the contacts. According to equation 3.4, the measured total resistance between the two electrodes R_T is linearly related to the electrode spacing, and the intercept with the y-axis is twice the contact resistance. Therefore, by combining the linear fitting diagram shown in Figure 20.b., the corresponding values of R_C and R_{sh} can be calculated, and the transmission length can be further obtained through equation 3.5. Figure 20.c and Figure 20.d show the vertical view and cross-section view for the actual cell under TLM measurement. However, the current flow in the actual cell is more complicated. The current flow through the metal/semiconductor interface and current crowding occurs at the edge of the contact as shown in Figure 20.d [178]. The transfer length is used to describe the average distance that an electron/hole travels in the semiconductor beneath the contact before it flows into the metal contact [178]:

$$L_T = \sqrt{\frac{\rho_c}{R_{sh}}} \tag{3.5}$$

The effective area of the contact can be treated as $L_T W$.

$$R_c = \frac{\rho_c}{L_T W} = \frac{R_{sh} L_T}{W} \tag{3.6}$$

$$R_T = \frac{R_{sh}}{W} L + 2R_c = \frac{R_{sh}}{W} L + 2\frac{R_{sh} L_T}{W} = \frac{R_{sh}}{W}(L + 2L_T) \tag{3.7}$$

When performing the TLM technique, the total resistance R_T between two contacts is measured and plotted as a function of contact spacing L, as shown in Figure 20.b. Three parameters can be extracted from this plot: R_c , R_{sheet} , L_T . In this project, I performed the TLM measurements to isolate the contact resistance for both PERC and TOPCon cells. To do so, the busbar was removed from the cells by laser cutting to isolate the current path after three cycles of forward bias annealing. The total resistance was measured as a function of the distance between fingers. The finger pitch was ~1 mm measured with an optical microscope. The contact resistance was extracted from the intercept of the measured resistance vs distance curve as shown in Figure 20.b.

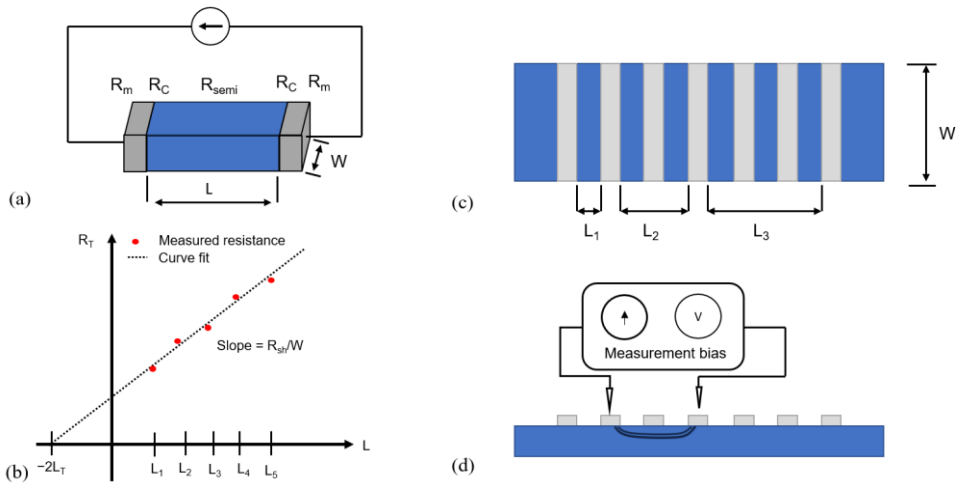

Figure 20. Schematic of TLM measurement. (a) simple resistor geometry in cross-section (b) the measured resistance vs distance curve (c) cell after removal of the busbar in vertical view (d) measurement set up for the cell in cross section.

3.4 Kelvin Probe Measurements

The Kelvin probe (KP) technique is used to measure the surface contact potential change of the specimens after corona discharge. The Kelvin probe measurement technology was proposed by Lord Kelvin in 1898 and

developed by William Zisman in 1932 [179]. It is a non-contact technique used to measure the surface potential difference between the metal probe and the substrate surface in vacuum or air conditions [179, 180], as shown in Figure 21.a. When the metal probe and the substrate sample are not connected in vacuum conditions, the surface potential of the metal probe is given by its work function Φ_m, while the surface potential of the substrate surface is Φ_s, as shown in Figure 21.b. When the probe is electrically contacted to the substrate surface, electrons would travel from the high work function material to the lower work function material, as shown in Figure 21.c, where the work function represents the electron energy difference between vacuum and Fermi levels. Therefore, the Fermi levels equalise and a contact potential will be established. In metals, this potential equates to the work function difference. Measuring work function requires a capacitor to be formed between the probe and the metal, as shown in Figure 21.a. The capacitance C is given by:

$$C = \frac{Q}{\Delta\Phi} = \frac{\varepsilon_0 A}{d_0} \tag{3.8}$$

Where Q is the charge held by the capacitor, ε_0 is the vacuum permittivity of the dielectric between the two ends of the capacitor, A is the effective area of the capacitor, d_0 is the distance between the probe and the test substrate surface, and the potential difference between the two ends of the capacitor is

$$\Delta\Phi = \Phi_m - \Phi_s \tag{3.9}$$

When the metal probe oscillates up and down periodically, the capacitance between the probe and substrate undergoes periodic changes, resulting on the change of the induced charge on the probe. This causes an alternating AC backing current flow

$$i_{AC} = \frac{dC}{dt}V \tag{3.10}$$

since the capacitance changes as

$$C = \varepsilon \times \varepsilon_0 \times \frac{A}{d_0 + \Delta d\, sin(\omega t)} \tag{3.11}$$

Where Δd is the vibration amplitude of the probe, ω is the vibration frequency of the probe. The probed current is hence given by:

$$i_{AC} = \frac{dQ}{dt} = \Delta\Phi\frac{dc}{dt} = -(\Delta\Phi\varepsilon\varepsilon_0 A\Delta d\omega)\frac{cos(\omega t)}{[d_0 + \Delta d\, sin(\omega t)]^2} \tag{3.12}$$

The work function difference is determined through Baikie's method [181]. The backing potential U is applied to the probe and i_{AC} is recorded, shown in Figure 21.d. When the reverse compensation potential U is added to the circuit and $d_0 >> \Delta d$, the AC backing current flow is given by:

$$I_{AC} = -(\Delta\varphi - U)(\varepsilon\varepsilon_0 A \Delta d\omega)\frac{cos(\omega t)}{{d_0}^2} \quad (3.13)$$

Through adjusting the compensation potential U, when the oscillating current flowing through the probe is neutralised, the surface potential of the substrate material is given by:

$$\Phi_s = \Phi_m - \Delta\Phi = \Phi_m - \mathrm{U} \quad (3.14)$$

All results here are reported for the compensation potential U, which in the field is also termed the contact potential difference CPD.

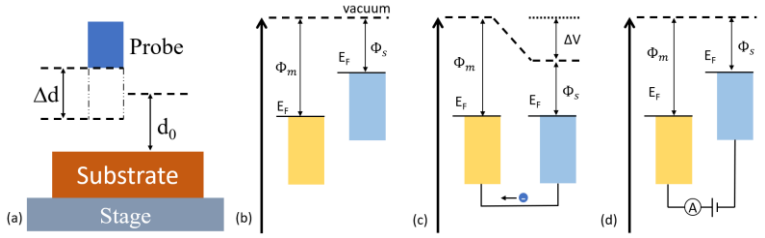

Figure 21. Schematic of kelvin probe apparatus and band diagram during the measurement. (a) kelvin probe apparatus (b) band diagram when the metal probe is not connected with the sample surface. (c) band alignment when the metal probe is connected to the sample surface. (d) impact of compensation potential applied.

3.5 Photoconductance Lifetime Measurement

The effective lifetime of minority carriers was evaluated by measuring the photoconductance decay on a Sinton WCT-120 Photoconductance Lifetime Tester. Photoconductance is a contactless method to extract the effective lifetime of a semiconductor specimen and was developed by Sinton and Cuevas in 1996 [182]. Figure 22 shows the schematic of the Sinton lifetime tester. An inductive coil creates a magnetic field above the specimen and induces Eddy currents. The conductivity of the specimen is extracted via an RF bridge that measures the impedance of the coil as changes occur to the carrier density of the nearby specimen. A high-intensity light is flashed on the specimen and electron-hole pairs are generated. A reference cell within the sample stage is used to measure the illumination stage during the flash decays. The conductivity change ($\Delta\sigma$) of the specimen is related to the concentration change of the minority carrier inside the silicon wafer by:

$$\Delta\sigma = q\Delta n\mu_n + \Delta p\mu_p = q\Delta n(\mu_n + \mu_p) \quad (3.15)$$

Where q is the electron charge, Δn and Δp are the concentration change of electrons and holes respectively, and μ_n and μ_p are the mobilities of electron and hole respectively.

If the photogeneration rate (G) and recombination rate (U) is assumed to be homogeneous throughout the wafer,

$$\frac{\partial \Delta n(t)}{\partial t} = G(t) - U(t) \quad and \quad U(t) = \frac{\Delta n}{\tau_{eff}} \tag{3.16}$$

The effective lifetime of specimen can be calculated as a function of time:

$$\tau_{eff} = \frac{\Delta n}{U(t)} = \frac{\Delta n}{G(t) - \frac{d\Delta n}{dt}} \tag{3.17}$$

In this work, measurements are carried out using the transient mode and quasi steady state mode (QSS), depending on the effective lifetime range [183]. The effective lifetime was measured when all the other light sources were turned off. For the specimen with an effective lifetime equal or above 100 µs, the transient mode is used for the measurement. For transient mode, a short pulse of light illumination is applied on the sample to excite excess carriers. The measurement is taken after the end of the light pulse so G(t)=0. Therefore, the effective lifetime is expressed as:

$$\tau_{eff} = \frac{\Delta n}{G(t) - \frac{d\Delta n}{dt}} = -\frac{\Delta n}{\frac{d\Delta n}{dt}} \tag{3.18}$$

For the specimen with effective lifetime lower than 100 µs, QSS mode is used for the measurement. For QSS mode, illumination of 10 times longer than the specimen's lifetime is applied on the specimen. Due to long time illumination, a steady condition is assumed. Therefore, the effective lifetime is expressed as:

$$\tau_{eff} = \frac{\Delta n}{G(t) - \frac{d\Delta n}{dt}} = \frac{\Delta n}{G(t)} \tag{3.19}$$

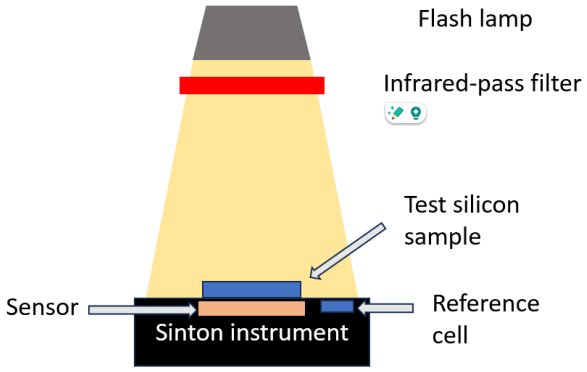

Figure 22. Schematic of the Sinton Lifetime tester.

From these data, the surface recombination velocity J_0 and open circuit voltage V_{oc} at 1 sun can be extracted[184, 185]. The effective lifetime is given by the sum of the bulk and surface components as discussed in section 2.3. The Sinton WCT-120 Photoconductance Lifetime Tester calculates these data following the Kane and Swanson slope method [182, 186]. For the excess carrier concentration Δn, the total recombination is given by:

$$\frac{\Delta n}{\tau_{eff}} = \frac{\Delta n}{\tau_{bulk}} + \frac{\Delta n}{\tau_{surface}} = \frac{\Delta n}{\tau_{bulk}} + \frac{J_0(N_d + \Delta n)\Delta n}{qWn_i{}^2} \tag{3.20}$$

Where W is the thickness of the specimen and N_d is the base doping concentration.

J_0 is the obtained from the slope of:

$$\frac{1}{\tau_{surface}} = \frac{\frac{1}{\tau_{eff}} - \frac{1}{\tau_{bulk}}}{\Delta n} \tag{3.21}$$

So that J_0 and V_{OC} are given by:

$$J_0 = \frac{qWn_i{}^2}{N_d + \Delta n}\left(\frac{1}{\tau_{eff}} - \frac{1}{\tau_{bulk}}\right) \tag{3.22}$$

$$Voc = \frac{kT}{q}\ln\left(\frac{J_{total,1sun}}{J_0 + J_{0,base}} + 1\right) \tag{3.23}$$

Where k is the Boltzmann constant, T is temperature and q is the magnitude of the elementary charge. $J_{total,1sun}$ represents the generated photocurrent with 1 sun illumination. $J_{0,base}$ represents the SRH recombination contribution under 1 sun illumination condition.

3.6 Photoluminescence Imaging

Photoluminescence (PL) imaging was developed by Trupke in 2006 and provides spatial information about recombination in silicon samples [187, 188]. When a semiconductor is excited by light with energy higher than its band gap, electrons are excited to the high-energy level. During the process of electrons returning to lower energy levels, energy is released. Recombination can occur radiatively or through the defect states. In PL imaging, the PL signal indicates the strength of radiative recombination, from which we can infer the carrier density, and thus the portion of defect-mediate recombination. Therefore, the quality of the silicon wafers can be correlated with the emitted photons after photoluminescence. The PL images presented in this work were taken with a CellSpot-ELPL imaging as shown in Figure 23. In this setup, the silicon wafer is placed on a non-luminescent baseplate. Two LED light sources are used to cause the silicon wafer to luminesce, and the photoluminescence is captured by the Nikon Z7Z6RM camera above the sample. The LED light source emits near-infrared noise which can distort the signal from the specimen. Therefore, filters are placed on the light source to eliminate much of the IR source. The illumination intensity is controlled by the magnitude of the current applied to the lamp. The overall emitted light is picked up by the detector and is converted into a pixel-by-pixel map of the sample. No information is provided regarding the light filtering as this is kept proprietary to the kit manufacturer. In this work, PL imaging is used to detect the cracks of the silicon wafer before the actual test and degradation or enhancement level after light soaking treatment.

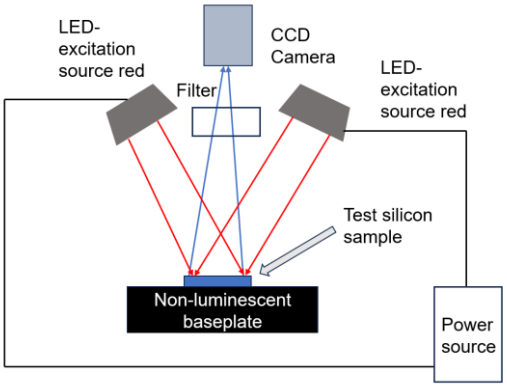

Figure 23. Schematic of the photoluminescence imaging system.

Chapter 4 Hydrogen-induced contact resistance at metal-semiconductor interfaces

4.1 Overview

This chapter investigates the contact resistance change of PERC and TOPCon specimens. Through the modification of PERC samples, different current paths to measure the sample resistance are achieved, elucidating crucial new insights into H-mediated interface degradation. IV and TLM measurements confirmed that the resistance changes for PERC and TOPCon during bias annealing happen at Ag/n-type silicon interfaces. The frequency of in-situ measurements also impacts the rate of change in contact resistance. Annealing before IV measurements can act to significantly increase this change rate in resistance, likely through an increase in the mobile hydrogen concentration at the Ag/n-type silicon interface. In addition, this chapter proposes a model explaining the hydrogen dynamics at the Ag/n-type silicon interfaces to correlate the observed contact resistance change during bias annealing.

4.2 Introduction

Chapter 2 explored the degradation dynamics in the PERC and TOPCon specimens. For PERC, the main recombination problem is light and elevated temperature-induced degradation (LeTID) [28]. Although the actual mechanism behind it is still unclear, a range of reports have provided evidence of the involvement of hydrogen in the formation of LeTID defects [29, 121, 189]. One approach to overcome this problem is a thermal treatment in the range of 300 °C – 500 °C, which is very effective in recovering V_{OC} in PERC cells [190]. However, this treatment can cause severe deterioration of the fill factor (FF), which is dominated by an increase in series resistance (R_S) [30, 123, 124]. Previous observations indicated that the change in R_S is related to a flow of charged particles with hydrogen as a likely candidate since it is known to be mobile at room temperature [125]. Therefore, studying the change in series resistance during annealing and finding a method to control the degradation process can help us understand hydrogen kinetics inside the PERC samples.

For TOPCon solar cell, performance is not affected by BO-LID since the use of n-type silicon as the main substrate reduces the BO defects, but LeTID is still observed in n-type silicon specimens [105, 191]. And this degradation is related to the firing-induced deterioration in passivation schemes [32, 33]. It has been reported that post-metallisation annealing in the range of 300 ℃ and 400℃ can help to mitigate this degradation, which is highly similar to the method used to mitigate LeTID in PERC structures [131]. It is hence possible that there is a link between the formation of the detrimental defects and the following thermal annealing treatment, and that such a link relates to the behaviour of hydrogen in these cell structures.

Hydrogen is almost impossible to be directly detected when working with solar cells. Therefore, in this work, I used the change in series resistance as the method to investigate the hydrogen kinetics inside of these architectures.

In this chapter, the impact of hydrogen induced contact resistance (HICR) in industrial PERC and TOPCon solar cells is studied. Industrial commercial PERC and TOPCon cells were used in this study. I demonstrate that HICR occurs both in TOPCon and PERC solar cells. The application of cycling forward current and reverse bias conditions controls the speed and extent of the contact resistance degradation. The degradation occurs purely at the n-type Si to silver contact on both cell architectures. Lastly, I propose a hypothesis by which these changes occur, based on the impact of the applied electric fields on the concentration and movement of charged hydrogen particles at the silicon surface.

4.3 Experiment Set Up

The series resistance change (ΔR_S) of solar cell specimens (PERC, mPERC and TOPCon) were tested in a dark box during annealing under an applied bias, as described in Chapter 3. ΔR_S was extracted in the range of 0-0.2 V forward bias using the initial R_S at elevated temperature as the reference value. I-V characterisation was performed before and periodically during annealing. I established a system to control heating temperature, applied bias, and measurement frequency, to produce different experimental conditions that lead to changes in the series resistance of the different specimens.

Figure 24.a illustrates the geometry of the original PERC cell received from UNSW and the measurement set-up used to measure series resistance from the front Ag contact to the rear Al contact, including resistance inside the device structure, labelled as current path ①. In this work, a new modified geometry is developed to

enable measuring different components of series resistance separately. Figure 24.b shows a schematic of the measurement set-up with the second direct aluminium front contact to the emitter. Four sets of measurements were performed to obtain the resistance change between (i) the front Ag finger and the rear Al contact in the original PERC specimen (① in Figure 24.a), (ii) the front Ag finger and the rear Al contact in the modified PERC specimen (① in Figure 24.b), (iii) the front Ag finger and the new front Al contact of a modified PERC specimen (② in Figure 24.b) and (iv) the front Al and the rear Al contacts of modified PERC specimen (③ in Figure 24.b). Original and modified samples were measured at 400℃ for a total of 180 minutes with intervals of forward and reverse (± 0.5V) biases applied for 30 min each, periodically, in between each measurement. This technique is referred to as 'biased annealing'.

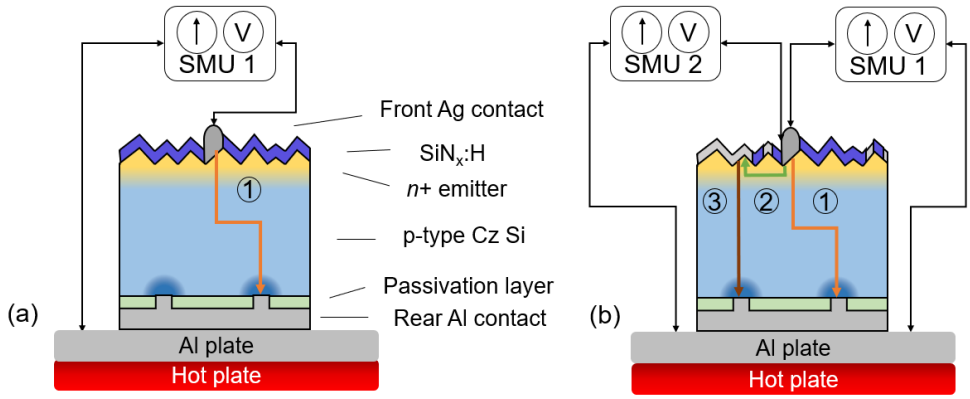

Figure 24. Schematic of the measurement model for samples with different geometry. (a) unmodified geometry and circuit: ① Measurement from front Ag to rear contact. (b) modified geometry and circuit: ① Measurement from front Ag to rear contact ② Measurement from front Ag to front Al ③ Measurement from front Al to rear contact.

After confirmation of the origin of the increase in the series change of PERC specimens from UNSW during bias annealing, further experiments were tested on the original PERC received from Trina and TOPCon cells from Trina. The shift of the PERC specimens from UNSW to Trina was caused by the run-out of the samples from UNSW. Figure 26.a illustrates the contact arrangement for measurements on PERC from Trina, which measured ΔR_S between the front Ag contact to the back Al contact. Figure 26.b illustrates the contact arrangement for measurements on TOPCon cells, which measured ΔR_S between the rear Ag contact to the front Ag contact. As the polarity of the TOPCon cell was reversed compared to PERC, the cells were flipped upside down so that I could use the same measurement polarity, as shown in Figure 26.b. The polarity of the bias used follows the convention for a p-n junction, i.e. forward bias means positive bias on the p-type side.

I hypothesise that the observed the R_S change is caused by the diffusion of the charged H ions during the bias annealing process, so R_S change should be proportional to the mobile atomic hydrogen concentration around the interface. Then, the impact of the bias annealing conditions on the R_S change of the PERC and TOPCon specimens is studied. Figure 25 illustrates the flow chart of the experiment process. At first, the impact of the annealing temperature on the R_S change of the PERC and TOPCon specimens is investigated, as shown in Figure 25.a. The same bias conditions are applied on the PERC and TOPCon specimens with a cycle of 500 mA forward current for 30 minutes followed by 2.5 V reverse bias for 30 minutes. The specimens were subjected to a total of 150 minutes bias annealing process at different annealing temperatures (350 ℃, 375 ℃ and 400 ℃) and the R_S change was measured during the process. After that, the influence of bias stress conditions on the R_S change of the PERC and TOPCon specimens is investigated, as shown in Figure 25.b. The specimens were subjected to a total of 180 minutes with 3 cycles of different forward currents (10 mA, 100 mA and 500 mA) for 30 minutes followed by 2.5 V reverse bias for 30 minutes at 400 ℃. R_S change was measured during the whole process. During the annealing treatment, the generation of the atomic hydrogen and diffusion of hydrogen atoms happened at the same time [192, 193]. To mitigate the impact of the initial atomic H concentration difference in the PERC specimens from UNSW on the further R_S change during bias annealing treatment, the specimens have been through the pre-annealing procedure with 2.5 V reverse bias at first. A set of samples were pre-annealed for 2 h at different temperatures from 325 to 400 ℃. Then samples were subjected to a total of 80 minutes process with 4 cycles of 10 mA forward bias for 10 minutes followed by 2.5 V reverse bias for 10 minutes at 400 ℃. Another set of samples were pre-annealed at 400 ℃ for different duration times between 0 and 22 hours to separate the effects of temperature and time. Then these samples were subjected to a total of 90 minutes process (4 cycles of 10 mA forward bias for 10 minutes followed by 2.5 V reverse bias for 10 minutes and followed by an extra 10 minutes of 10 mA forward bias treatment) at 400 ℃. For the pre-annealed specimens, mobile atomic hydrogen has already distributed through the whole cell [193], the impact from the bias should be dominant. I reduce the forward current during the IV measurement from normal 500 mA to 10 mA to see how sensitive for the pre-annealed specimens to the bias annealing treatment.

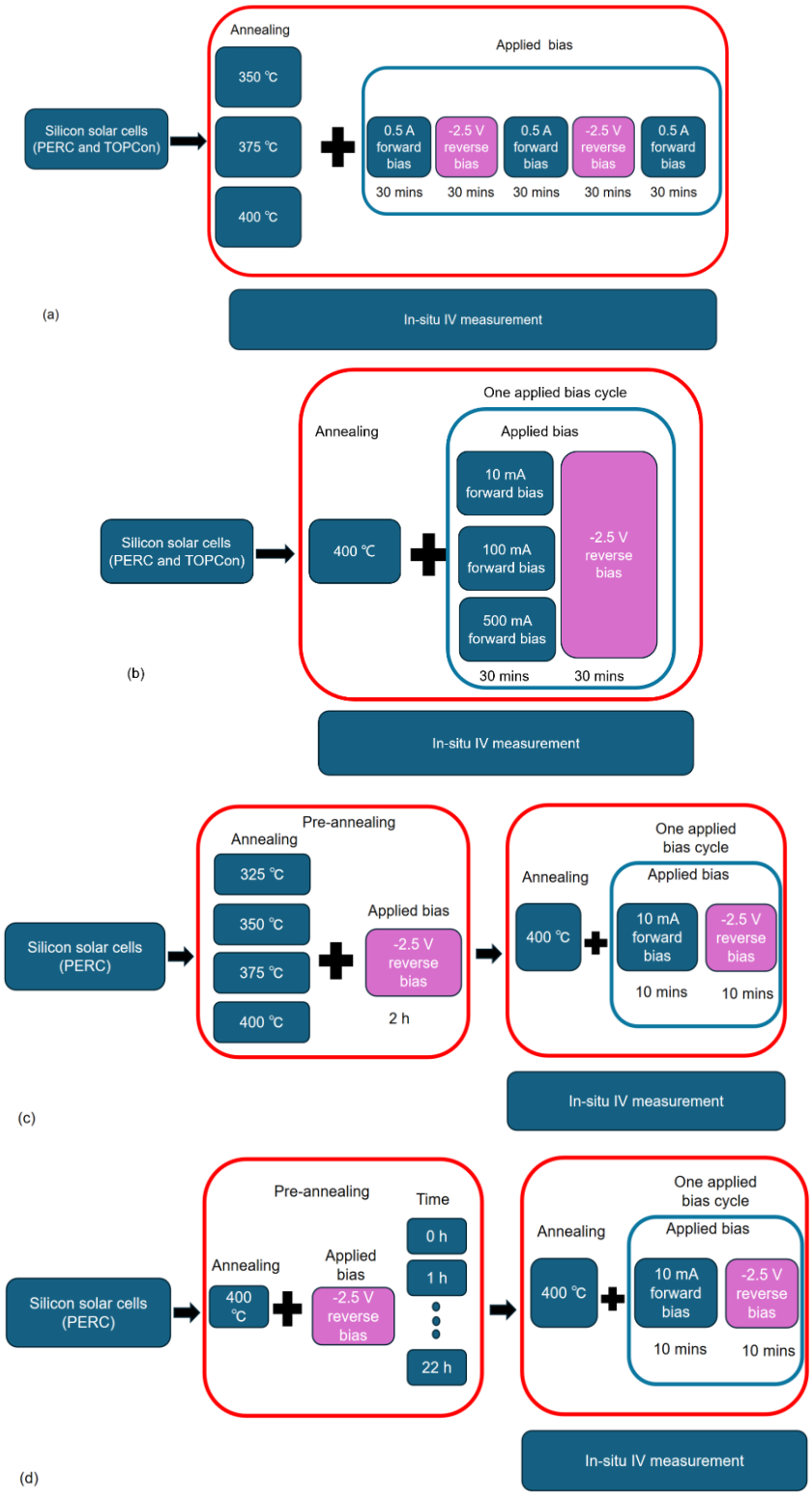

Figure 25. Flow chart of experiment process. (a) R_S change of the PERC and TOPCon specimens with different annealing temperatures and the same bias condition during the bias-annealing process. (b) R_S change of the PERC and TOPCon specimens with different bias conditions and the same annealing temperature during the bias-annealing process (c) R_S change of the PERC specimens during the bias-annealing process after pre-annealing process with different pre-annealing temperatures at the same duration. (d) R_S change of the PERC specimens during the bias-annealing process after pre-annealing process with different durations at the same pre-annealing temperature.

Transmission line method (TLM) measurements were performed to isolate changes in the contact resistance for both cell architectures. To do so, the busbar was removed from the cells by laser cutting to isolate the current path after three cycles of forward bias annealing. The total resistance was measured as a function of the distance between fingers. The finger pitch was ~1 mm measured with an optical microscope. The contact resistance was extracted from the intercept of the resistance vs distance curve as detailed in Section 3.3.2.

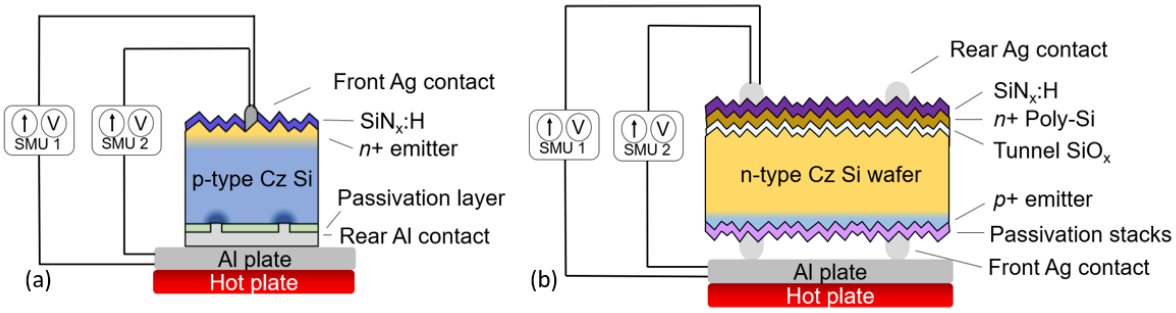

Figure 26. Schematic diagram (not to scale) of the measurement set up for observing in-situ changes in series resistance for PERC cells and TOPCon cells. (a) PERC_B cells (b) TOPCon cells.

4.4 Origin of the series resistance increase in PERC

Reports in the literature have shown that the application of an electric field impacts the nature of changes in R_S in PERC solar cells [124]. However, many aspects of the cell can contribute to increased R_S. To isolate the region of the cell leading to severely increased R_S, I designed a modified cell mPERC, as depicted in Figure 24.b, which allows for the isolation of three distinct current pathways.

First, I performed in-situ monitoring on an original standard PERC specimen from UNSW to replicate the results in Ref. [30], using current pathway ① in Figure 24.a. In pathway ①, the R_S can be impacted by (i) the front Ag / Si interface contact resistance (in contact with n+ emitter), (ii) resistance in the silicon bulk and (iii) the rear Al / silicon interface contact resistance. A forward bias of 0.5 V was applied for a 30 min interval, followed by an equal magnitude reverse bias for a 30 min interval at a temperature of 400 ℃. The changes in R_S were monitored in-situ and are displayed in Figure 27.a. The application of a forward bias causes a significant increase in R_S. An increase of ~ 100 $\Omega \cdot cm^2$ is observed after 60 mins of exposure to forward bias. The subsequent application of reverse bias leads to a suppression of R_S, however, the R_S does not return to the initial value. This result closely matches the previous observations in Ref. [124].

The modified PERC structure was fabricated from original PERC cells to provide a deeper insight into the cause of changes in the R_S. Before exploring the impact of different current pathways, the change in R_S through pathway ① in the modified cell is measured to verify that the fabrication sequence did not alter the behaviour. The result for pathway 1 in the modified cell is displayed in Figure 27.b. In this case, the application of forward bias leads to a significant increase in the R_S and the application of reverse bias suppresses this increase. The response to the bias very closely resembles that for the original PERC cell shown in Figure 27.a. while R_S increases with the application of forward bias and decreases with the application of reverse bias. The R_S change is saturated around 100~200 $\Omega.cm^2$ after the 3rd forward bias treatment. ΔR_S between the front Ag to back Al could attain its highest value around 200 $\Omega.cm^2$ in the 3rd forward bias treatment for the original PERC, while ΔR_S between the front Ag to back Al could attain its highest value around 300 $\Omega.cm^2$ for the modified PERC. The difference of the highest R_S change could be related to the difference in sample (such as defects around the interface and H concentration). Compared to the initial R_S with the value of 2~3 $\Omega.cm^2$, the change caused by the bias is more pronounced, so ΔR_S is used as the main factor in the further test. These results indicate that the subsequent sample preparation did not impact the response to HICR.

To isolate the contribution of the front surface on the change in R_S, current pathway ② in the modified cell was tested. Pathway ② is displayed schematically in the green line in Figure 24.b. In this pathway, contributions to R_S come from (i) the front Ag / Si interface contact resistance, (ii) the sheet resistance of the n+ emitter and (iii) the front Al / silicon interface contact resistance. For this test, the front Ag metallisation is the industrial screen-printed fingers while the front Al contact was thermally evaporated following SiN_X removal as shown in Figure 24.b. The change in R_S under forward and reverse bias conditions for pathway ② is displayed in Figure 27.c. These results very closely resemble those of pathway ①, shown in Figure 27.b. The application of a forward bias leads to a significant increase in R_S. The magnitude of the increase in R_S is higher than for current pathway ①. Indeed, values of $R_S > 10\ \Omega \cdot cm^2$ are already extremely large and could cause the loss of the fill factor ~50% relative [30]. The reverse bias causes a recovery of R_S. For pathway ②, the impact of resistance in the wafer bulk and the rear Al / Si interface are eliminated. The observation that the change in R_S appears very similar to pathway ① indicates that the bulk and rear contacts do not play a significant role in the increased R_S.

To test this hypothesis, current pathway ③ is tested, displayed schematically in brown in Figure 24.b. In this pathway, contributions to R_S come from (i) the front Al / Si interface contact resistance, (ii) the

resistance in the wafer bulk and (iii) the rear Al / silicon interface contact resistance. As such, this is the only result without the contact resistance at the front Ag / Si interface. The change in R_S for pathway ③ is shown in Figure 27.d. The results shown here are substantially different to the other three cases. The application of forward bias does not lead to a substantial increase in R_S. In fact, the R_S reduces slightly. The first cycle of reverse bias also decreases R_S, however, subsequent cycles cause a slight increase in R_S. This behaviour indicates that the aspect of the cell causing the large increases in R_S is not present in pathway ③. Therefore, I conclude that the contact resistance at the front Ag / Si interface with the n+ emitter is the primary cause of HICR in PERC.

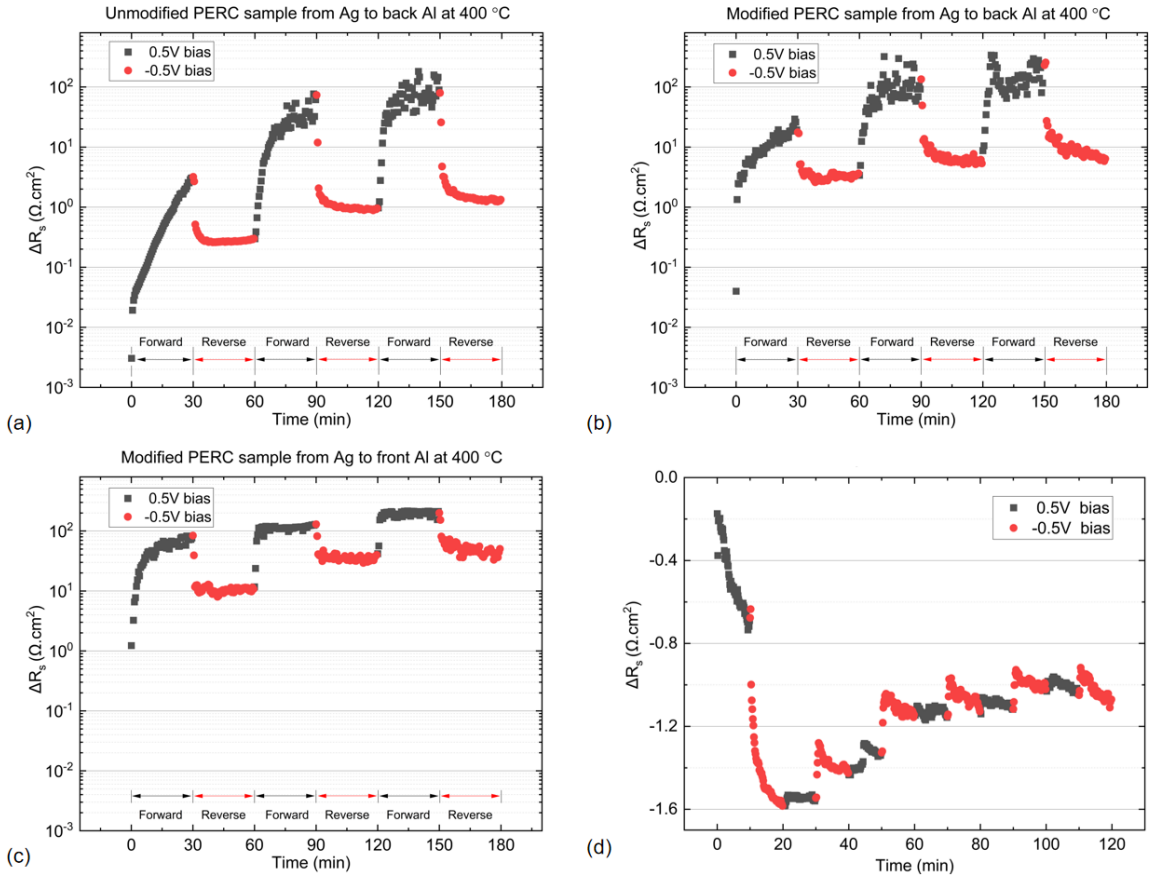

Figure 27. The series resistance changes of the previous path and new path of modified and original PERC specimens. (a) original path ①: Δ as a function of annealing time and applied bias between the Ag and rear Al contacts for the unmodified specimen. (b) modified path ①: ΔR_S as a function of annealing time and applied bias between the Ag and rear Al contacts for the modified specimen. (c) modified path ②: ΔR_S as a function of annealing time and applied bias between the Ag and front Al contacts for the modified specimen. (d) modified path ③: ΔR_S as a function of annealing time and applied bias between the front Al and rear Al contacts for the modified specimen. Only one sample was used for each bias annealing condition.

4.5 Influence of temperature in R_s for PERC and TOPCon during bias annealing process

In the previous section, it was demonstrated that HICR occurs at the Ag/n-type Si interfaces in PERC samples. Due to the similarity of thermal treatments to mitigate the SRD in TOPCon and LeTID in PERC cells, I study the potential for such thermal treatments to lead to hydrogen induced contact resistance in both of these cell architectures jointly. In the last section, 0.5 V forward bias is used to increase the R_S during the bias annealing. With the increase of the R_S at the Ag / n-type Si interface, the current across the whole cell is decreased, which leads to the decrease of voltage bias across the junction and substrate. The saturation of R_S could be related to the decrease of the driving force for the charged ions across the junction region to the interface. To mitigate that impact, I switch a forward bias to a forward current for the forward bias annealing process, so a constant bias is applied across the substrate and junction region. As shown in Figure 27, 0.5 V reverse bias can mitigate the R_S change from 100 $\Omega \cdot cm^2$ to 10 $\Omega \cdot cm^2$, but cannot reverse it to its initial value. The strength of reverse bias with a value of 0.5 V might not be enough to mitigate the impact of the forward bias annealing. Therefore, I increase the value of the reverse bias from 0.5 V to 2.5 V for the further test.

Figure 28 displays the response of both PERC and TOPCon solar cells from Trina, as described in Section 3.1, to the bias-controlled annealing process in the range from 350 °C – 400 °C. The result for the PERC cell, as shown in Figure 28.a, closely resembles that in Figure 27.a. At 400 °C, a significant increase in R_S is observed following the application of a forward current. Subsequent reverse bias annealing immediately suppresses this change. However, for lower temperatures, the change in R_S is much less pronounced. This indicates that the temperature has a large impact on the kinetics of hydrogen induced resistance change in PERC cells. For the TOPCon cell shown in Figure 28.b, the result at 350 °C is different to PERC. The PERC cell is remarkably stable over the duration of the repeated forward current and reverse bias, however, the TOPCon cell does display some increase in R_S, on the order of approximately 2 $\Omega \cdot cm^2$. At 375 °C, this difference in the response is even more pronounced. For the 400 °C case, the trend of the contact resistance change is similar for PERC and TOPCon, however, the magnitude of change in R_S is larger for PERC at the 3rd forward bias treatment cycle. These results demonstrate that TOPCon solar cells are also susceptible to increased R_S when exposed to thermal treatments during the bias annealing process, which has a significant impact on cell efficiency. The increase of the annealing temperature will lead to an increase in the R_S change

during the forward bias annealing process. Besides that, increase of the reverse bias voltage to 2.5 V still cannot totally mitigate the R_S change during forward bias annealing.

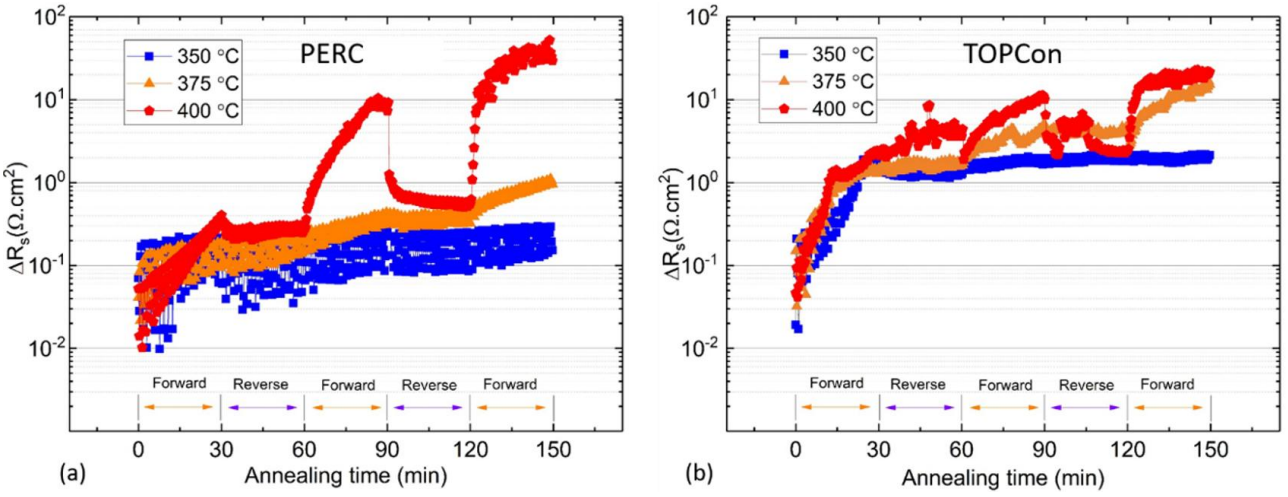

Figure 28. ΔR_S as a function of annealing time at various temperatures for (a) PERC and (b) TOPCon solar cells. The samples were subjected to a cycle of 500 mA forward current for 30 minutes followed by 2.5 V reverse bias for 30 minutes. Only one sample was used for each annealing condition.

4.6 Influence of stress biasing conditions

In the previous section, I studied the impact of the annealing temperature for the R_S change for the PERC and TOPCon specimens during bias annealing process and I demonstrated that the bias polarity-controlled series resistance changes were observed on both the TOPCon and PERC architectures. To study the impact of the strength of the applied electric field on the contact resistance change, I varied the magnitude of the applied forward bias on the PERC and TOPCon specimens from Trina during bias annealing process. Figure 29 displays the response of both PERC and TOPCon solar cells to the bias-controlled annealing process with forward biases of 10 mA, 100 mA and 500 mA at 400 °C. The reverse bias was kept the same in all cases, at 2.5 V. With 500 mA forward bias, a significant increase in R_S is observed in both architectures. However, the subsequent reverse bias annealing does not have an identical response. In PERC, a rapid suppression is observed in Figure 29.a, whereas the reduction under reverse bias in TOPCon is less pronounced in Figure 29.b. The minimum level of change in R_S following three cycles is thus significantly lower for PERC than TOPCon.

Reducing the applied current to 100 mA further illustrates the difference in response. In PERC, the R_S profile under forward and reverse bias very closely resembles that of the 500 mA case. However, in TOPCon

at 100 mA shown in Figure 29.c, the first two cycles of forward bias have far less impact on the R_S. The R_S increases with increase of the annealing time and the switch between the forward bias to reverse bias doesn't suppress this increase. A similar observation is made at 10 mA as shown in Figure 29.c. For TOPCon cells with 10 mA forward bias and 2.5 V reverse bias, a continuous increase in R_S is observed and bias has negligible impact on the change. The increase in resistance can be primarily attributed to the temperature. The difference in response indicate that the cell structure impacts the movement of hydrogen to the contacts differently. The forward bias used has a large impact on the kinetics of hydrogen induced resistance change in PERC and TOPCon cells, which would have a significant impact on cell performance for different in-field operating conditions.

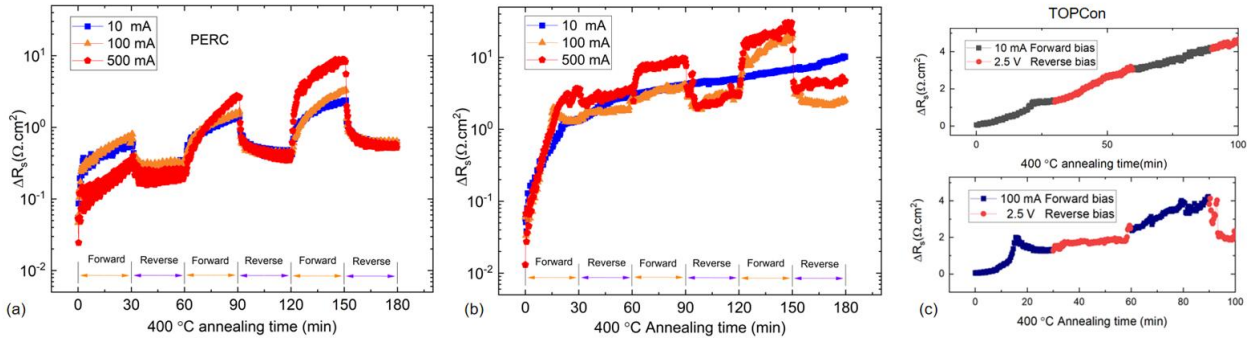

Figure 29. ΔR_S as a function of annealing time at various forward biases at 400 °C for (a) PERC (b) TOPCon solar cells and (c) comparison of the ΔR_S for TOPCon specimens for the first two cycles of forward bias with different magnitude. Only one sample was used for each bias condition.

4.7 Influence of measurement frequency

As described in the methodology in Chapter 3, the stress biasing source SMU2 is turned off during I-V measurements. The unit used for I-V characterisation, SMU1, applies a stair function of current while capturing voltage. This procedure could impact the mobile charged H species inside the structure. It would follow that the frequency at which the measurements are performed would impact the results. To explore this hypothesis, I set up an additional experiment where the rate of measurement was adjusted.

Figure 30.a shows the measured ΔR_s with alternating forward and reverse applied bias for three different measurement frequencies and biasing durations for the PERC samples from UNSW for the 420 minutes of stress bias-annealing process at 400 °C. The samples were measured 60 times for one forward bias (500 mA) cycle, and 60 times for the reverse bias (2.5 V) cycle for the IV measurement process as shown in Figure 30.c.

During each measurement cycle, the time intervals for the application of the bias form SMU2 is varied between 20, 60, and 180 seconds to study the impact of the measurement frency on R_S change of the PERC specimens during the bias annealing process, as shown in Figure 30.b. It is identified that the frequency of the measurements not only increases the rate at which the resistance increases, but also significantly increases the value of the resistance. ΔR_s increased by almost three orders of magnitude in the first 20 minutes when the measurements were performed every 20 seconds. However, the increase is less than an order of magnitude for the same duration when the measurements are performed every 180 seconds. The final values of ΔR_s also differed significantly where the sample measured every 20s saturated around 200 $\Omega.cm^2$ after 300 min measurement, while the sample measured every 180s only reached around 2 $\Omega.cm^2$ after 400 min measurement. The apparent difference of R_S change in PERC from UNSW is due to the difference in measurement condition. This demonstrated the importance of maintaining an identical measurement frequency when comparing results.

It is also important to note that ΔR_s ΔR_sbecome unstable and unreliable once it exceeds ~ 20 $\Omega.cm^2$. Therefore, comparisons amongst samples were performed at an identical measurement frequency at which measured ΔR_s values were stable and reliable, normally in the range <20 $\Omega.cm^2$.

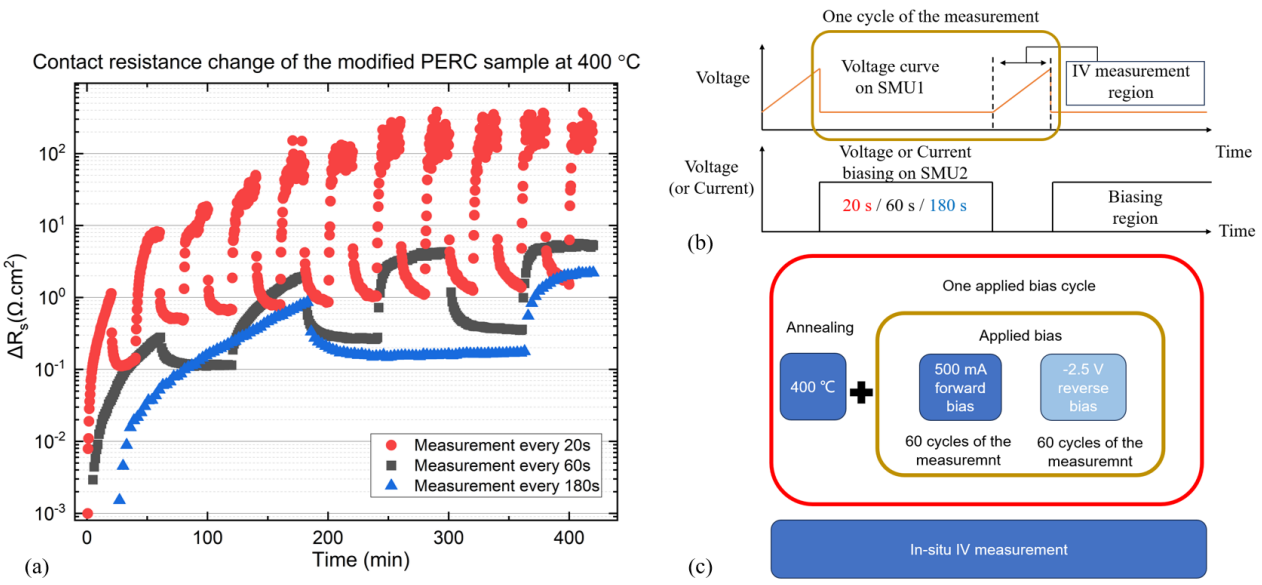

Figure 30. Results and experimental flow chart for the influence of the measurement frequency test. (a) ΔR_S as a function of annealing time and applied bias for the PERC sample with a period between measurements of 20 s (red) ,60s (gray) and 180 s (blue). Only one sample was used for each measurement frequency condition. (b) Bias-Stress Measurements Workflow for SMU1 and SMU2 during measurement. (c) experimental flow chart of the IV measurement process.

In the measurement set up for Figure 30.c, the bias duration time for each bias cycle was different. To separate the impact of the bias annealing time and measurement frequency, the impact of the measurement frequency experiment was repeated while keeping the bias duration constant rather than the number of measurements and adjusting the measurement intervals, as shown in Figure 31.c. Because the PERC specimen from UNSW ran out, this experiment was shifted to the PERC specimens from Trina. Figure 31. shows the ΔR_S for PERC and TOPCon specimens from Trina under different measurement frequencies with the same duration time. Figure 31.a shows that ΔR_s for the PERC sample and the change in measurement intervals had minimal impact on ΔR_s observed. The specimen measured every 20 s, 60 s and 180 s have approximately the same ΔR_s /dt.

For TOPCon measured every 20s, a significant increase in ΔR_s with forward bias is observed, with a subsequent reduction under reverse bias, as shown in the blue line in Figure 31.b. For TOPCon measured every 60s, a significant increase in ΔR_S with 1st forward bias cycle is observed with less ΔR_S /dt compared to the specimen measured every 20s. However, the subsequent 1st reverse bias cycle annealing does not have an identical response. ΔR_S increases from 1 to 3 $\Omega.cm^2$ at first and then draws back to 2 $\Omega.cm^2$ under 1st reverse bias cycle as shown in the orange line in Figure 31.b. For TOPCon measured every 60s, a similar increase in R_S with 1st forward bias cycle is observed, compared to the specimen measured every 60s. R_S is still increasing under the subsequent 1st reverse bias cycle annealing with small ΔR_S /dt, as shown in the red line in Figure 31.b. For the TOPCon specimens measured every 60 s and 180 s, the change under reverse bias is more pronounced in the 2nd and 3rd cycles. The impact of measurement frequency is observed in PERC from group A and TOPCon cells from group C. There was almost no impact of measurement frequency for PERC specimens from Trina.

Considering the link between LeTID and HICR, I speculate that the differences observed in different specimens may originate from differences in H concentration, or changes in the Ag/Si interface morphology of each specimen. When metal contacts a semiconductor, it produces a Schottky barrier contact with a high concentration of interface states. These charge states can be occupied by the mobile atomic hydrogen during annealing and cause an increase in the barrier height. For the PERC specimens from UNSW, R_S increased to almost 60 $\Omega.cm^2$ after 150 mins 500 mA forward bias annealing treatment with measurement every 20 s, while R_S increased to almost 1 $\Omega.cm^2$ s with measurement every 180 s, as shown in Figure 30. For the PERC specimens from Trina, R_S increased to almost 10 $\Omega.cm^2$ after 150 mins 500 mA forward bias annealing

treatment with measurement every 20 s, while R_S increased to the same value with measurement every 180 s, as shown in Figure 31.a. The change in R_S for the PERC from Trina is less than the R_S change in PERC from UNSW with measurement every 20s at the same bias annealing conditions. The less R_S change could be related to the fewer interface states in PERC from Trina, compared with the PERC from UNSW. For the PERC specimens from Trina, the hydrogen concentration might be large enough for the interface states at the Ag/Si interface, so the change of measurement frequency has less impact, compared with the specimens from UNSW. The different responses for the R_S change in PERC from UNSW and Trina to the measurement frequency should be related to the difference in specimens. These results would hence show that the manufacturing conditions are of importance for the final H concentration, yet further investigation is required to isolate the underlying mechanisms. Besides that, to study the series change of the solar cells at elevated temperatures, the measurement condition should be kept at the same condition, due to the interface passivation quality change caused by the diffusion of charged ions (hydrogen) driven by the electric through the whole cell. The IV measurement condition affected the measured R_S change during the bias annealing process and might lead to the measured R_S change to a different extent for the different specimens. The possible mechanism behind this phenomenon will be discussed in Section 4.10 Discussion part.

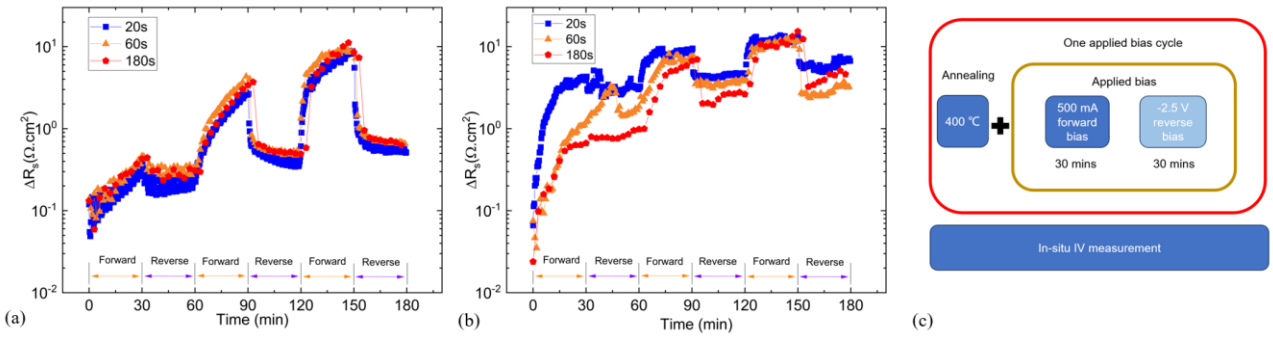

Figure 31. ΔR_S as a function of annealing time and applied bias for (a) PERC and (b) TOPCon sample with a period between measurements of 20 s (blue), 60s (orange) and 180 s (red). Only one sample was used for each measurement frequency condition. (c) experimental flow chart of the IV measurement process.

4.8 Influence of pre-annealing

This work indicates that the change of series resistance during annealing appears to be related to the conditions of the charged H species, which respond to an electric field polarity, and hence the changes are controlled by the bias conditions [30]. Provided that the cause of increased R_S is hydrogen passivation of the

interface, such ΔR_S should be proportional to the mobile hydrogen concentration in the structure available to passivate. Hydrogen is released from dielectric layers during firing and hydrogen atoms are trapped in unstable forms such as hydrogen complexes bound to the impurities or hydrogen dimers during the subsequent rapid cooling process [138, 190, 194-196]. Subsequent annealing causes a change in the concentration of available H concentration through an increase in the overall concentration of the mobile atomic hydrogen atoms during thermal processing [196, 197]. To investigate the impact of increased H concentration on ΔR_S, samples have been pre-annealed and different pre-annealing conditions have been tested.

Figure 32.a shows the series resistance changes of four samples pre-annealed with 2.5 V reverse bias at four different temperatures between 325-400 ℃ for two hours before being bias-stressed and I-V characterised for 80 minutes under alternating forward and reverse bias at 400 ℃. For the specimens pre-annealed for 2 h below 350℃, the application of forward bias does not lead to a significant increase in R_S after 4th forward bias cycle at 400 ℃. The ΔR_S of the specimen pre-annealed for 2 h at 375℃ increased to 1 $\Omega.cm^2$ after 4th forward bias cycle at 400 ℃, while ΔR_S of the specimen pre-annealed for 2 h at 400℃ increased to 3 $\Omega.cm^2$ at the same condition. The results demonstrate that higher temperature pre-annealing condition causes a faster and higher increase in ΔR_s with the same applied bias. It confirms that the concentration of active H species involved in the R_s increase depends on pre-annealing temperature. The results also suggest that the mechanisms causing front contact increases are boosted at 400° in comparison with lower temperatures. Hence, I decided to perform I-V characterization at 400° C and investigate the effect of pre-annealing duration on contact resistance changes. Figure 32.b shows the series resistance change of six samples pre-annealed at 400 ℃ for different durations from 0 to 370 minutes under 2.5 V reverse bias before being forward-bias stressed and I-V characterised for 20 minutes under 10 mA bias. Figure 32.b shows that the increase of the pre-annealing time increases the rate of resistance change. The highest resistance change occurred in the sample with 290 mins pre-annealing, where ΔR_S was above 10 $\Omega.cm^2$ after only 20 mins measurement. However, samples with longer pre-annealing exhibited a smaller rate of resistance change. The sample with 370 mins pre-annealing had less than 6 $\Omega.cm^2$ resistance increase. This showed that increasing the length of pre-annealing time leads to ΔR_S increase in the beginning, which is consistent with the annealing time used for mitigation of LeTID [194]. Further increase of the pre-annealing time causes less ΔR_S, which should be related to the hydrogen effusion in silicon solar cells in long-term thermal processing.

Figure 32.c shows ΔR_S of the sample pre-annealed with 2.5 V reverse bias with different pre-annealing time from 0 to 22 h at 400℃ before being bias-stressed and I-V characterised for 90 minutes under alternating 500 mA forward and 2.5 V reverse bias at 400 ℃. The highest ΔR_S occurred in the sample with 3 h pre-annealing, where ΔR_S was around 3.1 Ω.cm^2 after the 5th forward bias cycle. ΔR_S of the specimen pre-annealed 22 h was around 1.5 Ω.cm^2 after the 5th forward bias cycle. Figure 32.d shows the rate of the series change of the PERC specimens under the forward bias cycle of the specimens shown in Figure 32.c at 400 ℃. The annealing time includes the time for the pre-annealing procedure and the measurement cycle time. The rate of the series change is calculate based on the formula 3.24, where the ΔR_S represents the series change between the value before the forward cycle and the value of after the forward cycle and $t_{forward\ cycle}$ represent the forward bias annealing time (here is 10 mins).

$$\frac{\Delta R_S}{dt} = \frac{R_{S\ after\ the\ forward\ cycle} - R_{S\ before\ the\ forward\ cycle}}{t_{forward\ cycle}} \quad (3.24)$$

Pre-annealing PERC specimens between 2 and 3 h at 400 ℃ leads to the highest ΔR_s/dt rate around 0.27 Ω.cm^2/min at the 5th forward cycle, while 2.1763 Ω.cm^2/min for specimen pre-annealed 2 h and 2.2767 Ω.cm^2/min for specimen pre-annealed 3 h. The specimens pre-annealed in the region between 2 and 3 hours shows the highest change rate among the tested specimens. With increase of pre-annealing time, a subsequent decrease in the ΔR_s/dt rate is observed. The subsequent decrease after times longer than 3 h could be related to hydrogen concentration change during excessively long annealing periods. The change of R_S for specimens pre-annealed 22h is still bias controlled and ΔR_S/dt rate decreased to 0.11 Ω.cm^2/min at the 5th forward cycle. This indicates that the concentration of the mobile charge ions is decreased with the increase of annealing time. These results show a correlation between the pre-annealing conditions that lead to large rates of change and thermal treatments that have been reported for the mitigation of LeTID [194]. Based on the difficulty of finding a LeTID treatment that does not cause HICR [198, 199], it is likely that these two effects share a common cause or are at least some correlations.

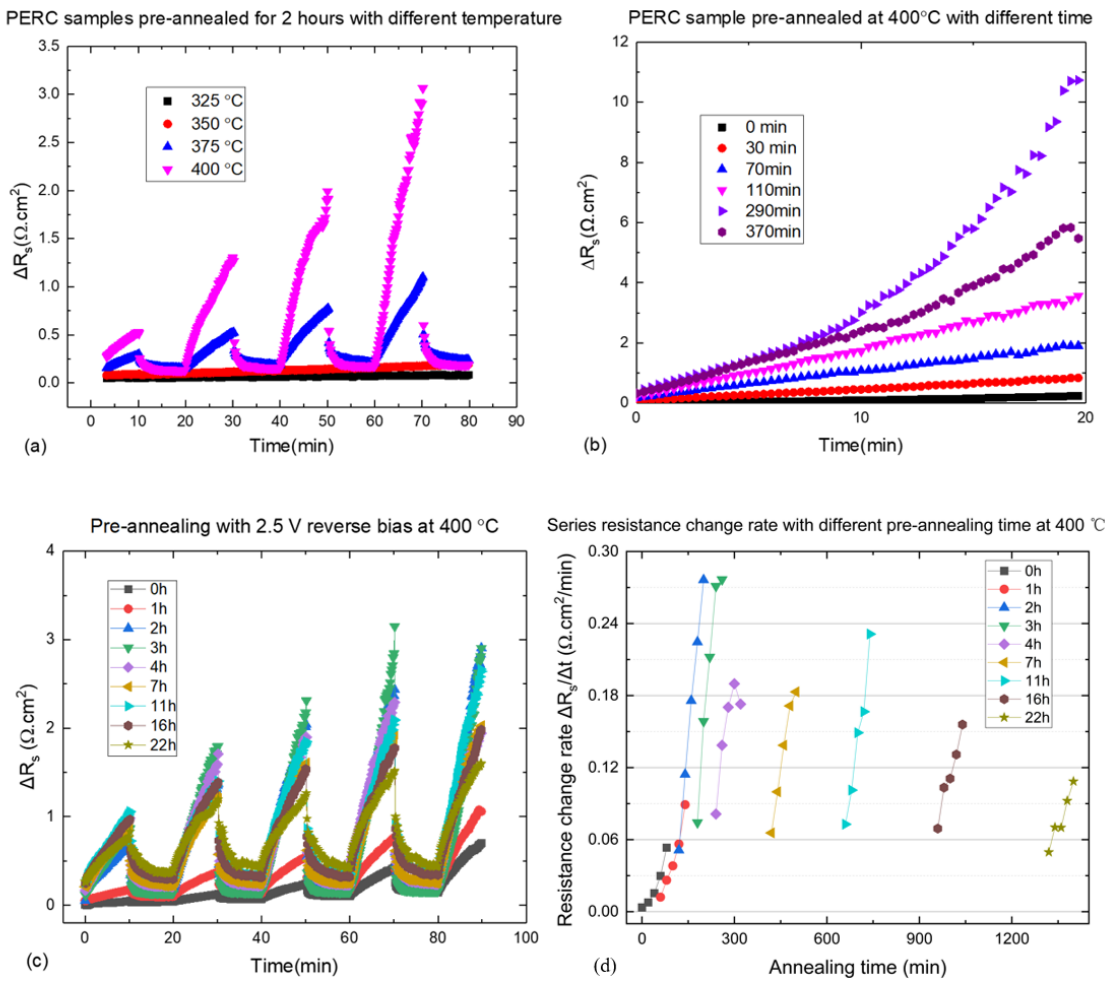

Figure 32.The effect of Pre-annealing conditions for the contact resistance change for PERC samples (a) ΔR_S of specimens at 400℃ after 2.5 V reverse bias annealing with different temperatures for 2 hours (b) ΔR_S of specimens under forward bias after 2.5 V reverse bias annealing with different time at 400℃. (c) ΔR_S of the sample under 500 mA forward and 2.5 V reverse bias cycle after 2.5 V reverse bias annealing with different pre-annealing times at 400℃. (d) the ΔR_S rate of the sample under 500 mA forward and 2.5 V reverse bias cycle after 2.5 V reverse bias annealing with different pre-annealing times at 400℃. Only one sample was used for each pre annealing condition.

4.9 Contact resistance in TOPCon vs PERC

In Section 4.4, it has been identified that the increase in R_S in PERC is related exclusively to increased contact resistance at the front contact (n+ emitter). To better understand the HICR phenomenon in TOPCon solar cells, transmission line method (TLM) measurements are used to isolate changes in the contact resistance for both cell architectures. The results are displayed in Figure 33, where the error bars correspond to the goodness of the linear fit. For PERC devices, the TLM measurements were performed on the front surface and are displayed in red in Figure 33. To better understand the changes in TOPCon cells, TLM measurements were performed on both the front and rear surface, this data is displayed in blue and yellow in Figure 33, respectively.

For PERC, a clear trend of increased contact resistance as a function of annealing temperature is observed. This result closely matches the observations in Figure 27 and Figure 28 as expected, and is in agreement with previous work in the literature [30]. It shows that the change in R_S is related to contact resistance on the front surface and that the temperature plays a large role.

In TOPCon cells, measurements on the front surface (referring to the p+ boron emitter) showed little variation. The change in contact resistance for each temperature are all almost within one standard deviation from the initial average value. However, measurements on the rear side (tunnel oxide / n+ doped polysilicon layer) display a significant increase. This change occurs on the surface consisting of the n+ doped layer contacted by screen-printed silver, which is the same type of contact as for the front surface in PERC. The slope in the TLM curve was not significantly altered, implying that the changes observed are dominated by contact resistance, rather than changes in the emitter sheet resistance. It is possible to conclude unambiguously that for PERC and TOPCon cells, the instability of contact resistance changes upon bias-stress annealing is due to the n-type silicon/Ag contact interface.

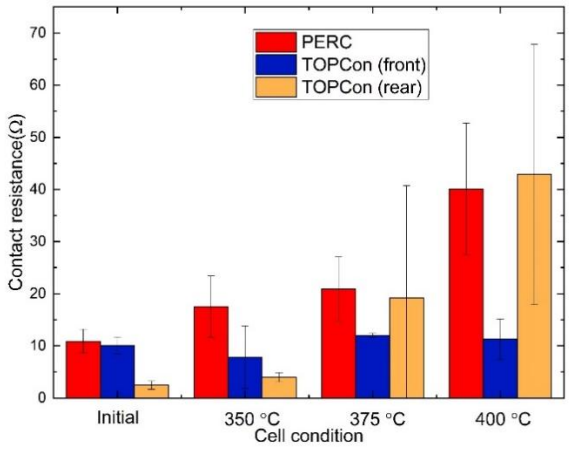

Figure 33. Contact resistance values extracted from TLM measurements for biased annealing at various temperatures. The measurements were taken on samples after the completion of the third cycle of 30 min forward current. This represents the point of maximum degradation in this experiment. The errors on the initial values represent the standard deviation of three samples. Only one sample was used for each annealing condition, the errors shown for annealed samples represent the 95% confidence interval of the linear TLM fit. All values shown are in ohms (Ω).

4.10 Discussion

This chapter has unequivocally demonstrated the impact of electric fields on the series resistance change in PERC and TOPCon architectures without light soaking at elevated temperatures. The increased R_S were observed in both architectures, following the application of a forward bias between the front and rear metal contacts at elevated temperatures. The application of a reverse bias was able to reverse this increased R_S to a certain extent. The temperature of the cell during exposure to electric fields and the stress of the bias significantly impacted the amount of R_S change for both architectures. Increasing the annealing temperature from 350 to 400 ℃ increases the R_S change from 0.1 to 30 Ω.cm^2 for PERC and 2 to 20 Ω.cm^2 for TOPCon architectures, as shown in Figure 28. Increasing the amount of forward bias from 10 to 500 mA current increases the R_S change from 2 to 10 Ω.cm^2 for PERC and 10 to 20 Ω.cm^2 for TOPCon architectures, as shown in Figure 29. Through the modification of the PERC geometry and IV measurement, the different current pathways are isolated, and it is confirmed that the increased R_S occurs at the front surface near the junction between the Ag contact and the n-type silicon region. Through the TLM measurement, it confirmed that the increased R_S occurs on the rear surface between the Ag contact and the heavily doped n+ poly-Si layer.

The R_S change of PERC and TOPCon during the bias-annealing treatment shows some similarities:

1. Electric fields between the cell front and rear contacts can modulate the R_S change
2. The direction of the field impacts this modulation.
3. An increase in the temperature or magnitude of the bias leads to a more pronounced increase in R_S
4. This change occurs at the Ag/n-type Si interface.

However, there are still some differences between the R_S response of PERC and TOPCon structures to the bias-annealing process:

1. TOPCon structures show a more significant “irreversible” component during the annealing process, which is identified as a higher value of the R_S change at the end of the 3rd reverse bias cycle, as shown in Figure 28.b and Figure 29.b.
2. TOPCon structures exhibit a different temperature response. TOPCon specimens still exhibit a substantial increase in R_S change at 350 ℃, as shown in Figure 28. However, when the sample is cooled down at RT and TLM measurement is taken, this increase is no longer observed, as shown in Figure 33.

3. TOPCon structures show a different response to the low bias current. A clear reversible R_S change is observed in the PERC structure with 10 mA forward current and 2.5 V reverse bias cycle, while almost no impact on the observed R_S change in the TOPCon structure, as shown in Figure 29.

Numerous studies indicate that H plays an important role in the LeTID of PERC cells, while the defect concentration increases with the increase of hydrogen content [112, 191, 200]. However, the kinetics of hydrogen behind it is still not clear. It has been reported that the PERC specimens after LeTID mitigation thermal treatment process are stable during the further prolonged light soaking test [163, 190]. It is hypothesised that prolonged annealing causes the effusion of the hydrogen atoms from the cells and the reduction of the remaining hydrogen concentration inside the cells leads to the recovery of the cells. For the PERC specimen pre-annealed with 2.5 V reverse bias at 400 °C for up to 22 h, it still shows the increase of R_S with forward bias and a decrease of R_S with reverse bias, shown in Figure 32.c. The bias-controlled resistance changes after prolonged annealing indicate that there is still enough hydrogen inside the cells after long-term annealing, which is in clear contradiction with the hypothesis that the majority of hydrogen atoms effused from the cells. The LeTID mitigation treatment in literature [98, 101] therefore does not require the removal of all H from the cells, but rather that it is transformed to more stable forms than the mobile monoatomic species, whether in the bulk or near-surface regions.

I explained the dependence of the series change of the PERC cells on the applied bias through the effect that the migration of the hydrogen near the Ag/n-Si interface. When the metal is intimately connected to the semiconductor, the Schottky barrier is formed at the interface with the existence of a high concentration of interface states [201]. The biasing operations allow hydrogen species to accumulate in the different regions of the cells, leading to the change of the passivation at the Ag/Si interface. The movement of hydrogen in silicon occurs largely via interstitial sites and thus the charge state plays a large role in the motion of hydrogen [197]. Hydrogen atoms in silicon exist in three charge states, negative (H^-), neutral (H^0) and positive (H^+). It is widely accepted that the position of the Fermi energy (E_F) influences the fractional concentration of the three possible charge states, such that H^+ is typically dominant in p-type silicon and H^- is typically dominant in n-type silicon [149, 197, 202]. The impact of the different bias conditions on the energy band diagram is shown in Figure 34. Figure 34.a describes the p-n junction in a PERC solar cell, contacted by an Ag contact, under reverse bias conditions. Under reverse bias, the electric field across the junction is increased, which greatly reduces the migration of H^+ from the bulk into the n-type emitter. A large number of the interface states are unoccupied at

the Ag/n-type Si interface, leading to the small Schottky barrier height with low contact resistance. Conversely, under forward bias, the electric field across the junction is reduced and the H^+ has the possibility to cross the p-n junction and be converted to H^-, which increases the concentration of H in the emitter, as schematically shown in Figure 34.b. Then, the mobile hydrogen interacts with the unoccupied interface states, leading to the increase of the Schottky barrier height, as shown in Figure 34.c. Due to the increase of Schottky barrier height, fewer electrons can tunnel through the barrier, which corresponds with the increase of the contact resistance.

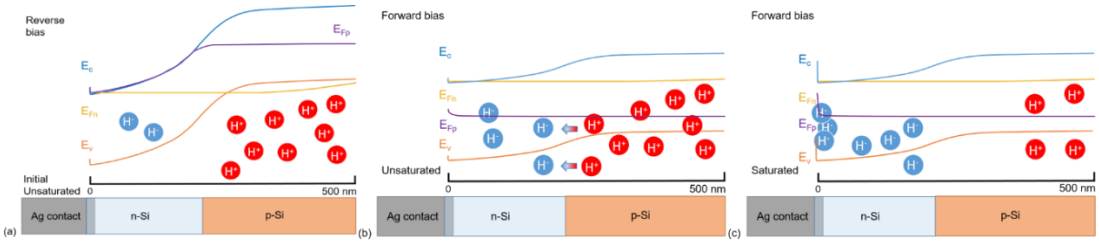

Figure 34. Schematic of band diagram of the PERC specimens under different bias conditions. (a) under reverse bias (b) diffusion of the hydrogen atoms from p-type silicon to n-type silicon under forward bias (c) occupation of interface states under forward bias.

To explain the impact of the measurement frequency on the change in series resistance of solar cells in Section 4.7, the electric field at the Ag/Si contact itself should be considered. The Schottky barrier also acts as an obstacle for H^- ions to occupy these interface states. When the applied forward bias from SMU 2 is removed and the measurement bias from SMU 1 is applied, as detailed in Section 3.3, the Schottky barrier height is reduced by a small amount. H^- ions have more possibility to diffuse to the Ag/Si interface and deactivate the interface states, which leads to a reduction in the Fermi level pinning and an increase in the Schottky barrier height. When the measurement frequency is increased, the frequency for the reduction of the obstacle for H^- ions is increased, hence causing the increase of resistance change rate. Once the interface is passivated with enough hydrogen atoms, the Schottky barrier is oversaturated and can be broken down by the localised large electric field generated by the applied bias, which causes the sudden reduction in the series resistance of the cells during bias annealing. That is the reason why the R_S change should be kept in the range $<20\ \Omega.cm^2$ during the bias annealing process.

In the case of a TOPCon structure, the R_S change during the bias annealing process is more complicated. Firstly, the R_S change is observed at the rear contact of the TOPCon specimen, while the R_S change occurs at the front contact of the PERC specimen. Secondly, the kinetics of hydrogen is more complicated in the polysilicon layer. The polysilicon layer directly under the rear metal acts as a sink for the mobile hydrogen, due to the existence of a high concentration of the defects and grain boundaries in this layer [52, 203]. For

these reasons, it is expected that the kinetics and dependence on applied bias might be varied between PERC and TOPCon structures. However, TOPCon structures still have a strong response to applied bias. When a forward bias is applied across the p-n junction in TOPCon specimens, the hydrogen atoms stored in the p^+ emitter will drift across the junction into the n-type bulk part. Through the increased gradient of H concentration in the bulk part, further H diffusion across the Si/tunnel oxide/n+ poly-Si is achieved. Another finding is that applied bias has an impact on the resistance change of the metal contact interface itself. When the interface is not saturated with sufficient hydrogen atoms, the contact resistance is low and this impact is highly small. When enough interface states are occupied with the hydrogen atoms during bias annealing treatment, the contact resistance increases significantly and applied bias will appear as a voltage drop across the contacts. In the case of PERC architectures, this impact is highly small, given the capacity to almost completely suppress HICR with reverse bias annealing treatment [204]. In the case of TOPCon architectures, this impact may be more prominent, due to the high concentration of H present in the poly-Si and tunnel oxide layers. This correlates with the comparatively small R_S change or TOPCon structures during the first forward/reverse bias cycle, as shown in Figure 28.b, Figure 29.b and Figure 31.b. Identifying the sereies resistance change in PERC and TOPCon cells and confirming the response regions still have a profound effect on further studies exploring degradation mitigation pathways and developing manufacturing process strategies in these two architectures .

4.11 Summary

In this chapter, the impact of the electric field on the nature of the instability of the series change in both PERC and TOPCon solar cells is investigated, especially associated with hydrogen dynamics at the interface. Through the modification of the commercial PERC cell with the isolated current pathways, it is identified that increased R_S under forward bias almost exclusively occurs at the interface between the Ag contact and the n+ emitter for the PERC architecture. For the first time, I show that hydrogen induced contact resistance (HICR) also occurs in the TOPCon architecture. The temperature of the cell during the bias annealing process and the polarity and magnitude of the electric field impacted the extent of HICR for both PERC and TOPCon solar cells. It is identified that the root cause of the increased R_S in TOPCon is the contact resistance change between the Ag contact and the heavily doped n+ poly Si layer through the TLM measurement. Furthermore, given the results that HICR in PERC and TOPCon architectures occurs at Ag/n-Si interface, it is proposed that the cause

of the instability of the series resistance change is the migration of mobile hydrogen near this interface. The migration of the hydrogen atom is controlled by its charge state and electric field across it. However, the exact mechanisms of this hydrogen accumulation in TOPCon structures require further exploration. The application of the electric field can provide insight into the role of hydrogen in the series resistance change of the commercial PERC and TOPCon cells and the development of processing strategies to mitigate degradation and enhance stability in these architectures.

Chapter 5 Controlling and tailoring H injection across a dielectric-silicon interface

5.1 Overview

This chapter investigates the impact that a surface electric field has on the nature of surface-related degradation in TOPCon solar cells. The surface polarisation of TOPCon lifetime samples was achieved by the application of corona charge while the samples underwent light soaking at elevated temperatures. It is observed that the application of a positive charge on the surface drastically enhances the amount of surface-related degradation. Increasing the surface charge leads to more degradation in the minority carrier lifetime and a pronounced increase in J_0. In contrast, the application of the negative charge on the surface does not impact the amount of degradation. It is proposed that the cause of degradation is the accumulation of excessive hydrogen near the c-Si / SiO_x interface and that the application of surface charge accelerates the movement of hydrogen to the interface.

5.2 Introduction

Chapter 2 explored the degradation dynamics in TOPCon specimens. The high efficiency of TOPCon cells is achieved through good passivating contact schemes based on a thin tunnelling oxide / doped polysilicon layer stack. Firing-induced degradation has been observed in such n+ poly-Si / tunnel SiO_X layers at the rear of TOPCon cells [79, 81, 82, 205]. A range of reports have provided evidence of hydrogen involvement for these instabilities during light soaking, including varying the firing conditions, type of hydrogen-containing dielectric, and removal of SiN_X layer [33, 34, 127, 128]. This lifetime degradation correlated with an increase of J_0 and was triggered by an industrial-type firing step [32, 33]. This indicates that the firing-induced degradation is caused by the deterioration of the surface passivation layers. It has been reported that the increase in J_0 during degradation correlates with an increase in hydrogen concentration, implying the formation of hydrogen-induced defects near the c-Si surface, at the Si/SiO_X interface [34]. To date, however, little is understood about root causes for this firing-induced surface-related degradation (SRD), such that suitable mitigation approaches can be developed.

One possible approach to modify the diffusion of H in tunnel oxide structure is the application of electric fields to control the movement of charged hydrogen ions during various degradation conditions. This approach originates from the work of Hamer *et al.*, who observed increased contact resistance in PERC cells following a post-firing thermal treatment [30]. It showed that the application of an electric field during degradation could accelerate or suppress the increased contact resistance, depending on the direction of the field. In Chapter 4, the instabilities of contact resistance change were also observed in TOPCon solar cells, implying that electric fields can modulate degradation. It has also been reported that surface electric fields have an impact on the resulting surface passivation after the firing of hydrogen-containing dielectrics [134]. These works show that the application of surface electric field could open new ways to control H migration and potentially mitigate SRD.

In this chapter, I explore the impact that surface polarisation, induced by corona charging, has on the firing-induced SRD of thin oxide / n+ doped poly-Si passivating schemes. The presence of an electric field at the surface through the corona charge during light soaking can accelerate the deterioration seen in surface passivation of samples. This provides further evidence that this SRD is likely caused by the movement of charged particles near the interface, most likely hydrogen ions.

5.3 Experimental Procedure

Experiments in this work were carried out on the full-size TOPCon lifetime architectures from group D to group I, as described in Section 3.1. The effective lifetime τ_{eff} is measured as a function of the excess carrier density Δn at ~ 25 °C using the WCT-120 Photoconductance lifetime tester. The τ_{eff} of the TOPCon sample is extracted at a fixed excess carrier concentration of $\Delta n = 1\times10^{15}$ cm^{-3}. The recombination current density J_0 is extracted at a fixed excess carrier concentration of $\Delta n = 1\times10^{16}$ cm^{-3} using the Kane and Swanson method [206]. Corona discharge is used to create a surface electric field without needing a metal contact, as detailed in Section 3.2.2. The corona charging was performed continuously throughout the experiments, due to the vanish of the corona charge voltage at the surface caused by the thermionic emission at elevated temperature [169, 207]. Figure 35 shows the measurement set-up and test conditions for TOPCon lifetime specimens. A closed loop controlled hot plate is used to heat the sample on the Al stage at a temperature of 175 °C. Two different light sources were used during the light soaking in these experiments, depending on the compatibility

with the corona charge box. Figure 35.a shows the measurement set up for specimens under 1.1 Suns light soaking without corona charge at 175 ℃. Samples were illuminated by halogen lamps (with a wavelength range of 320-1100 nm) with an equivalent illumination intensity of 1.1 Suns as measured by a calibrated silicon solar cell. Figure 35.b shows the measurement set up for samples tested in the dark corona charging box, without illumination, at 175 ℃. Figure 35.c shows the measurement set up for specimens under 0.1 sunlight soaking with corona charge at 175 ℃. The specimens tested in the corona charging box were illuminated with normal commercial LED lamps (with a wavelength range of 275-950 nm) reaching an illumination intensity of 0.1 sun as measured by a calibrated silicon solar cell, due to physical constraints on the experimental design. Single junction solar cells can absorb the light in the wavelength range between 300 and 1100nm [207] and these two types of lamp can supply the light with the wavelength in that range. Figure 35.d shows the schematic of the structure of nnnTOPCon lifetime specimens used in this chapter. The structure of the other specific types of TOPCon specimens used will be put in the related section.

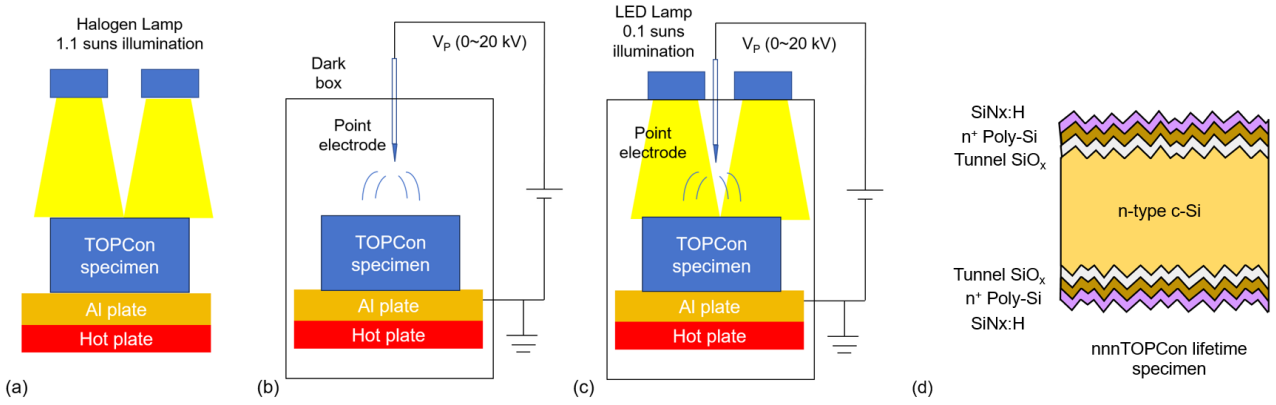

Figure 35. Schematic of measurement set up and test conditions for TOPCon lifetime specimens. (a) 1.1 suns illumination without surface polarisation at 175 ℃. (b) surface polarisation without light illumination at 175 ℃. (c) surface polarisation with 0.1 sun light illumination at 175 ℃. (d) schematic of structure of nnnTOPCon lifetime specimen.

This experimental setup aimed to evaluate the effects that light illumination and surface polarisation have on TOPCon lifetime structures. It is noted that the corona charge, and thus the modified surface electric field, was only applied to the front surface. The effective lifetime τ_{eff} and recombination current density J_0 were evaluated before and after each step of corona charge annealing. With control of light illumination, surface polarisation generated by corona discharge, and annealing time, the impact of the surface polarisation of the change for τ_{eff} and J_0 on TOPCon lifetime specimens is investigated.

5.4 Degradation and Recovery of TOPCon lifetime samples under light illumination

Previous reports have shown that the degradation and recovery of symmetrical thin oxide / n+ doped poly-Si lifetime structures are observed under 175 °C, 1 sun illumination conditions [128]. To verify such degradation behaviour, TOPCon lifetime specimens with n-type substrate combined with thin oxide / n+ doped poly-Si / SiN_X layer on both sides (nnnTOPCon) from Trina were subjected to 1.1 suns light soaking on a hot plate at 175 °C without corona charging, as shown in Figure 35.a. Figure 36 shows the change of τ_{eff} and J_0 of nnnTOPCon under 1.1 suns illumination at 175 °C. The effective lifetime of nnnTOPCon undergoes severe degradation from the initial value of ~ 6.8 ms, reaching a minimum value of ~ 2.7 ms after 7.6 h light soaking. The reduction of the τ_{eff} is correlated with an increase of the J_0 from 12.7 to 42.6 fA/cm^2. The time for nnnTOPCon to reach the maximum degradation point at 175 °C correlates well with the time reported in Ref [128] of around 8 h. With a further 1.1 sun annealing treatment, the subsequent recovery of τ_{eff} and reduction on J_0 were seen, almost back to initial values, after 400 hours of treatment, indicating that this degradation is attributed to the deterioration in surface passivation. This degradation and recovery cycle in nnnTOPCon specimens under 1.1 suns 175 °C annealing closely resembles those presented by Di *et al.* [33] and Chen *et al.*[128]. This demonstrates that the samples investigated in this study are susceptible to the previously identified SRD phenomenon.

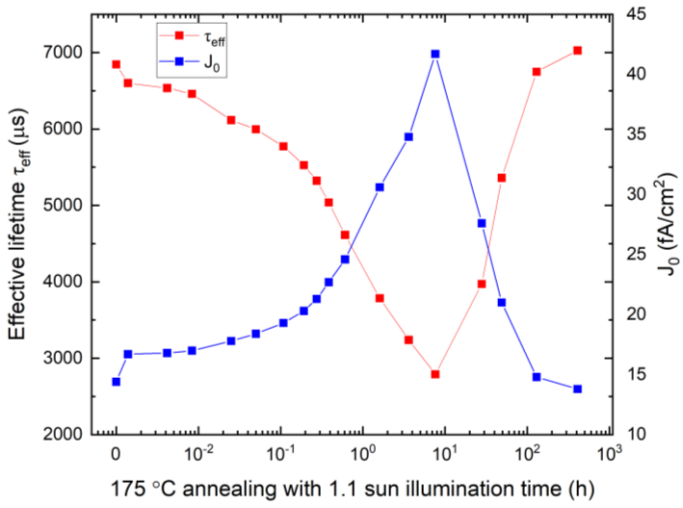

Figure 36. The change of effective lifetime τ_{eff} and recombination current density J_0 of TOPCon lifetime specimens with n-type substrate combined with thin oxide / n+ doped poly-Si / SiN_X layer on both sides under light soaking under 1.1 suns light soaking at 175 °C. Only one sample was used for this test.

5.5 Surface Polarisation without light illumination

To isolate the impact of the surface polarisation and the light illumination, nnnTOPCon specimens from Trina were tested only in the presence of the corona charge without illumination at first, as shown in Figure 35.b. Figure 37 displays τ_{eff} and J_0 change of the nnnTOPCon specimens under 4 different test conditions: (i) Control sample: Kept in dark box, (ii) Anneal only sample: Annealed at 175 ℃, (iii) Positive Corona: Annealed at 175℃ with positive corona (1μA), and (iv) Negative Corona: Annealed at 175℃ with negative corona (1μA). The data in black triangles was a measurement control, which was kept in a dark box at room temperature without annealing or corona charging. This control sample was almost unchanged during the experiment, indicating the good stability of specimens at room temperature without illumination, as shown in Figure 37.a and Figure 37.b. The sample that underwent dark annealing but was not subjected to corona charging exhibited slight degradation. The lifetime was reduced by 0.5 ms, as shown in red squares in Figure 37.a. The J_0 decreased from 20.7 to 19.7 fA/cm^2 after 12 h treatment, as shown in red squares in Figure 37.b. This indicates that the 175 ℃ annealing does not cause the deterioration of the surface passivation. However, the lifetime change ~ 0.5 ms for the specimen during dark annealing at 175 ℃ (red squares in Figure 37.a) was much less pronounced than the lifetime change ~ 4.1 ms for the specimen under 1.1 suns 175 ℃ annealing shown in Figure 36.

The application of a negative corona charge on the surface (gold triangles) led to little change in lifetime during the dark annealing. During the 12 hours of testing, the lifetime was reduced by ~ 300 μs, which was slightly less than for the sample without corona charge, as shown in Figure 37.a. The J_0 decreased from 17.9 to 17 fA/cm^2 after 12 h treatment, as shown in the gold triangles in Figure 37.b. In sharp contrast, the application of a positive corona charge to the surface during annealing (blue circles) led to significant degradation. The lifetime was reduced by > 2 ms, from 8.4 ms to 6.2 ms after 12 h treatment, as shown in Figure 37.a. This reduction correlated with an increase in J_0 from 14.9 to 16.5 fA/cm^2, which was not observed for other samples, as shown in Figure 37.b. This indicates that surface polarisation impacts surface-related degradation, even under dark conditions where the degradation is less pronounced. Hereafter, this effect is referred to as electric field-induced degradation (EFID).

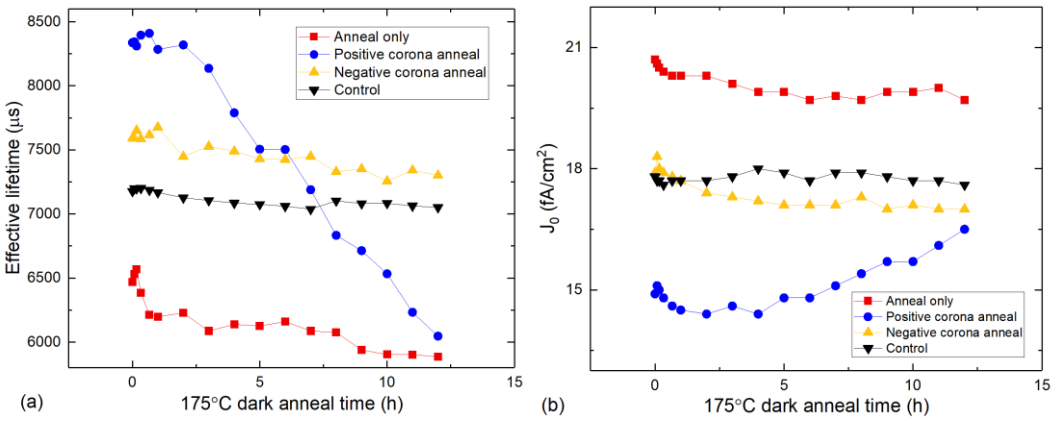

Figure 37. (a) τ_{eff} and (b) J_0 for nnnTOPCon samples exposed to various corona charge conditions during dark annealing at 175 °C. (i) Control (black triangle): Kept in dark box, (ii) Anneal only (red squares): Annealed at 175 °C, (iii) Positive Corona (blue circles): Annealed at 175°C with positive corona (1µA), and (iv) Negative Corona (gold triangles): Annealed at 175°C with negative corona (1µA). Only one sample was used for each dark bias annealing condition.

Due to the severe degradation observed with positive charge annealing treatment, EFID is further investigated by applying the positive corona charge on a new set of nnnTOPCon samples. Figure 38 displays the τ_{eff} and J_0 changes of the nnnTOPCon samples under three different positive corona charge conditions:

(i) Control (orange squares): Kept in dark box at RT (room temperature),

(ii) Positive corona at RT (red squares): positive corona (1µA) at RT, and

(iii) Positive Corona at 175°C (blue squares): positive corona (1µA) at 175°C.

The application of positive corona charge to the surface at 175 °C (blue squares) led to significant degradation of the lifetime around 2.2 ms after 12 h treatment, while the application of positive corona charge to the surface at room temperature led to loss of effective lifetime around 0.4 ms, as shown in Figure 38.a. The specimen with positive corona charge at elevated temperature shows an increase of J_0 around 1.6 fA/cm^2, as shown in the blue squares in Figure 38.b. The J_0 of specimen with positive corona charge at room temperature was stabilised around 20.4 fA/cm^2 for the first 10 h, but increased to 21.5 fA/cm^2 after a further 2 h treatment, as seen in the red squares in Figure 38.b. This provides a clear indication that surface polarisation has an impact on the SRD and that the application of positive charge can accelerate the process at elevated temperatures.

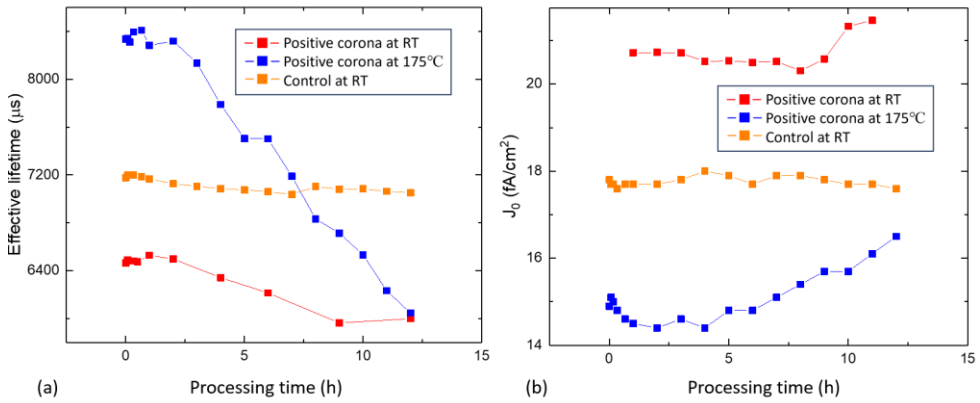

Figure 38. (a) τ_{eff} and (b) J_0 for nnnTOPCon samples exposed to various conditions. (i) Control (orange squares): Kept in dark box at RT (room temperature), (ii) Positive corona at RT (red squares): positive corona (1μA) at RT, and (iii) Positive Corona at 175℃ (blue squares): positive corona (1μA) at 175℃. Only one sample was used for each bias annealing condition.

5.6 Surface Polarisation with light illumination

Next, the nnnTOPCon samples from Trina were tested under illuminated, heated, and corona-exposed conditions, as shown in Figure 35.c. In the last section, the nnnTOPCon specimen under 1μA negative corona annealing at 175 ℃ showed the similar trend for the lifetime change of nnnTOPCon specimen under annealing only condition. 1μA negative corona might not be enough this degradation, therefore I increase the negative corona current from 1 to 4 μA. To achieve a direct comparison between the impact of positive corona and negative corona during the illumination annealing test, the positive corona current is increased from 1 to 4 μA. Since illumination was reduced to 0.1 suns, it is expected that the rate of degradation could also be modified. It is noted that the maximum degradation with around 60 % lifetime loss will be achieved after around 8 h 1.1 suns 175 ℃ annealing treatment, as shown in Figure 36. Figure 39 shows the τ_{eff} and J_0 of nnnTOPCon specimens under three corona charge conditions under 0.1 sun illumination at 175 °C:

(i) Negative corona (orange triangles) of 4μA current at 175℃,

(ii) Anneal only (red squares): annealed at 175 °C, and

(iii) Positive Corona of 4μA current at 175℃ (blue squares).

For the specimen annealed only at 175℃ with 0.1 sun illumination, the characteristic lifetime degradation of around 4.7 ms after 24 h treatment was observed, as shown in red squares in Figure 39.a. This corresponds with an increase of J_0 around 18.1 fA/cm^2, as shown in red squares in Figure 39.b. Comparing Figure 36 and

Figure 39, it is noted that a reduction in illumination intensity causes a reduction in the degradation rate. Under 1.1 sun, a maximum degradation is observed after 7.5 hours, while the sample under 0.1 sun is still degrading after 24 hours. Moving to the impact of corona charge, the application of negative corona charge with a magnitude of 4 µA yields a very similar response to that observed on the annealing-only sample shown in Figure 39. A similar increase in J_0 is seen for this case, as shown in Figure 39.b. Specimens with 4 µA negative corona charge degrade from 5.2 ms to 2.9 ms after 24 h treatment, while specimens annealed only at 175 °C degrade from 8.2 ms to 3.5 ms after 24 hours treatment, as shown in Figure 39.a. The presence of a positive corona charge (blue circles) significantly impacts the degradation behaviour. In this case, the lifetime was reduced from 6.9 ms to 0.7 ms after the 24-hour testing period. Figure 39.b shows that a corresponding increase in J_0 is observed, and it is much more pronounced with an increase of 37 fA/cm^2. This shows that the positive charge on the surface has a profound impact on the deterioration of surface passivation.

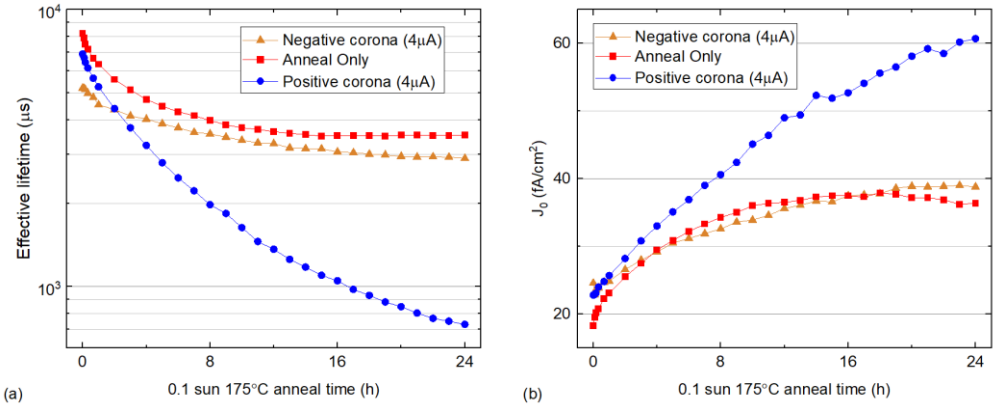

Figure 39. (a) τ_{eff} and (b) J_0 for samples exposed to various corona charge conditions during light soaking under 0.1 suns at 175 °C. (i) Negative corona (orange triangles): negative corona (4µA) at 175°C, (ii) Anneal only (red squares): annealed at 175 °C, and (iii) Positive Corona at 175°C (blue squares): positive corona (4µA) at 175°C. Only one sample was used for each bias annealing condition.

5.7 Influence of the magnitude of surface polarisation under light illumination

In the previous section, I demonstrated that positive charge on the surface impacted the deterioration of surface passivation under 0.1 sun illumination at 175 °C. In this section, I vary the magnitude of the applied corona charge to study the impact of the strength of the surface polarisation on the τ_{eff} and J_0 change of nnnTOPCon specimens from Trina. Figure 40 shows the impact of the varied magnitude of positive corona charge on the τ_{eff} and J_0 of the TOPCon_E specimens under 0.1 sun illumination at 175 °C.

The application of 1 µA induces a degradation in lifetime from 6.4 ms to 1.9 ms, as shown in Figure 40.a. An increase in J_0 from 19.8 to 41.3 fA/cm^2 is observed in Figure 40.b. Increasing the corona magnitude to 4 µA significantly increases the rate and extent of degradation for the period tested, with the lifetime reducing to 0.7 ms and J_0 increasing to 58.7 fA/cm^2. Further increasing the corona discharge to 12 µA causes the lifetime to degrade by an additional order of magnitude to < 100 µs. For this case, the J_0 increases rapidly to 540 fA/cm^2, indicating a severe deterioration in surface passivation. Increasing the magnitude of the positive charge on the surface impacts the amount of EFID. This clearly shows that the surface passivation can be modulated by the presence of a surface electric field, further supporting the hypothesis that the changes are caused by the movement of charged particles.

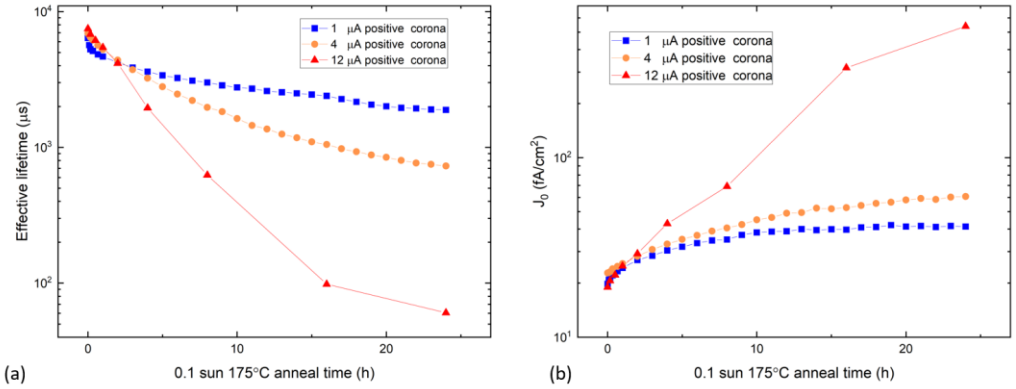

Figure 40. (a) τeff and (b) J0 for samples exposed to positive corona charge at 1 µA, 4 µA and 12 µA during light soaking under 0.1 suns at 175 °C. Only one sample was used for each bias annealing condition.

Figure 41 shows the impact of varying magnitude of negative corona charge on the τ_{eff} and J_0 of the nnnTOPCon specimens under 0.1 sun illumination at 175 °C. The changes of the magnitude of charge between 1 µA ,4 µA and 12 µA show similar impact on the specimens after 24 h treatment. The effective lifetime of all specimens decreased to below 2.5 ms, with the increase of J_0 to ~ 40 fA/cm^2. Compared to the specimens with positive corona shown in Figure 40, negative corona shows less impact on the deterioration in surface passivation and no dependence on the field strength.

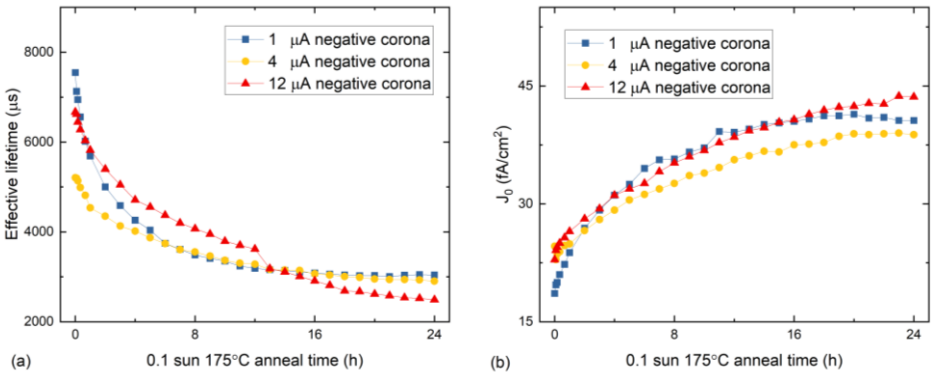

Figure 41. (a) τ_{eff} and (b) J_0 for nnnTOPCon samples exposed to negative corona charge at 1 µA, 4 µA and 12 µA during light soaking under 0.1 suns at 175 °C. Only one sample was used for each annealing condition.

5.8 EFID on TOPCon precursors

All the results shown thus far have been on symmetrical thin SiN_X / n+ poly / tunnel oxide samples, which represent the rear surface of the standard commercial TOPCon cell. To study this phenomenon in a system more representative of a finished cell, the experiments are repeated on the TOPCon cell precursor with a boron emitter on the front surface, labelled as TOPCon precursor in Section 3.1. To keep the conditions consistent with previous results, the corona charge and light illumination were still applied to the thin oxide / n+ poly side. Figure 42 displays τ_{eff} and J_0 for TOPCon precursor exposed to various test conditions:

(i) Control (black triangle): Kept in dark box,

(ii) Anneal only (red squares): Annealed at 175 ℃,

(iii) Positive Corona (blue circles): Annealed at 175 ℃ with positive corona (1µA),

(iv) Negative Corona (gold triangles): Annealed at 175 ℃ with negative corona (1µA).

The initial lifetime of these samples is much lower than that of the symmetrical structures due to the contribution of the boron emitter. The data in black triangles was a measurement control, which was not subjected to illumination, annealing or corona charging. This sample was unchanged during the experiment, indicating good stability at room temperature without illumination. The sample that underwent dark annealing without corona charging (red squares) exhibited an increase in effective lifetime of 0.24 ms during the first 15 mins of light soaking. However, a slight degradation was observed, and the lifetime of the dark annealed sample had nearly returned to its initial value after 24 h treatment, as the red squares indicate in Figure 42.a. The J_0 increased from 28.9 to 49.1 fA/cm^2 after 24 h treatment, as seen in Figure 42.b.

The application of a negative corona charge on the thin oxide / n+ tunnel oxide surface (gold triangles) shows a similar pattern in τ_{eff} during the 0.1 sun annealing with an increase of 0.3 ms in the first 15 mins treatment, compared to the anneal-only specimens. After 24 hours of testing, the lifetime was reduced by ~ 220 µs, which was still larger than its initial value. The J_0 is stabilised around 54.9 fA/cm^2 during the 24 h treatment. In sharp contrast, the application of positive corona charge to the thin oxide / n+ tunnel oxide surface during annealing (blue circles) led to significant degradation. The lifetime was reduced to 37.7 µs after 24 h treatment. This reduction correlated with an increase in J_0 from 26.3 to 218 fA/cm^2, which was not observed for other samples, as shown in Figure 42.b. This indicates that positive corona charge on the thin oxide / n+ polysilicon surface of a TOPCon solar cell also induces severe EFID under 0.1 sun at 175 °C.

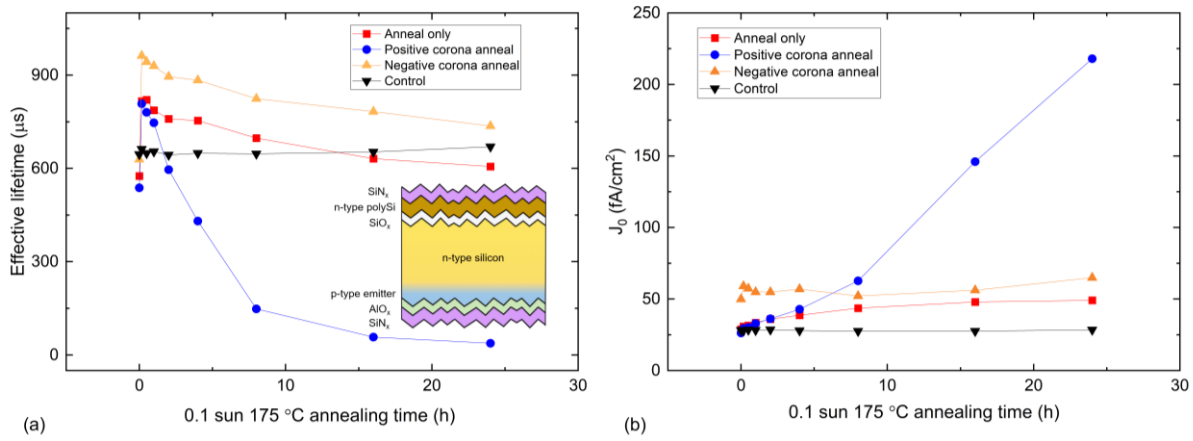

Figure 42. (a) τ_{eff} and (b) J_0 for TOPCon cell precursor samples exposed to various corona charge conditions during light soaking under 0.1 suns at 175 °C. (i) Control (black triangle): Kept in dark box, (ii) Anneal only (red squares): Annealed at 175 °C, (iii) Positive Corona (blue circles): Annealed at 175 °C with positive corona (1 µA), and (iv) Negative Corona (gold triangles): Annealed at 175 °C with negative corona (1 µA). The inset presented in (a) is a schematic of the sample structure. Only one sample was used for each bias annealing condition.

5.9 EFID for P-poly and P-substrate TOPCon samples

To investigate the impact of the doped polysilicon layer on the EFID behaviour of TOPCon samples, the experiments were repeated on the TOPCon lifetime samples with different types of doped polysilicon and substrates. The schematic of the test sample structures is shown in Figure 43. The nnnTOPCon lifetime specimens and npnTOPCon lifetime specimens from Fraunhofer is used in this test. The pnpTOPCon lifetime specimens and pppTOPCon lifetime specimens from ANU is used in this test. The details of these four types of the TOPCon lifetime specimens have been discussed in Section 3.1.

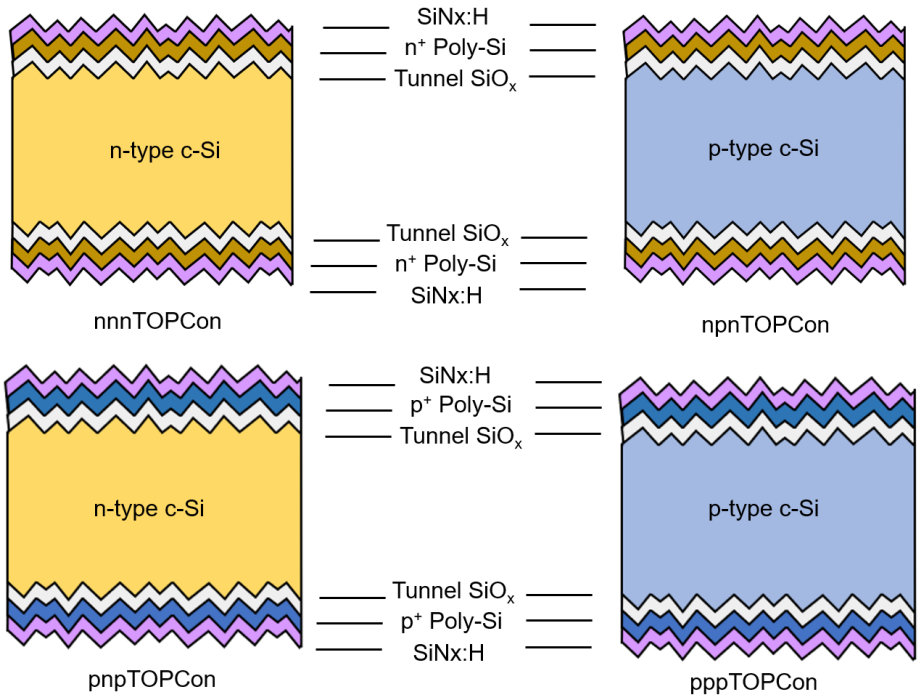

Figure 43. Schematic of the symmetrical TOPCon lifetime samples with different doped polysilicon layers and different substrates.

Figure 44 shows the τ_{eff} and J_0 change of the symmetrical thin SiN_X / n+ poly (or p+ poly) / tunnel oxide TOPCon lifetime samples with n-type (or p-type) substrate under 4 μA positive corona charge annealing at 175 °C with 0.1 sun illumination. For the samples with the n-type doped polysilicon layer, degradation was observed both in the n-type and p-type substrates shown in Figure 44.a, which corresponds well with the previous result in Figure 40.a. As shown in Figure 44.b, the J_0 of the n-type substrate with n+ poly layer increased from 11 fA/cm^2 to 50 fA/cm^2 after 12 h positive corona charge annealing, while the J_0 of the p-type substrate with n+ poly layer increased from 13 fA/cm^2 to 30 fA/cm^2, indicating the deterioration in surface passivation is more significant in n-type doped polysilicon TOPCon lifetime specimens with the application of the positive corona charge and 0.1 sun illumination on one side.

The samples with p-type doped polysilicon layers, however, showed different results as shown in Figure 44.c and Figure 44.d. P-type substrates with p+ poly are stable during corona charging, which is not influenced by the EFID. For the n-type substrate with p+ poly sample, the effective lifetime decreased from 1.2 ms to 0.8 ms after 24 h treatment shown in Figure 44.c. The J_0 for the specimens with p-type doped polysilicon is almost stable during EFID treatment. This shows that polysilicon doping has an impact on the deterioration of surface passivation.

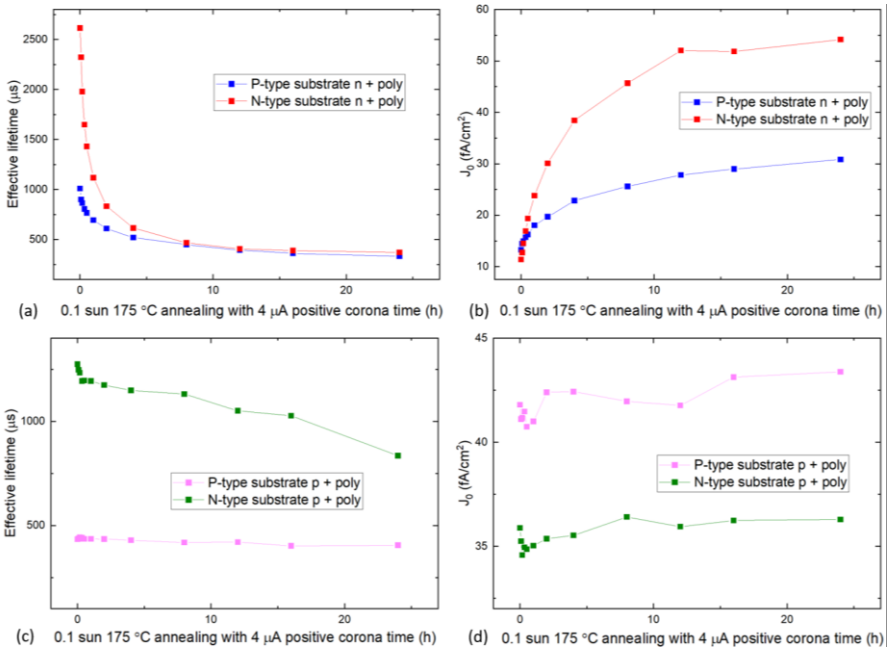

Figure 44. (a) τ_{eff} and (b) J_0 for symmetrical thin SiN_X / n+ poly / tunnel oxide TOPCon lifetime samples with n-type and p-type substrate exposed to 4 µA positive corona charge during light soaking under 0.1 sun at 175 °C. (c) τ_{eff} and (d) J_0 for symmetrical thin SiNx / p+ poly / tunnel oxide TOPCon lifetime samples with n-type and p-type substrate exposed to 4 µA positive corona charge during light soaking under 0.1 suns at 175 °C. Only one sample was used for each illumination recovery test.

5.10 Exploring the regeneration behaviour in EFID

The SRD in thin oxide / n+ doped poly-Si samples displayed in Figure 36 displays clear degradation and recovery behaviour and agreement with previous reports [33, 128]. When seeking solutions to mitigate this degradation mode, it is important to study the underlying mechanisms. Chen *et al.* showed that once the degradation and recovery cycle (annealing the specimen in the range of 250 – 400 ℃ with varied degrees of illumination from 1 to 150kW/m^2) was completed, no further degradation was observed following subsequent light soaking experiments in thin oxide / typical n+ doped poly-Si samples [128]. In this section, the presence of EFID following an initial degradation/recovery cycle is explored.

First, a TOPCon_E sample that did not undergo light soaking, labelled as ‘original’ sample was exposed to the same positive corona annealing discussed in Figure 39 (4 µA positive corona charge annealing at 175 °C). The expected severe degradation due to EFID is observed, as shown in Figure 45. Next, a sample which had undergone a full degradation and recovery cycle following light soaking under 1.1 suns at 175 °C (same conditions as Figure 36) for 411 hours was tested. In contrast to the result in [33], this sample also underwent

severe degradation under the EFID condition. The effective lifetime of the original specimen reduced from 7.5 ms to 1.9 ms after 4 h of positive corona annealing, while the effective lifetime of the recovered specimen took 1 h to reduce from 6.4 ms to 1.6 ms. The degradation rate is significantly faster for the recovered sample, compared with the original sample.

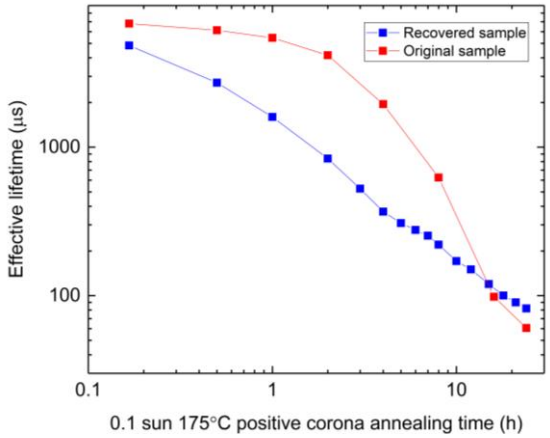

Figure 45. Effective lifetime changes of the TOPCon_E specimens under 12 μA positive corona charge during light soaking under 0.1 suns at 175 °C, comparing the response of a fresh sample and a sample that underwent degradation/recovery cycle. Only one sample was used for each illumination recovery test.

Under light soaking alone condition (Figure 36), the minimum lifetime during degradation is 2.6 ms. However, when a large positive surface field is applied, the lifetime degrades to < 100 μs (Figure 40). Additionally, the typical recovery behaviour (shown in Figure 36) is not seen for the sample that underwent EFID. This poses the question of whether the EFID process induces a new type of defect or whether it is simply enhancing the SRD seen during typical light soaking.

To test the nature of this defect, two degraded samples during EFID were exposed to 1.1 suns light-soaking conditions to assess whether they would recover. Figure 46.a shows the recovery of the effective lifetime change of the degraded nnnTOPCon and npnTOPCon specimens under 1.1 sun at 175 °C, while Figure 46.b shows the change of J_0 during the recovery process. For the nnnTOPCon samples with n-type substrate combined with n+ poly-Si layer, τ_{eff} recovers from 3.0 ms to 5.9 ms after 900 h treatment, which corresponds well with a decrease of J_0 from 45.6 to 27.3 fA/cm^2. For the npnTOPCon samples with p-type substrate combined with n+ poly-Si layer, τ_{eff} recovers from 331 μs to 439 μs after 900 h treatment, which corresponds well with a decrease of J_0 from 30.8 to 15.5 fA/cm^2. This shows that the EFID can be recovered by the light-soaking annealing treatment. The surface electric field mainly accelerated the SRD, not creating a new type of degradation.

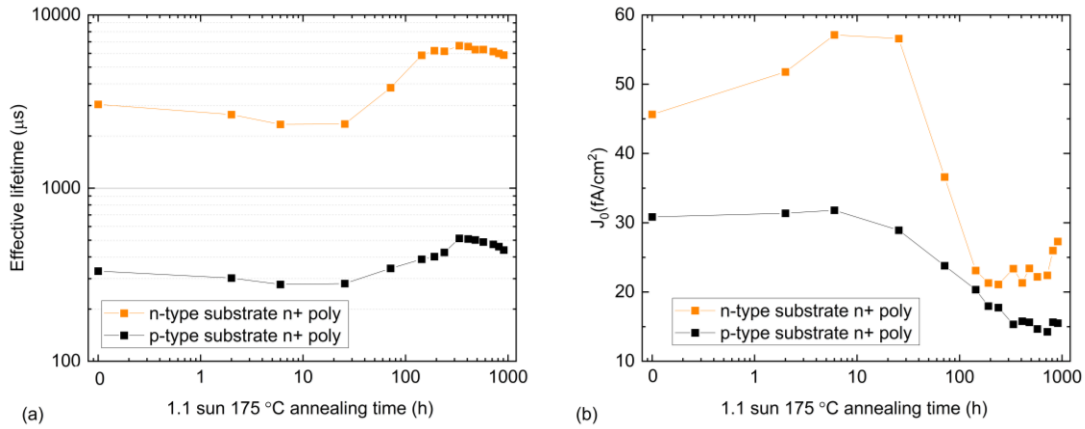

Figure 46. (a) τ_{eff} and (b) J_0 changes of the TOPCon lifetime specimens with n + poly silicon on both sides after EFID treatment during light soaking under 1.1 sun at 175 °C. Only one sample was used for each illumination recovery test.

5.11 Discussion

This chapter has unequivocally demonstrated the impact of surface polarisation on the surface passivation performance in TOPCon architectures under light soaking at elevated temperatures. Table 2 summarises all the possible processing sequences that can lead to the degradation of effective lifetime and J_0 change in TOPCon lifetime specimens. The well-known surface-related degradation (SRD) processes are first addressed: under 175 °C annealing, only a slight degradation of the effective lifetime takes place, with a loss of 9 % after 12 h treatment. The stable J_0 indicates that this degradation is not related to the deterioration of the surface passivation. Light soaking has a great impact on this surface-related degradation, and the intensity of illumination impacts the degradation process. For the symmetrical thin oxide / n+ doped poly-Si TOPCon lifetime specimens, 1.1 sun 175 °C annealing treatment can achieve the maximum lifetime loss of 60 % in 7.6 h, and further treatment can cause the recovery of the specimens, as seen in Figure 36 and sequence process C in Table 2. Under 0.1 sun 175 °C annealing condition, it took 12 h to achieve the same maximum degradation value, and there is no sign of recovery after 24 h treatment, as seen in Figure 39. This corroborates previous findings where the intensity of light soaking impacts the degradation rate and the time taken for recovery to begin [128].

I now turn my attention to EFID. Under a positive surface polarisation on the SiN_X layer, the deterioration of the surface passivation is accelerated at 175 °C without illumination (process A1+ in Table 2). 1µA continuous positive corona charge at the surface without light soaking will lead to a 27.5 % loss in lifetime and an increase in J_0 after 12 h treatment. The combination of positive surface polarisation and 0.1 sunlight

soaking led to more severe degradation. Increasing the positive corona charge current from 1 to 12 μA leads to an increase the amount of positive charge at the surface, which causes more severe degradation in the lifetime loss from 70.5% to 99.2 % in 24 h treatment with a pronounced increase in J_0 (process B1+, B4+ and B12+ in Table 2). However, the application of the negative charge on the surface does not impact the amount of degradation during light soaking (process B1-, B4- and B12- in Table 2). Application of the surface electric field affects the SRD process. Increasing positive corona charge on the n+ poly-Si/SiO_X surface significantly accelerates the degradation process.

I also find that the doped layer impacts the EFID behaviour of TOPCon samples during positive corona charge annealing at 175 ℃ with 0.1 sun illumination (process B4+ in Table 2). 4μA continuous positive corona charge at the surface will lead to around 67-85 % loss in lifetime and an obvious increase in J_0 after 24 h treatment in TOPCon architectures with n+ poly-Si / SiO_X stack. However, the TOPCon architectures with p-type substrate show different responses to the EFID process. A less pronounced degradation in the effective lifetime and almost no change in J_0 is observed. Comparing the change in τ_{eff} for the TOPCon lifetime specimens in the different passivation structures, it is found that whenever there is an n-poly Si /SiO_X interface, there is degradation from EFID, and this degradation is related to the deterioration of the surface passivation. For the specimens with p-type poly-Si /SiO_X interface, surface polarisation has a slight impact on the deterioration of surface passivation, while the loss mainly comes from the bulk. These results indicate that the defect concentration in the surface passivation layer is controlled by the applied surface electric field. Since the electric falls primarily across the SiN_X, I postulate that only a charged ion species could be involved in the degradation mechanisms and that it is most likely H inside the nitride, which has a very strong response to electric fields.

Table 2. Summary of degradation observations in TOPCon specimens with different architectures under light soaking at elevated temperatures with changes in the surface conditions.

Sample Structure	**ID**	**Process Sequence**	**Time (h)**	**Relative τ_{eff} degradation (%)**	**J_0 initial (fA/cm^2)**	**J_0 final (fA/cm^2)**
n-poly/n-Si/n-poly	A	Dark 175 ℃	12	9.03	20.70	19.70
	B	0.1 sun 175 ℃	12	55.86	18.30	36.50
	C	1.1 sun 175 ℃	7.6	59.24	14.40	41.70

	A1+	Dark 175 ℃, +ve corona (1 µA)	12	27.47	14.90	16.50
	B1+	0.1 sun at 175 ℃, +ve corona (1 µA)	24	70.49	19.80	41.30
	B4+	0.1 sun at 175 ℃, +ve corona (4 µA)	24	89.45	22.80	60.70
	B12+	0.1 sun at 175 ℃, +ve corona (12 µA)	24	99.19	19.00	539.00
	A1-	Dark 175 ℃, -ve corona (1 µA)	12	3.83	17.90	17.00
	B1-	0.1 sun at 175 ℃, -ve corona (1 µA)	24	59.69	18.60	40.60
	B4-	0.1 sun at 175 ℃, -ve corona (4 µA)	24	44.24	24.60	38.80
	B12-	0.1 sun at 175 ℃, -ve corona (12 µA)	24	62.64	22.90	43.60
n-poly/n-Si/n-poly	B4+	0.1 sun at 175 ℃, +ve corona (4 µA)	24	85.79	11.40	54.15
n-poly/p-Si/n-poly				67.17	13.28	30.85
p-poly/p-Si/p-poly				6.61	41.80	43.39
p-poly/n-Si/p-poly				34.46	35.88	36.29

I now contrast the findings of this work with the understanding of surface-related degradation (SRD) in the literature. In the manufacture of silicon solar cells, high-temperature firing is a critical step in achieving high efficiency [208-210]. The primary purpose of this step is to form the metal contact of the cells [211, 212]. Additionally, firing is used to drive hydrogen from hydrogen-containing dielectric layers (SiN_X:H and AlO_X:H) into the surfaces and bulk of cells [144, 213, 214] for passivation purposes. The introduced hydrogen plays an

important role in the mitigation of recombination in solar cells, as described in Chapter 2. However, the hydrogen introduced during firing from the hydrogenated passivating dielectrics can also induce light and elevated temperature-induced degradation (LeTID), which can cause significant losses in efficiency in the field, and occurs for a range of silicon solar cell architectures [27, 29, 103, 110, 112].

The hydrogen-induced defects in LeTID can affect both bulk and surface regions [215-217]. Most notoriously, it has been reported that LeTID can originate from the instability of the surface dielectric passivation layer [130, 166]. Sperber *et al.* reported the observation of the decrease in the surface passivation quality of FZ, Cz, and mc-Si specimens with either SiO_X/SiN_X:H or AlO_X:H/SiN_X:H layer stacks, during the light-induced degradation treatment [218]. They showed that the surface saturation current density (J_0) is a reliable method to separate the changes in the bulk and surface during the treatment. With this method, they showed that SRD tends to occur in a long-timescale over 1000 h. Kim *et al.* investigated the surface passivation quality of boron-doped p-type Cz-Si with SiN_X, AlO_X:H/SiN_X:H stack and thermally-grown SiO_2 layer in dark annealing at 175 ℃ [219]. They found that the degradation of the surface starts when the initial bulk degradation ends, and the surface degradation was later followed by a recovery process. This indicates there is a link between LeTID and SRD. No degradation was observed for the specimens with SiO_2 passivation layer, indicating a link between the hydrogen in the dielectric passivation layer and degradation in the surface passivation. All these works show that hydrogen in the dielectric layer plays an important role in the SRD in all cell architectures. Therefore, studying the kinetics of hydrogen is important to investigating and finding methods to mitigate the normal SRD phenomena.

SRD has also been reported to occur in samples with doped or undoped surfaces [29, 130, 166, 219]. Sen *et al.* investigated the impact of surface doping profile and passivation layers on SRD in PERC cells [220]. It was found that moving to the lightly doped emitters had a minimal impact on the bulk but led to more severe degradation in the surface, which could be related to the hydrogen behaviour in the surface with varied diffusion profiles. They found that the SRD was only observed for the PERC specimens with SiO_2/ SiN_X:H layer on the rear side, while none was observed for PERC specimens with AlO_X/ SiN_X:H layer on the rear side. The charge state and distribution of the hydrogen atoms inside the hydrogen-containing dielectric layer impact SRD. Although the actual defect causing this degradation is yet to be identified, several reports show that it should be related to the accumulation of hydrogen atoms in the near-surface region [219, 221, 222]. The surface conditions play an essential role in varying the extent of SRD and the surface passivation is controlled by the

hydrogen inside it. The cell efficiency is related to the stability of the passivation of the silicon surface and bulk defects [22, 56, 162]. Therefore, studying the kinetics of hydrogen near the surface region is critical to better understanding the stability of solar cells.

While initial SRD literature primarily investigated a non-conductive dielectric-silicon interface, the emergence of passivating contacts has shifted attention to heterojunctions and tunnelling interfaces. For example, the high efficiency of TOPCon solar cells is achieved through the excellent rear side passivation provided by the combination of a thin tunnel oxide and n+ doped polysilicon stack [81, 168]. Several works have reported firing-induced degradation of the passivation at the n+ poly / SiO_2 / c-Si interface in TOPCon architectures [32, 33, 126]. Di *et al.* correlated this degradation with a five-fold increase in the J_{0s}, which shows that this degradation is related exclusively to the surface, rather than the bulk [33]. Besides that, Di *et al.* used secondary ion mass spectrometry (SIMS) to correlate the SRD with an excessive concentration of hydrogen near the SiO_2 / c-Si interface [34]. They showed that the quality of the fired passivation layer is determined by the concentration of hydrogen atoms in this region after the firing step. Winter *et al.* investigated this firing-induced degradation in the architectures with the n+ poly-Si layer on the p-type and n-type Czochralski-grown silicon wafers that underwent industrial firing and subsequent light soaking and annealing treatments [32]. For the p-type specimens, a primary degradation and recovery cycle was observed at 185 ℃, independent of illumination, which was attributed to the boron-oxygen defects. For the n-type specimens, the degradation and recovery cycle was only observed for the specimens that underwent a rapid-firing step, and the lifetime values change corresponded well with the change of J_0.

The reduction and recovery of J_0 during the light-soaking annealing treatments indicates that changes result from deterioration of the surface passivation. Such standard SRD phenomenon is only observed for the n-type wafers and not p-type. As shown in Figure 44, TOPcon lifetime specimens with p-type substrate still suffer the degradation during the 0.1 sun 175 ℃ annealing with positive corona at the surface, but the almost stable J_0 change indicates that this degradation should be related to the bulk part [47, 117]. The lifetime and J_0 change for the specimens with different doping structures (process B4+ in Table 2) correspond well with the normal SRD phenomena. Besides that, Figure 46 showed that the lifetime of the TOPCon specimens with different dopant after EFID process can be recovered during the 1.1 sun 175 ℃ annealing treatment, which indicates that EFID process appears to accelerate SRD, not creating the new degradation phenomena. The application of the positive corona at the surface just accelerates the diffusion of the mobile H atoms to the n-

poly / SiO_X / n-Si interface. The impact of the EFID process on the SRD phenomena during the light soaking treatment as shown in Table 2 and the recovery phenomena of the EFID samples as shown in Table 3 show that there is a link between the hydrogen and SRD in TOPCon architectures during light soaking annealing treatment. Because hydrogen atoms have high diffusivity and exist in different charge states, related to the concentration and distribution of electrons and holes, it is proposed that the EFID phenomena indicated in Table 2 should be related to the hydrogen kinetics in TOPCon architectures during the degradation process.

I now turn my attention to the recovery processes that occur after extended exposure to elevated temperature and illumination treatments. Table 3 summarises the recovery observed for the TOPCon specimens with n-poly Si /SiO_X interfaces after the EFID process in this work. All the data shown here are the ratio between the measured effective lifetime and the initial lifetime before any treatment. The initial value means the initial lifetime without any light soaking treatment, in as received state. The τ_{eff} of a n-poly / n-Si / n-poly specimen lost around 55 % with an increase of J_0 of 24.98 fA/cm^2 after 12 h EFID treatment. With a further 900 h 1.1 sun 175 °C light soaking treatment, the τ_{eff} can be returned to 87 % of the initial value before any treatment with an obvious decrease of J_0. The application of positive surface polarisation contributes to the deterioration of the surface passivation of n-poly / n-Si / n-poly specimen and can be recovered by the 1-sun light soaking treatment. For the n-poly / p-Si / n-poly specimen, the τ_{eff} lost around 67 % of the initial value with an increase of J_0 of 17.57 fA/cm^2 after 12 h EFID treatment. However, the τ_{eff} can only be returned to 43.5 % of the initial value with J_0 almost back to the initial values. The recovered J_0 indicates that the deterioration of surface passivation is recovered after the normal light soaking treatment. However, there is still around 57 % loss of the lifetime, which is possibly related to the bulk lifetime [191, 223]. Due to the use of the p-type substrate wafer, the normal LID will lead to the degradation in the bulk. This loss could be related to the boron-oxygen defects and the hydrogen-induced defect in the bulk during the light soaking treatment [29, 224, 225]. The degradation of the n-poly / p-Si / n-poly specimen during EFID process is therefore related to the deterioration of both the surface passivation and the bulk defects. The n-type substrate specimens mainly suffer from the normal SRD during the EFID process, while the p-type substrate specimens mainly suffer from the degradation caused by the bulk defect during the EFID process.

When assessing these results against the literature on SRD and LeTID, it is clear that the charge state of the hydrogen atoms at different interfaces plays a role in the degradation phenomenon during the EFID process. Previous reports showed that no further degradation is observed for specimens after the degradation/recovery

cycle under the light soaking treatment [33, 128]. It was expected that the 1 sun 175 ℃ annealing treatment could transfer the hydrogen species into the deactivated states, free from the light-induced degradation. However, Figure 45 shows that recovered samples would degrade again, with a faster degradation rate, under EFID process. The original sample degraded from 7.5 ms to 1.9 ms after 4 h at 0.1 sun 175 ℃ 12 μA positive corona treatment, while the sample after the degradation/recovery cycle degraded from 6.4 ms to 1.6 ms after only 1 h treatment with a faster degradation rate. The degradation phenomena of the recovered specimen during the EFID process indicates that the recovery of the lifetime is not achieved through the effusion of hydrogen from, but through the deactivation of the mobile hydrogen inside of the TOPCon architectures. Applying the positive surface polarisation accelerates the SRD process and reinforces the proposed mechanism in which mobile charge atoms (H) inside the cells migrate and activate defects.

Table 3. Degradation and Recovery of TOPCon specimens after EFID treatment

Sample Structure	**Degradation (process 1)**	**Rel τ_{eff} after process 1 (%)**	**ΔJ_0 after process 1 (fA/cm^2)**	**Regeneration (process 2)**	**Rel τ_{eff} after process 1 + 2 (%)**	**ΔJ_0 (fA/cm^2) after process 1 + 2**
n-poly / p-Si / n-poly	1 sun 175 ℃, +ve corona (4 μA), 12 h	32.8	17.57	1.1 sun at 175 ℃	43.4	2.23
n-poly / n-Si / n-poly	1 sun 175 ℃, +ve corona (4 μA), 12 h	44.9	24.98	1.1 sun at 175 ℃	86.6	6.62
Where $Rel\ \tau_{eff} = \frac{\tau_{eff_{after\ process}}}{\tau_{eff_{initial}}}$ $\Delta J_0 = J_{0,after\ process} - J_{0,initial}$						

The results in this work provide valuable insight into understanding the role of hydrogen atoms in TOPCon specimens during light soaking. Comparing the conventional SRD in the previous literature part and

the EFID results in the previous sections, Table 2 and Table 3, there is some similarities between these two processes:

(i) The degradation is caused by the deterioration of the surface passivation, which correlates well with the degradation of the effective lifetime and increase of J_0.

(ii) The degradation is observed on the n-type substrate wafer, not on the p-type substrate wafer.

(iii) The degraded samples can be recovered by the normal light soaking treatment.

Here, I present a hypothesis about why the n+ poly-Si specimens experience a more rapid near-surface degradation under light soaking with positive surface polarisation at elevated temperatures. A model based on the redistribution of charged hydrogen atoms at the poly-Si layer and diffusion of hydrogen atoms inside TOPCon architectures under varied surface polarisation conditions is presented in Figure 47. The TOPCon passivating contact architecture, inclusive of the surface antireflection and hydrogenation SiN_x layer, has been simulated in SCAPS under 1 Sun illumination. In Figure 47.a the electronic band diagram for this structure is pictured without any surface polarisation in the nitride [226].

As described in Chapter 2, hydrogen is released from the SiN_X layer as the molecular H_2 or atomic hydrogen by restructuring the Si-H and N-H bonds after firing. Several works have found a prevalence of H^+ in the SiNx layer [227], and my model here is in agreement with such findings. The concentration of H at poly-Si / SiO_X/ c-Si interfaces increases significantly during the firing step, and hydrogen atoms still exist in the 10^{19} and 10^{21} cm^{-3} range within the SiN_X and poly-Si layers [34, 228]. Upon further treatment, hydrogen atoms can diffuse from the SiN_X layer to the other layers. The migration of hydrogen atoms is achieved via interstitial sites and is strongly affected by the internal electric fields due to the charged nature of H species (H^+ and H^-) [197, 229, 230]. Figure 47.b illustrates how the charge state of H atoms is controlled by the local concentration and distribution of electrons and holes, with H species predominantly existing in the H^- state in n-type silicon and the H^+ state in p-type silicon [125, 138, 151]. For the n-type poly-Si layer without surface polarisation, the concentration of the H^+ ions is significantly lower in the steady state, where H mainly exists as H^- ions and H-P bonds [31].

The concentration ratio $[H^-]/[H^0]$ is proportional to the concentration of electrons. Due to the high diffusivity [196], H^0 atoms have the possibility to diffuse to the SiO_X/c-Si interface. Due to the low concentration of H^0 in n+ poly-Si layer, the impact of the H^0 to the SiO_X/c-Si interface is small without surface polarisation. When a positive corona charge is applied on the top surface of the SiN_x layer ($Q \sim 10^{12}$ q/cm^2), as

shown in the simulation in Figure 47.c, an electric field drifts H^+ species from the nitride towards the polysilicon layer. Provided enough energy is available from temperature and illumination, the H species can cross the interface and get injected into the polysilicon. There, the H^+ can capture abundant electrons to transfer into H and H- ions. The increased concentration gradient of both H^- and H^0 (though note that H- will be the predominant specie) in the poly-Si will produce a diffusion of hydrogen across the poly layer and into the c-Si. I postulate that the presence of H species captured at the poly-Si/c-Si interface causes an increase in the defect concentration. I note here that the electric field produced by surface corona charge drops entirely in the SiN_x layer. Thus, only the charged species inside it should be responsive to changes in surface polarisation.

When the negative corona charge is applied on the top surface of the SiN_X layer, as shown in Figure 47.d, the concentration of H in the polysilicon remains unchanged since H in the nitride is pulled away from the interface. Any degradation process would proceed via the standard mechanisms earlier described. The effective lifetime change is similar to a specimen without corona charge, as shown in Figure 39 and Figure 41. The change of the magnitude of the negative corona on SiN_X layer has almost no impact, compared to the illuminated annealing samples. For the n-poly Si/ SiO_X specimens, the application of positive surface polarisation remains the major factor impacting the migration of H between poly-Si / SiO_X/ c-Si interfaces , leading to the loss in lifetime and increase in $J_{0,}$ as shown in Figure 44.a.

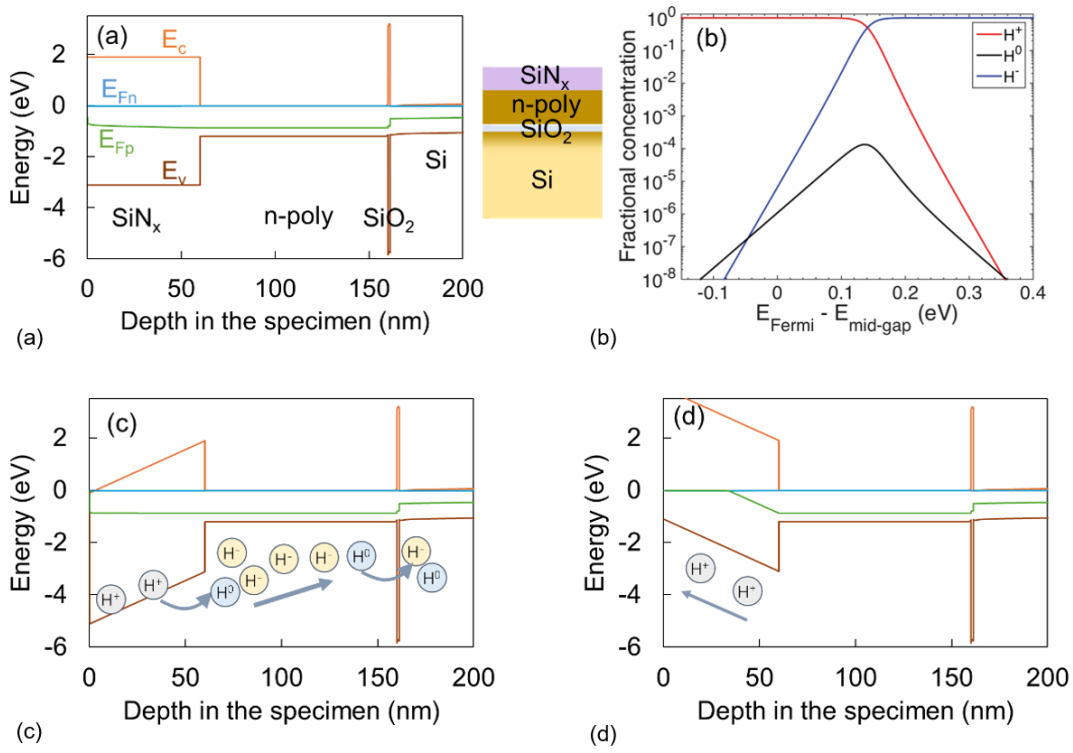

Figure 47. Schematic of band diagram and motion of hydrogen for the TOPCon architecture with structure of n-type polysilicon with n-type silicon substrate with varied surface polarisation under 1 Sun illumination. (a) without surface polarisation on the SiN_X film(b) the fractional concentration of hydrogen with different charge states as a function of Fermi level (relatively to the middle of the band gap), reproduced after [138] (c) application of positive corona charge on the SiN_X film (d) application of negative corona charge on the SiN_X film

The results presented herein mainly focus on the n+ poly-Si / tunnel SiO_x layers of the TOPCon cells. Figure 42 demonstrates the change in τ_{eff} for the TOPCon cell precursors without metal contact during exposure to various surface polarisation, with 0.1 sun light soaking at 175 °C. An increase in effective lifetime of around 0.3 ms was observed in positive anneal, negative anneal, and anneal-only specimens in the first 10 min 0.1 suns 175 °C annealing treatment. With further treatment, degradation was observed in all specimens. Only the specimen with positive corona annealing treatment suffered from severe degradation. Further studies on the difference between the p+ emitter / AlO_X:H / SiN_X:H interfaces and tunnel SiOx / n+ polysilicon / SiN_X:H layer interfaces could provide possible insight to identify the role of hydrogen across the whole TOPCon cell during light soaking. Thus, these results show that controlling the diffusion of hydrogen at different interfaces of TOPCon solar cells is critical to the stability in the actual field, and surface polarisation is a potential method for controlling the motion of hydrogen between different interfaces.

5.12 Summary

In this chapter, the impact of a surface electric field on the nature of this degradation is investigated. It is identified that the application of the positive charge on the surface drastically enhances the amount of surface-related degradation in the symmetrical thin oxide / n-type doped poly Si TOPCon lifetime structures. Increasing the amount of surface positive charge leads to more degradation and more pronounced increase in J_0. In contrast, the application of negative charge on the surface does not impact the amount of degradation for the symmetrical thin oxide / n-type doped poly-Si TOPCon lifetime structures. It is proposed that the cause of degradation is the accumulation of excessive hydrogen near the c-Si / SiO_X interface. Application of the surface polarisation impact of the migration of hydrogen ions inside the SiN_X film. Under the positive surface polarisation, H^+ ions will diffuse to the n-type doped poly-Si film and transfer to the H^- and H^0 ions. The increased concentration gradient of hydrogen atoms will cause the diffusion of hydrogen across the poly layer and into the c-Si, which increases the hydrogen-induced defect near the c-Si / SiO_X interface and causes the serve degradation. Under the negative surface polarisation, H^+ ions will diffuse to SiN_X film surface side and almost not impact the concentration change of H atoms inside the poly layer, which causes a similar degradation trend compared with the specimens under the anneal-only conditions. The application of the surface electric field via the corona charge method can provide insights into the role of hydrogen-induced deterioration of the surface passivation of the TOPCon architectures.

Chapter 6 Impact of surface polarisation on the enhancement of silicon heterojunction (SHJ) solar cells

6.1 Overview

This chapter investigates the impact of surface polarisation on the nature of light-induced improvements in SHJ architectures. The surface polarisation of SHJ lifetime samples was achieved by applying corona charge on a surface dielectric layer while the samples underwent light soaking at room temperature. A low-temperature (200 ℃) PECVD SiO_X deposition process is developed to enable SHJ lifetime specimens to hold a surface charge. It is observed that the combination of the positive charge on the n-type doped amorphous silicon surface and the light soaking process drastically enhances the lifetime of SHJ symmetric lifetime samples (a-Si (n) / a-Si (i) on both sides). Increasing the amount of surface charge leads to a higher enhancement rate. On the other hand, a negative corona charge does not have a significant impact. For the architectures with a-Si (n) / a-Si (i) and a-Si (p) / a-Si (i) on different sides, the combination of the corona charge (positive/negative) on the a-Si (n) surface and the light soaking process leads to the loss in the lifetime of them. It is hypothesised that the cause of instability is the movement of the excessive hydrogen to the a-Si:H(i) / c-Si interface under light soaking and the application of surface polarisation can be used to control the migration of hydrogen across interfaces.

6.2 Introduction

Chapter 2 introduced the previous literature on light soaking enhancement dynamics in SHJ specimens. The high efficiency of the SHJ architectures is achieved by a passivation stack comprising intrinsic amorphous silicon (a-Si) and doped a-Si nanolayers [87-89]. The stability under prolonged light illumination is essential for solar cell devices. Several studies have reported that light-soaking can enhance the performance of SHJ cells [35-37]. The enhancement is attributed to an improved lifetime, which has been tested in SHJ samples and occurs when the doped layer is present [35]. The efficiency of SHJ cells can be increased up to $0.7\%_{abs}$

after 30 seconds 100-sun illumination process at 200 ℃, which is highly desirable and compatible with industrial production [37]. Light soaking treatment shows great potential as an enhancement method in production. However, the mechanism behind light soaking enhancement in SHJ cells remains unclear. The hypothesis is that hydrogen migrates to the interface to improve surface passivation due to the electric field induced by the doped layers [136, 231, 232], but little understanding is yet available.

In Chapter 5, the application of surface electric fields showed the possibility of controlling the hydrogen migration inside cells with subsequent changes in the effective lifetime. This methodology was employed in this chapter to investigate the impact of light soaking enhancement on SHJ lifetime samples in the presence of varied surface electric fields through corona charging. Due to the conductivity of the amorphous silicon films, it is not possible to establish and directly modify the electric field on the surface of an SHJ sample. Therefore, I developed a 200 ℃ low-temperature PECVD SiO_X process to deposit the 1μm SiO_X layer on the surface of SHJ specimens, enabling them to hold charge without damaging the existing passivation. The application of the surface electric field impacts the effective lifetime change of the SHJ sample during light soaking, which provides further evidence that the light-induced enhancement should be related to the motion of charged ions at/near the interface, most likely hydrogen.

6.3 Experimental Procedure

Experiments in this work were carried out on four types of SHJ lifetime architectures and Figure 1 schematically displays the geometry of the investigated specimens. Symmetrical n-type amorphous silicon (a-Si(n)) / intrinsic amorphous silicon (a-Si(i)) samples and standard SHJ cell precursor without transparent conductive film and metal contacts were used as starting samples, identified as *ni*/Si/*in* shown in Figure 48.a and *ni*/Si/*ip* shown in Figure 48.b respectively. Then, 1 μm SiO_X is deposited on the *in* side for both architectures with 150 sccm of silane (SiH_4) and 730 sccm of nitrous oxide (N_2O) flowed and decomposed in a plasma reactor with 80 W RF power at 200 ℃, with a base pressure of 1200 mTorr for 11min 50 s, as identified as SiO_X/*ni*/Si/*in* in Figure 48.c and SiO_X/*ni*/Si/*ip* in Figure 48.d.

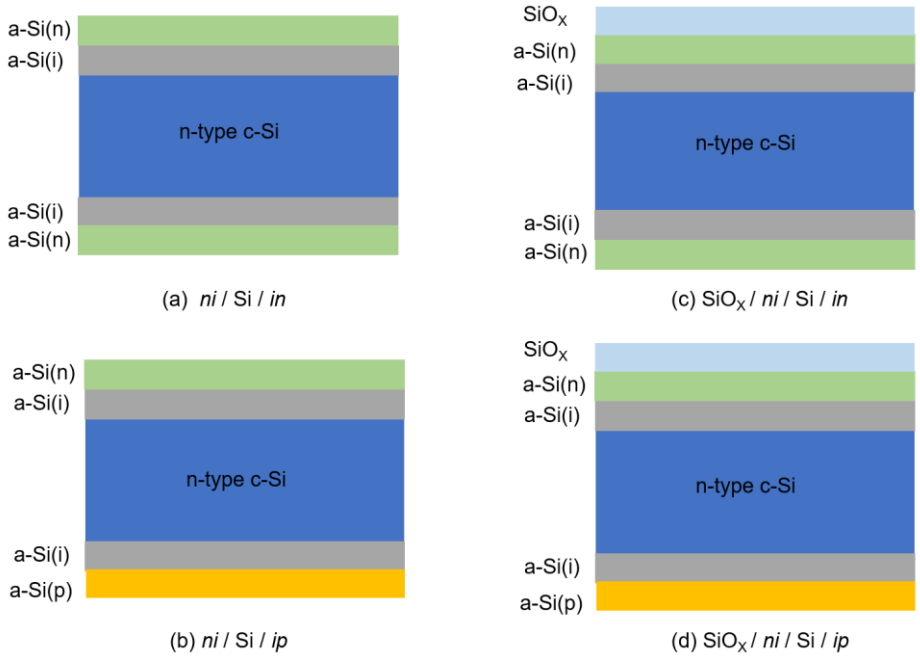

Figure 48. Schematic of the geometry of SHJ lifetime specimen. (a) symmetrical lifetime structures with both sides passivated with a bilayer consisting of intrinsic amorphous silicon (a-Si(i))/n-type doped amorphous silicon (a-Si(n)), identified as *ni*/Si/*in* (b) lifetime structures with a-Si(i)/ a-Si(n) on the front surface and a-Si(i)/ with p-type doped amorphous silicon (a-Si(p)) on the rear from group K, identified as *ni*/Si/*ip*. (c) *ni*/Si/*in* specimens with 1µm SiO_X layer on a-Si(i) side. (b) *ni*/Si/*ip* specimens with 1µm SiO_X layer on a-Si(i) side.

Figure 49 shows the schematic of the measurement set-up and test conditions for the SHJ lifetime specimens. Four LED lamps above the corona charge box form a 5 × 5 cm^2 illuminated area on the Al stage with an intensity of 1 sun. The 4 × 4 cm^2 lifetime specimens were placed in the centre of the illuminated area. Figure 49.a shows the measurement set up for the *ni*/Si/*in* and *ni*/Si/*ip* specimens under 1sun light soaking on *ni* side without corona charge at 70 ℃. Then, corona charge was applied on the SiO_X/*ni* side for SiO_X/*ni*/Si/*in* and SiO_X/*ni*/Si/*ip* specimens in the dark box at 25 ℃ to study the impact of surface polarisation alone at first, as shown in Figure 49.b. Then, 1 sun illumination was added on SiO_X/*ni* side shown in Figure 49.c to study the impact of surface polarisation on light-induced enhancement of SHJ specimens. For all the test with corona charge treatment in the chapter, the corona charging was performed continuously through the experiment, due the limitation of the stability of the corona charged ions on the low-temperature deposited SiO_X layer. The τ_{eff} of the SHJ samples is extracted at a fixed excess carrier concentration of $\Delta n = 1\times10^{15}$ cm^{-3}, before and after each step of the corona charging illumination process. With control of light illumination, surface polarisation generated by corona discharge, the impact of the surface polarisation of the change for τ_{eff} on SHJ lifetime specimens during light illumination is investigated. The effective lifetime was measured using a Sinton WCT 120 instrument.

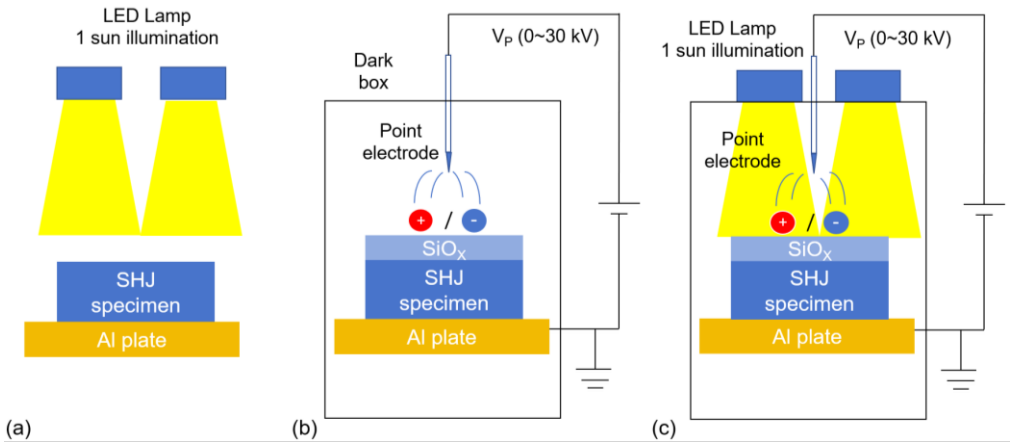

Figure 49. Schematic of measurement set up and test conditions for the SHJ lifetime specimens. (a) 1 sun illumination without surface polarisation at 70 ℃. (b) surface polarisation without light illumination at 25 ℃. (c) surface polarisation with 1 sun light illumination at 25 ℃.

6.4 Enhancement of SHJ lifetime samples under light illumination

Previous reports have shown an enhancement in SHJ lifetime specimens with doped layers under 25℃ 1 sun illumination [35]. To verify the enhancement behaviour, *ni*/Si/*in* and *ni*/Si/*ip* specimens were subjected to 1 sun light soaking on the Al plate without corona charging, as shown in Figure 49.a. To accelerate the enhancement process, the temperature was increased to 70 ℃. Two 4 × 4 cm^2 *ni*/Si/*in* lifetime specimens were tested, labelled as D1-1 and D1-2 respectively. Two 4 × 4 cm^2 *ni*/Si/*ip* lifetime specimens were tested, labelled as E1-1 and E1-2 respectively.

Figure 50 shows the change of τ_{eff} of two *ni*/Si/*in* specimens (D1-1 and D1-2) and the PL image of the tested specimens after light soaking treatment. The effective lifetime of D1-1 specimen increased from the initial value of ~ 11.3 ms, reaching a maximum value of ~ 13.0 ms after 2 h treatment, as shown in the red curve in Figure 50.a. After 90 h light soaking treatment, the enhancement of τ_{eff} for D1-1 specimen was stable. The effective lifetime of D1-2 specimen increased from the initial value of ~ 9.9 ms, reaching almost the maximum value of ~ 11.8 ms after only 0.5 h, 1 sun, 70 ℃ annealing treatment, as shown in the blue curve in Figure 50.a. With further treatment, the τ_{eff} for D1-2 specimen decreased almost to its initial value after 4 h. There was no further enhancement observed after the total 90 h. The control sample was kept in the dark box at 25 ℃ and its effective lifetime was stable during the lifetime measurement, black curve in Figure 50.a. This indicates that the measurement process does not change the τ_{eff} of SHJ lifetime specimen and the τ_{eff} of *ni*/Si/*in* specimens was stable under storage. Figure 50.b shows the PL image of D1-1 and D1-2 specimens after the

light soaking treatment. The intensity of the luminescence is proportional to the density of non-equilibrium minority carriers at this position. Defects in the sample act as recombination centres, appearing as dark dots, lines or areas in the PL image. The PL images of D1-1 and D1-2 specimens have uniform brightness with a series of dark dots on the edges and the dark area at the coroners. These dark lines were the scratches and microcracks introduced by the tweezer and dicing pen during the dicing and transport process.

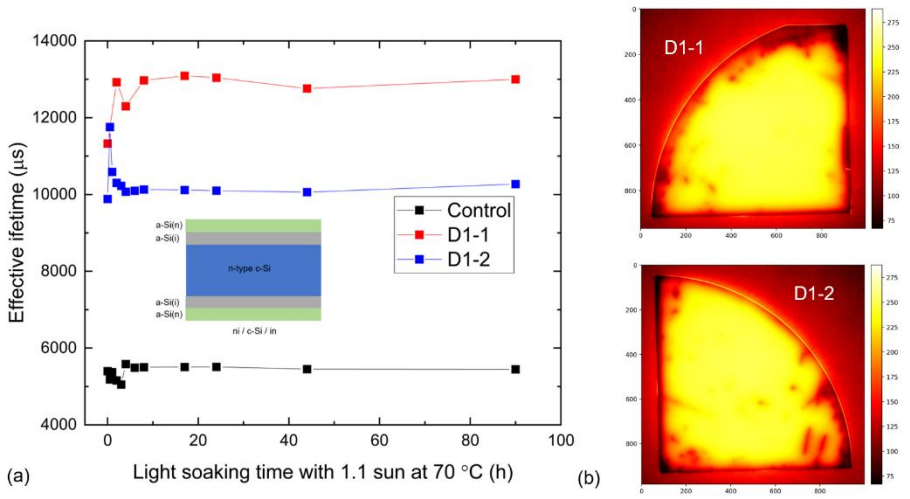

Figure 50. The change of τeff of ni/Si/in specimens under 1 sun light soaking at 70 °C. (a) The τeff change of D1-1 and D1-2 specimens. (b) PL image of D1-1 and D1-2 after 90h light soaking treatment. Only one sample was used for each test condition.

Figure 51 shows the change of τ_{eff} of two *ni*/Si/*ip* specimens (E1-1 and E1-2) under 1 sun illumination at 70 °C and the PL images of the tested specimens after light soaking treatment. The effective lifetime of E1-1 specimen increased from ~ 3.5 ms, reaching a maximum value of ~ 4.2 ms after 8 h treatment, as shown in the red curve in Figure 51.a. After the total 122 h treatment, the enhancement of τ_{eff} for D1-1 specimen was stable. The effective lifetime of E1-2 specimen increased from ~ 4.1 ms, reaching ~ 4.7 ms after 8 h treatment, as shown in the blue curve in Figure 51.a. With a further 1 sun light soaking treatment, the τ_{eff} for D1-1 specimen decreased to 4.3 ms after 122 h. The control sample was stable during the lifetime measurement, as shown by the black curve in Figure 51.a . Figure 51.b shows the PL image of E1-1 and E1-2 specimens after the light soaking treatment, showing uniform brightness with a series of dark streaks and dot regions.

Enhancement behaviours during the 1 sun light soaking were observed both on the *ni*/Si/*in* and *ni*/Si/*ip* lifetime specimens. The physical condition of the sample surface after manufacturing and during the process seems to impact the rate of lifetime enhancement. Unintended scratches and microcracks could damage the passivation layer, which would occur more prominently the more time the samples are moved between

different set-ups, which could lead to a decrease in the lifetime after prolonged manipulation. This would explain some of the sample variation observed.

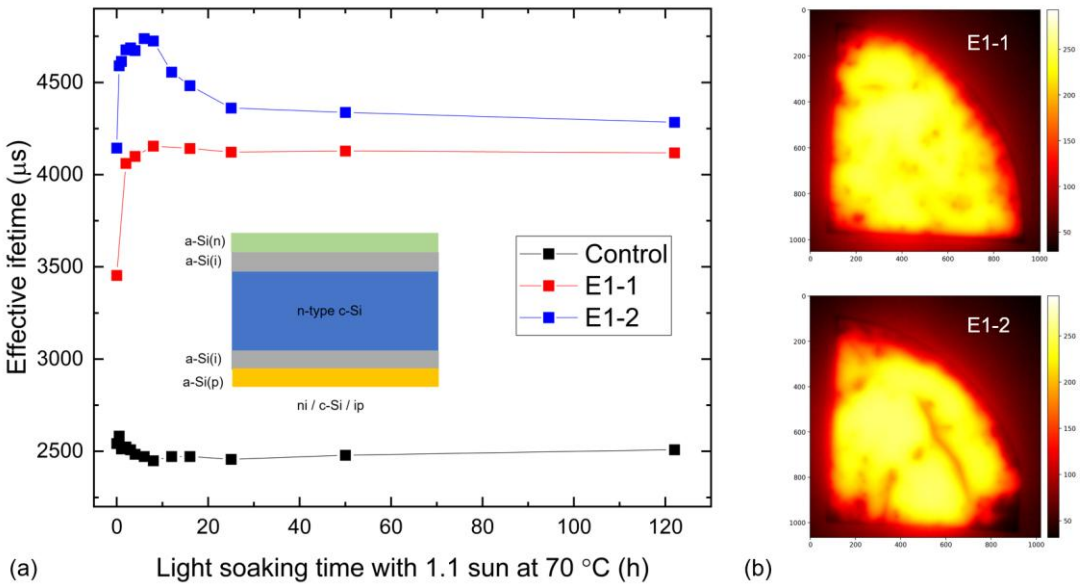

Figure 51. The change of τ_{eff} of *ni*/Si/*ip* specimens under 1 sun light soaking at 70 ℃. (a) The τ_{eff} change of E1-1 and E1-2 specimen (b) PL image of E1-1 and E1-2 after the light soaking treatment. Only one sample was used for each test condition.

6.5 Development of a low-temperature PECVD SiOx

To allow for the application of corona charge onto SHJ sample surfaces, a low-temperature PECVD SiO_X process is developed. PECVD has been widely used for the deposition of the SiO_X layers with a temperature around 300 ℃ [233, 234]. However, the intrinsic hydrogenated amorphous silicon layer is only stable up to 200 ℃, while higher temperatures causing deterioration in the passivation quality [235]. My aim was to develop a low-temperature PECVD process such that the SiO_X dielectric layer would have the ability to hold sufficient charge on the surface without damaging the passivation.

Due to the limited source of SHJ lifetime specimen, the PECVD development was carried out on 675 μm n-type Cz silicon wafers, 30-60 Ω.cm at first. The silicon wafers were diced into 4 x 4 cm^2 specimens. Then, they underwent RCA cleaning, as shown in Table 4. After, the SiO_X layer was deposited with different PECVD recipes using an Oxford Instruments PlasmaLab 80+ system. The SiO_X layer was deposited on one side of all specimens. Then, the specimens were taken out immediately and cooled in the air at RT before storing.

Table 4. The RCA Cleaning process for Si wafer before PECVD process

Step	Solution	Temperature (℃)	Time (min)
RCA 1	1:1:5 (ammonia: H_2O_2: DI water)	85	10
Rinse	DI water	25	5
RCA 2	1:1:5 (HCl: H_2O_2: DI water)	85	10
Rinse	DI water	25	5
HF dipping	10%	25	1
Rinse	DI water	25	5

6.5.1 Temperature selection

At first, the stability of the SHJ lifetime specimens at elevated temperatures is tested. Due to the limited source of the SHJ lifetime specimen, only one *ni*/Si/*in* specimen (D2-1) is tested in the range from 100 ℃ – 250 ℃ with 10 min time interval. After each annealing step finished, the sample was cooled in the air and the effective lifetime was measured at 25 ℃. Figure 52 displays the effective lifetime response of specimen D2-1 to the annealing process. The initial τ_{eff} of D2-1 specimen is 12.2 ms at 25 ℃. When the temperature is increased to 100 ℃, the τ_{eff} of D2-1 is highly stable with a value around 12.1ms after 10 min treatment. When the temperature is increased to 150 ℃, a clear decrease in lifetime is observed with loss of around 2 ms. When the temperature is increased to 200 ℃, the τ_{eff} of D2-1 is decreased to 9.7 ms. After a further 10 min 225 ℃ annealing, the τ_{eff} of D2-1 decreased to 9.1 ms. When the temperature is increased to 250 ℃, almost 55% of the lifetime is lost. Considering the stability of the SHJ specimen at elevated temperature and temperature needed for PECVD SiO_X deposition, 200 ℃ is chosen a a reasonable balance between PECVD SiO_X deposition and low SHJ specimen degradation.

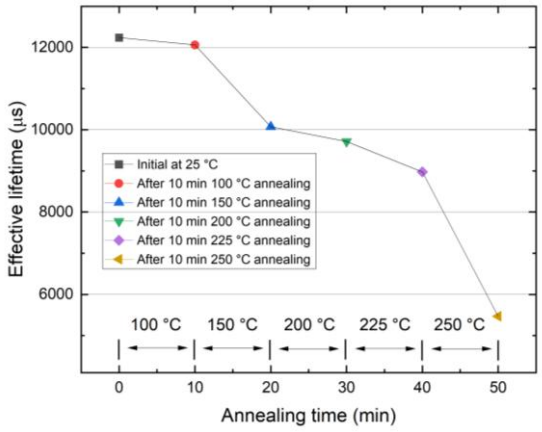

Figure 52. Stability of *in*/Si/*in* in the range of 100 ℃ – 250 ℃. Only one nnSHJ sample was used for this test.

6.5.2 Optimisation of deposition parameters

After the temperature was selected at 200℃, I varied the gas ratio, chamber pressure and RF power to optimise the PECVD SiO_X deposition recipe. All the initial recipe optimisation works were carried out on the n-type silicon wafers from Oxfrod. The charge-holding ability and effective lifetime loss caused by the PECVD deposition process were chosen as the key parameters. For the charge-holding ability test, the specimens with the deposited SiO_X layer were positively corona charged for 2 mins with a tip voltage of 30 kV at a distance of around 16 cm. The specimens were immediately followed by KP contact potential difference (CPD) measurement in the dark, for 5 minutes, to assess the charge concentration and stability. In this section, Table 5 summarised the best recipes (recipes A and B) and the detailed tested recipe results are shown in Appendix A.

Table 5 . Best Low temperature PECVD SiO_X recipes

Recipe	**SiH_4 flow rate (sccm)**	**N_2O flow rate (sccm)**	**Pressure (mTorr)**	**RF power (W)**	**T (℃)**	**Time (min)**
A	120	760	1000	20	200	1 min 51 s
B	150	730	1200	80	200	1 min 51 s

Figure 53 shows the n-type Cz-Si wafer samples with top performance with top recipes A and B. For the recipe A, 93 nm SiO_X layer shows a good ability for charge holding and the best stability of the charge storage. After a positive corona charge was applied on the SiO_X layer for 2 mins (30kV, 16cm), the CPD changed from -776.7 mV to -1498.4 mV. When the charged specimen was kept in a dark box for 5 min, the CPD changed from -1498.4 mV to -1438.3 mV. For the recipe B, 77 nm SiO_X layer shows good stability of the charge storage and the best ability of the charge holding. After a positive corona charge was applied on the SiO_X layer for 2 mins (30kV, 16cm), the CPD changed from -429.7 mV to -1949.1 mV. When the charged specimen was kept in a dark box for 5 min, the CPD changed from -1949.1 mV to -1602.6 mV. To achieve enough driving force for the charged hydrogen atoms inside the SHJ specimen through the corona charge process, the SiO_X layer with the highest CPD change is considered. Therefore, recipe B is chosen for the SiO_X deposition in SHJ samples. The instability of the corona charge could be related to the pin-holes generation during the deposition process and the annealing process over 500 ℃ could mitigate that problem [236]. However, the lifetime of the

test SHJ specimens could lost around 50% of the lifetime over 250 ℃. It has been reported that 1 μ m SiO_X can be deposited on a-Si layer for holding charge [237]. Then, I just did 10 cycles of PECVD SiO_X deposition with the recipe B to achieve 1μm SiO_X layer, which reduces the possibility of the pin-holes gathering at the certation region.

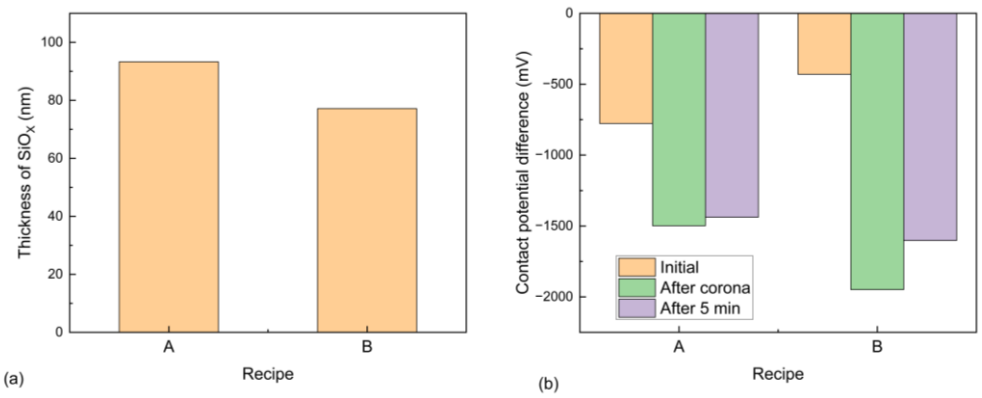

Figure 53. The thickness and charge-holding ability of PECVD SiO_X with recipe A (20 W RF power at 200 ℃, 120 sccm of SiH_4 and 760 sccm of N_2O flow with a base pressure of 1000 mTorr) and B (80 W RF power at 200 ℃, 150 sccm of SiH_4 and 730 sccm of N_2O flow with a base pressure of 1200 mTorr). (a) deposition thickness. (b) the charge-holding ability of deposited SiO_X layer. Only one sample was used for each test condition.

Recipe B SiO_x was tested on *ni*/Si/*in* and *ni*/Si/*ip* specimens. Figure 54.a shows the τ_{eff} change of the *ni*/Si/*ip* specimen before and after SiO_X deposition. After 1 μm SiO_X was deposited, the τ_{eff} of the *ni*/Si/*in* specimen increased from 11.7 ms to 12.5 ms. After application of 1 sun light soaking on the SiO_X side, the τ_{eff} decreased to 11.3 ms after 5 mins treatment. With the further 3 h treatment, the τ_{eff} increased to 12.9 ms. However, with a further light soaking treatment, the τ_{eff} decreased to 11.2 ms after 32 h, like the specimen D1-2 shown in Figure 51. Figure 54.b shows the τ_{eff} change of the *ni*/Si/*ip* specimen before and after SiO_X deposition. After 1 μm SiO_X was deposited, the τ_{eff} of the *ni*/Si/*ip* specimen increased from 4.0 ms to 4.4 ms. After application of 1 sun light soaking, the τ_{eff} decreased to 4.3 ms after 5 mins treatment. With the further 4 h treatment, the τ_{eff} increased to 4.4 ms. With further light soaking treatment, the τ_{eff} decreased to 4.3 ms after 24 h treatment, like the specimen E1-2 shown in Figure 52. The deposition of SiO_X process didn't kill the lifetime of the SHJ specimens and the effective liftime of SHJ specimens with top SiO_X layer still can be enhanced by the illumination process, which show that the 200 °C PECVD SiOx process with recipe B is suitable for the further surface polarisation test.

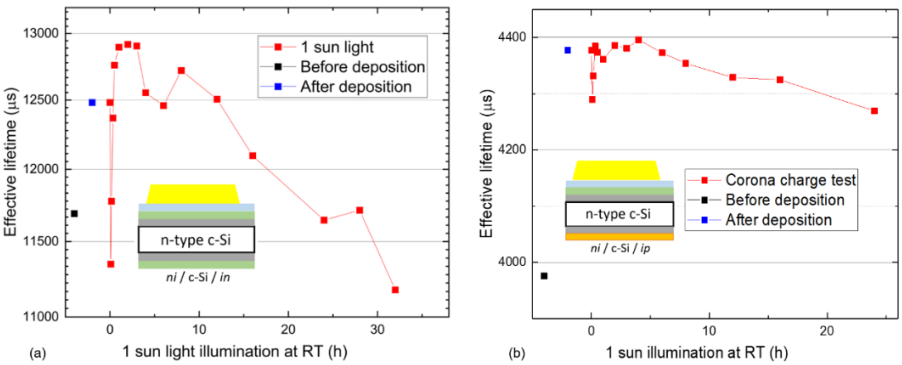

Figure 54. The change of τ_{eff} of SHJ lifetime specimens with SiO_X layer on a-Si(n) side under 1 sun light soaking at 25 °C. (a) SHJ_L specimen (b) SHJ_M specimen. Only one sample was used for each test condition.

6.6 Surface polarisation without illumination on SHJ specimens

In section 6.4, enhancement behaviours were observed in *ni*/Si/*in* and *ni*/Si/*ip* specimens under 1 sun illumination. To investigate the impact of surface polarisation on light soaking enhancement, the impacts of the surface polarisation and the light illumination are isolated. SiO_X/*ni*/Si/*in* and SiO_X/*ni*/Si/*ip* specimens were tested only in the presence of the corona charge without illumination, as shown in Figure 55. Figure 55 displays the effective lifetime change of SiO_X/*ni*/Si/*in* and SiO_X/*ni*/Si/*ip* specimens in the dark at RT with different surface polarisation conditions. As shown in Figure 55.a, the effective lifetime of SiO_X/*ni*/Si/*in* samples degrades from 13.5 ms to 12.2 ms after SiO_x deposition. After 90 mins of positive corona charging at RT, the effective lifetime was increased from 12.2 ms to 13.2 ms. When the polarity was switched to negative corona charging, the effective lifetime remained almost stable at around 13 ms. Figure 55.b shows the case for the SiO_X/*ni*/Si/*ip* specimens. The effective lifetime increased from 3.7 ms to 4 ms after SiO_x deposition. When negative corona charging was applied at RT on the *in* side, the effective lifetime decreased from 4 ms to 3.6 ms after 90 mins. For positive corona charging, the effective lifetime showed an initial improvement and then stabilised around 3.8 ms after 90 mins treatment. Based on these results, the application of the surface polarisation has a small but noticeable impact on the effective lifetime change without illumination, likely as a combination of field effect passivation or mobile hydrogen ion migration at room temperature.

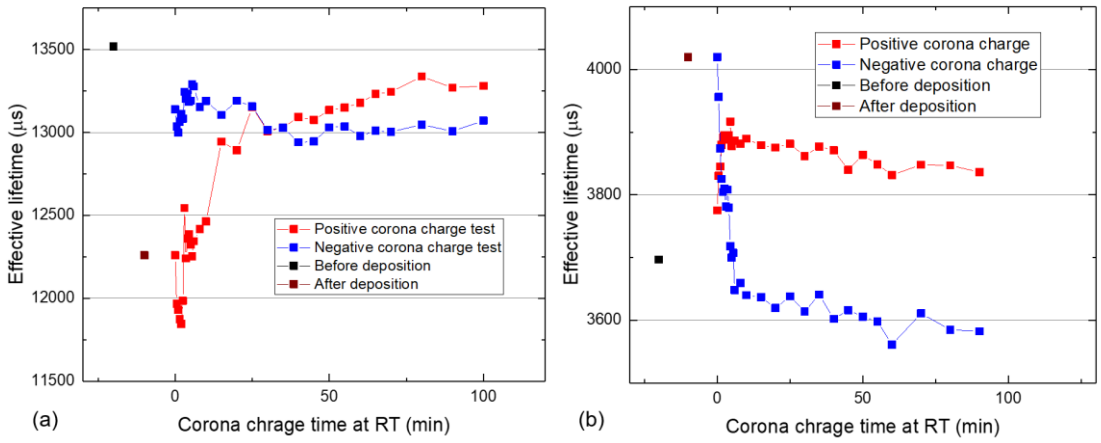

Figure 55. Impact of corona charge on τ_{eff} of SHJ lifetime samples at 25 °C without light illumination. (a) SiO_X/*ni*/Si/*in* specimen (b) SiO_X/*ni*/Si/*ip* specimen. Only one sample was used for each test condition.

6.7 Surface polarisation with illumination on SHJ specimen

Figure 56 displays τ_{eff} change for SiO_X/*ni*/Si/*in* sample and SiO_X/*ni*/Si/*ip* samples with top SiO_X layer under different corona charge conditions with 1 sun light illumination. For the SiO_X/*in*/Si/*in* sample shown in Figure 56.a, when no corona charge was applied on the sample at RT, the effective lifetime increased from 11.4 ms to 13 ms at first and slightly decreased to 11.2 ms after 32 hours. When positive corona charging was additionally applied on top *in* side, the effective lifetime increased from 12 ms to 15 ms within 1 hour and saturated around 14.7 ms after 32 hours. This is much larger than the result obtained using only corona charging in Figure 55.a for the SiO_X/*ni*/Si/*in* specimens and only illumination in Figure 54.a for the SiO_X/*ni*/Si/*in* specimen, indicating that the improvement relies on the combination of illumination and polarisation. When negative corona charge was applied, the effective lifetime stabilised at around 12 ms. For the SiO_X/ni/Si/ip sample shown in Figure 56.b, when only 1 sun illumination was applied on the sample at RT, the effective lifetime remained at around 4.4 ms. When the positive corona charge was applied on the top side, the effective lifetime showed a similar trend to the sample without corona charge, which increased around 0.1 ms initially but reduced by 0.3 ms after 24 hours of treatment. The application of a negative charge to the surface caused slightly more degradation in this SiO_X/*in*/Si/*ip* sample, which lost 0.5 ms effective lifetime in 24 hours. These results indicate that surface polarisation can have a large impact on the observed light soaking enhancement in SHJ cells, and further understanding can be obtained when considering the effect of surface electric fields upon the light and elevated temperature dynamics of H in silicon heterojunction structures.

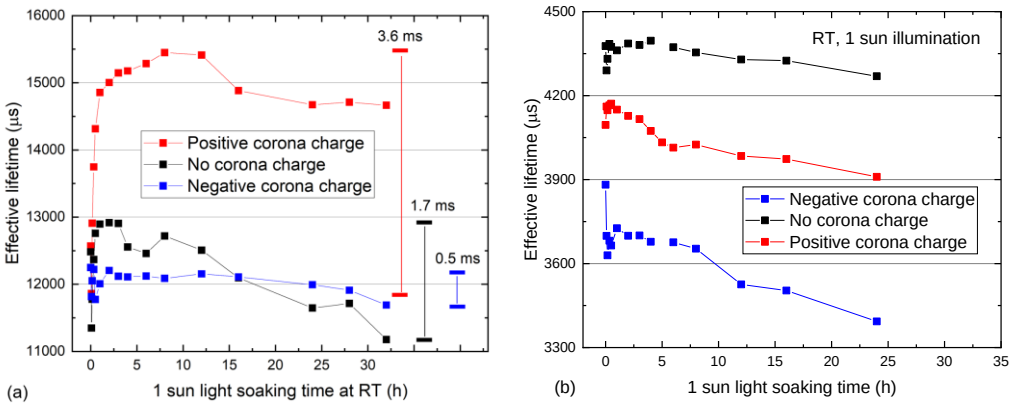

Figure 56. Impact of corona charge at room temperature under 1 sun light illumination on SHJ lifetime samples. (a) SiO_X/*ni*/Si/*in* specimen (b) SiO_X/*ni*/Si/*ip* specimen. Only one sample was used for each test condition.

6.8 Impact of magnitude of surface polarization

In the previous section, it was demonstrated that the positive charge on the surface of SiO_X/*in*/Si/*in* sample improves the lifetime under 1 sun illumination at 25 °C, while negative corona seems to mitigate this improvement. For the SiO_X/*ni*/Si/*ip* sample, applying the negative charge on the *in* side caused more degradation, while positive corona and no corona show a similar enhancement trend. In this section, the magnitude of the applied corona charge was varied to study the impact of the strength of the surface polarisation on the τ_{eff} change of SHJ lifetime specimens. Figure 57 shows the effective lifetime change for SiO_X/*ni*/Si/*in* sample and SiO_X/*ni*/Si/*ip* samples, under different corona charge conditions, with 1 sun illumination at RT. For the SiO_X/*ni*/Si/*in* sample, the application of 2 µA induces an improvement in lifetime around 2.1 ms, as shown in Figure 57.a. Increasing the corona magnitude to 5 µA significantly increases the rate and extent of enhancement, with the increase of lifetime around 3.4 ms. Further increasing the corona discharge to 8 µA causes the lifetime to increase around 3.5 ms after 24 h treatment. Increasing the magnitude of the positive charge on the in/in sample surface impacts the amount of light-induced enhancement. This shows that surface passivation can be modulated by the presence of a surface electric field, further supporting the hypothesis that the changes are caused by the movement of charged particles. For the SiO_X/*ni*/Si/*ip* sample, the application of 2 µA negative corona induces a lifetime degradation of ~1.1 ms, as shown in Figure 57.b. However, increasing the corona magnitude to 5 µA only causes a loss of lifetime around 0.36 ms. The initial lifetime of the specimens with 5 µA negative corona is only 3.9 ms, which is much lower than the other negative corona-charged specimens. The lower loss of the specimen with this process could be related to the initial physical damage in the wafer after dicing, due to the much lower initial lifetime compared with

specimens with 2 or 8 μA negative corona current. The bad initial wafer condition could lead to less loss in lifetime during the negative corona treatment. Further increasing the negative corona discharge to 8 μA causes the lifetime to degrade to 1.5 ms. Negative corona on the *in* side can mitigate the enhancement of SiO_X/*ni*/Si/*ip* samples during light soaking. Based on these results, increasing the magnitude of the positive charge on the surface of SiO_X/*ni*/Si/*in* specimens impacts the amount of enhancement. This shows that surface polarisation impacts the light-induced changes in the passivation of SHJ specimens, supporting the hypothesis that the movement of charged particles must be part of the process.

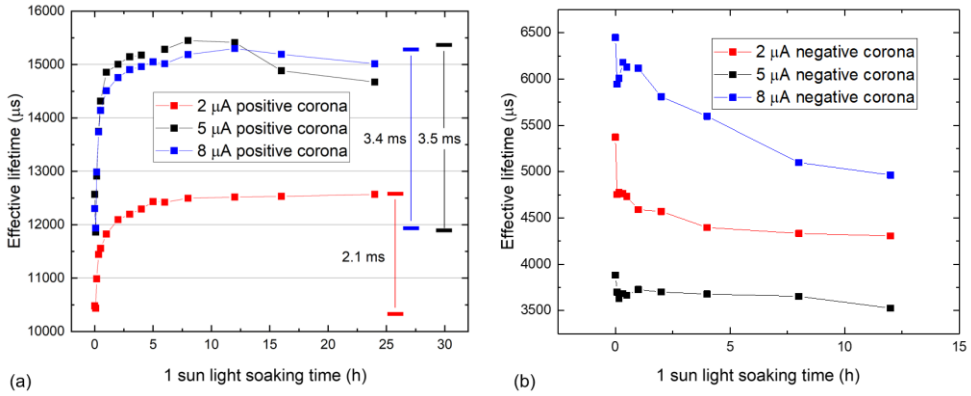

Figure 57. Impact of the magnitude of surface polarisation at 25 ℃ under 1 sun light soaking on SHJ lifetime samples. (a) SiO_X/*ni*/Si/*in* specimen (b) SiO_X/*ni*/Si/*ip* specimen. Only one sample was used for each test condition.

6.9 Discussion

This chapter has demonstrated the impact of surface polarisation on the effective lifetime change of SHJ architectures under light soaking. Table 6 summarises all the processing sequences tested in this chapter, that lead to effective lifetime changes. The well-known light-induced enhancement processes are first addressed in the literature [35]. At a temperature of 25 ℃ with 1 sun illumination, an enhancement of effective lifetime takes place for the SHJ specimens with doped layers, with an improvement between 10 - 40 % after 18 h treatment. The enhancement rate is impacted by the intensity of illumination [35, 37]. Under 70 ℃ annealing with 1 sun illumination (process A in Table 6), an enhancement in the effective lifetime of 15-20 % is observed both in the specimens with the structure of *ni*/Si/*in* and *ni*/Si/*ip*. The increased temperature accelerates the enhancement rate. Besides that, the surface conditions also impact the enhancement process, with cracks or scratches on the specimens causing a further loss in lifetime during the prolonged processing, as shown in Figure 50 and Figure 51.

I now focus on the impact of surface polarisation on the lifetime change of SHJ samples at RT. I will discuss the results in the following order:

1. Surface polarisation only (process B in Table 6)
2. Surface polarisation combined with 1 sun illumination (process C in Table 6)

For the *ni*/Si/*in* SHJ specimen with corona charge on *in* side without illumination, the positive corona leads to a lifetime enhancement of around 10.7 % in 1.5 h treatment, while the negative corona has almost no impact. For the *ni*/Si/*ip* SHJ specimen, the negative corona causes a 10.9 % loss in 1.5 h treatment, while the positive corona has almost no impact. Based on the results of process B, there were two findings:

1. Surface polarisation impacts the lifetime change of the SHJ specimens
2. The doped layer on the opposite sample side from where the polarisation is applied can impact the lifetime changes.

After combining the surface polarisation and light soaking treatment, there were some differences between the responses of the two architectures. For the *ni*/Si/*in* SHJ specimen, the combination of the positive surface polarisation and 1 sun light soaking (process C+ in Table 6) leads to a significant increase in lifetime (+23%), much larger than that provided by illumination alone (process A, C in Table 6), or by surface polarisation alone (process B in Table 6). Increasing the amount of surface charge from 2 to 8 μA corona charge current (C2+, C5+ and C8+ in Table 6) increases the enhancement. Negative surface polarisation (process C5- in Table 6) mitigates the possible improvements from light soaking and instead causes a slight loss of 1.3 %. For the *ni*/Si/*ip* SHJ specimen, the combination of the negative surface polarisation on *in* side and 1 sun light soaking (process C- in Table 6) leads to a significant loss in lifetime (-20%), while positive surface polarisation leads to a slight loss (-2%).

The results shown in process B and C indicate two key findings:

1. Surface electric fields can modulate light-soaking enhancements in SHJ samples.
2. The direction of the field impacts this modulation.

Table 6. Summary of lifetime change in SHJ lifetime specimens with different architectures under light soaking at room temperature with changes in the surface conditions.

Sample Structure	**ID**	**Process Sequence**	**Time (h)**	**Initial τ_{eff} (ms)**	**Final τ_{eff} (ms)**	**Relative τ_{eff} change (%)**

ni/Si/*in*	A	1 sun, 70 ℃	2	11.3	13	+15.04
SiO_X/*ni*/Si/*in*	B+	Dark, 30kV positive corona charge with a distance of 25cm, 25℃	1.5	12.2	13.5	+10.66
	B-	Dark, 30kV negative corona charge with a distance of 25cm, 25℃	1.5	13.14	13.01	-1.01
	C	1 sun, 25 ℃	2	12.48	12.92	+3.48
	C5-	1 sun, 25 ℃, -ve corona (5 μA)	8	12.25	12.09	-1.31
	C5+	1 sun, 25 ℃, +ve corona (5 μA)	8	12.57	15.45	+22.93
	C2+	1 sun, 25 ℃, +ve corona (2 μA)	8	10.48	12.50	+22.93
	C8+	1 sun, 25 ℃, +ve corona (8 μA)	8	12.30	15.19	+23.45
ni/Si/*ip*	A	1 sun 70 ℃	8	3.5	4.2	+20
SiO_X/*ni*/Si/*ip*	B+	Dark, 30kV positive corona charge with a distance of 25cm, 25℃	1.5	3.78	3.84	+1.62
	B-	Dark, 30kV negative corona charge with a distance of 25cm, 25℃	1.5	4.02	3.58	-10.88
	C	1 sun, 25 ℃	12	4.38	4.33	+2.33
	C5+	1 sun, 25 ℃, +ve corona (5 μA)	12	4.10	3.98	-2.71

	C5-	1 sun, 25 ℃, -ve corona (5 μA)	12	3.88	3.53	-9.18
	C2-	1 sun, 25 ℃, -ve corona (2 μA)	12	5.37	4.31	-19.86
	C8-	1 sun, 25 ℃, -ve corona (8 μA)	12	6.45	4.96	-23.03

I now contrast the findings of this work with the current understanding of light-induced enhancement in SHJ specimens. The hydrogen-rich amorphous silicon (a-Si:H) layer plays an important role in SHJ cells, achieving excellent passivation on the c-Si surface with a thickness of only a few nm [231, 238, 239]. The passivation properties are related to the H diffusion inside the cells [239-241]. The a-Si:H(i) layer passivates the dangling bonds on the c-Si surface in two ways: (i) the deposited film provides the covalent Si-Si bonds to saturate dangling bonds during film growth [36, 222]. (ii) hydrogen atoms are released from the a-Si:H(i) layer, diffuse to the a-Si/c-Si interface and from Si-H bonds further saturating defects and improving passivation quality [242, 243]. Crystalline Si specimens coated with only a single a-Si(i) layer could suffer from surface passivation degradation at the c-Si/a-Si:H(i) interface during the light soaking [135, 244]. In the a-Si:H thin film materials, Si atoms mainly exist as the Si-H bonds and Si-Si bonds with good stability, due to the large bond energies [245-248]. Due to the disorder in the a-Si:H, the Si-Si bond lengths and angles are strained and can be broken by external energy to form Si-H bonds or be reconstructed. If the broken strained Si-Si bonds are not reconstructed, the dangling bond density of the a-Si:H film will be increased. This is referred to as the Staebler Wronski effect (SWE), mainly in the bulk of the a-Si [35, 249]. Kobayashi et al. reported the light-induced increase in efficiency in SHJ cells including an a-Si layer in 2016 [36], which contrasts with the normal SWE. An efficiency enhancement of $+0.3\%_{abs}$ was observed with 1 sun light soaking treatment at 32 ℃, and a similar enhancement was observed under forward bias treatment (+2.8 V bias, current density of 41 mA/cm^2). This abnormal photovoltaic phenomenon quickly attracted widespread attention in the photovoltaic field [35, 37, 250].

Mahtani et al. reported the improvement of the lifetime for SHJ samples only exists in the presence of doped layers during the light soaking treatment, while no enhancement is observed on the samples with only

an intrinsic amorphous layer on both sides [35]. For the intrinsic case, the light soaking causes the reduction in lifetime, and the subsequent dark annealing recovers the degradation, which correlates with the expected SWE degradation. Wright et al. reported that the application of 100-sun illumination at 200 ℃ can increase the efficiency of SHJ cells up to 0.7%abs after 30 seconds treatment, which shows that carrier concentration has an impact on the enhancement rate [37]. However, the mechanism behind light soaking enhancement in SHJ cells remains unclear. The current hypothesis is that hydrogen migrates to the a-Si:H/c-Si interface to improve surface passivation due to the electric field induced by the doped layers [136]. In SHJ cell, the a-Si:H/c-Si interface is always combined with a doped a-Si layer for selective carrier extraction [251] . During the light soaking treatment, the injection carrier will weaken the hydrogen ions bonding in the a-Si:H(i) layer and increase the concentration of the mobile hydrogen atoms. Through the built-in electric field generated by the doped layer, migration of hydrogen ions to the c-Si/a-Si(i) interface is promoted. The mobile hydrogen atoms saturate dangling bonds reducing interface states and thus recombination at the c-Si surface [35, 252].

The involvement of hydrogen seems to play an important role in these architectures but little understanding is yet available. It is possible that H dynamics are affecting the passivation observed after establishing an electric field through the doped layer. In this thesis, Chapter 5 has shown that surface polarisation can impact hydrogen migration in TOPCon architectures. Therefore, surface polarisation through corona discharge was exploited in this chapter to study the hydrogen kinetics for SHJ specimens during light soaking. Here, I present a hypothesis about the changes in the effective lifetime observed in *ni*/Si/*in* specimens with varied surface polarisation under light soaking at room temperatures. A model based on the redistribution of charged hydrogen atoms at the a-Si layer and diffusion of hydrogen atoms inside SHJ architectures under varied surface polarisation conditions is presented in Figure 58. Figure 58.a shows a band diagram simulated via Senarus TCAD (code provided by collaborator Pietro Altermatt) under illumination for no charge deposited on the oxide surface layer. Once corona charge is deposited, an electric field arises at the surface as shown in Figure 58.b. Here, I hypothesise the response of hydrogen atoms to the positive corona charge at the surface for the *ni*/Si/*in* SHJ specimen. When the positive charge is present on *in* side, redistribution of the electron and holes at the very surface of the n-doped a-Si is achieved. An excess electron concentration is created at the SiO_X/a-Si(n) interface. There, mobile H ions in the a-Si(n) would experience a drift mechanism. Consider the possible charge states of H. While it is accepted that n-Si will primarily host H^- ions, it is noted that H^- would be attracted to the SiO_X/a-Si(n) interface due to the electric field. Under illumination, it would be possible to

generate a small concentration of H^+ ions. I propose that it is such H^+ that is responsible for the changes in passivation at the a-Si(i)/Si interface. Under even a small surface electric field in the a-Si(n) layer as pictured in Figure 58.b, H^+ ions can diffuse towards the Si bulk and provide a passivating species most effective near the a-Si(i)/Si interface. Then, the interface states at the a-Si(i)/Si interface are passivated, causing an increase in the lifetime, as shown in Figure 56.a. When the positive corona current is increased, the increased intensity of electric field at the SiO_X/a-Si(n) interface leads to increased migration of H^+, which causes further improvements in lifetime as shown in Figure 57.a. When the negative charge is applied on *in* side, holes would gather at the SiO_X/a-Si(n) interface and no H^+ migration is promoted. The concentration of H^- in the a-Si(n) layer remains almost unchanged since H^- ions are the predominant species, compared with the anneal-only specimens without corona charge, which caused a similar change trend for processes C5 and $C5^-$ in Table 6. I postulate that the presence of H^+ species captured at the a-Si(i)/Si interface causes a decrease in the defect concentration.

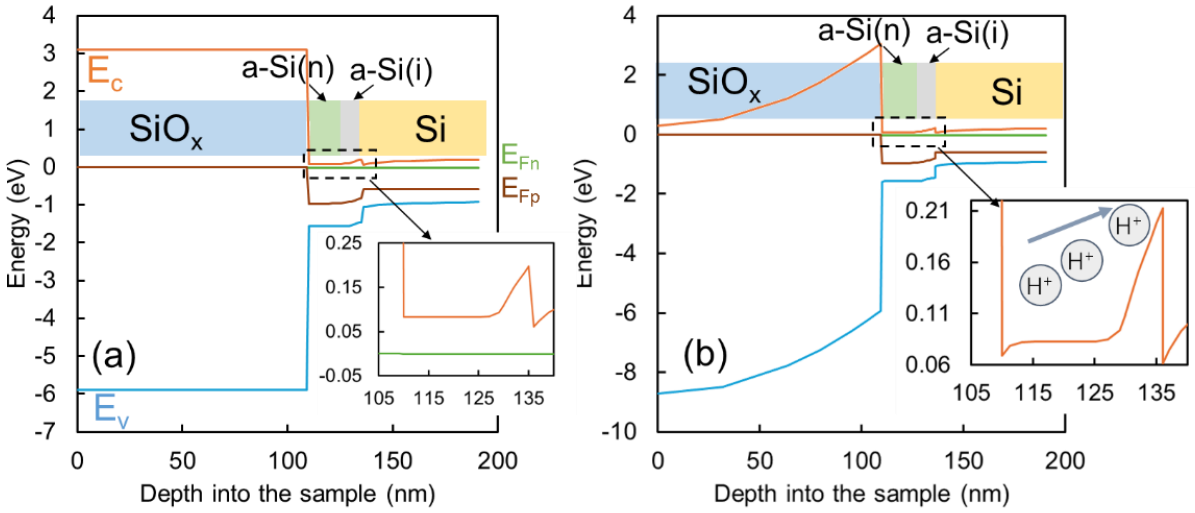

Figure 58. Schematic of band diagram and motion of hydrogen for the SHJ architecture with structure of SiO_X/a-Si(n)/a-Si(i) stack with n-type silicon substrate with varied surface polarisation under 1 Sun illumination. (a) without surface polarisation on the SiO_X film at *in* side (b) with positive corona charge on the SiO_X film at *in* side.

6.10 Summary

In this chapter, the impact of a surface electric field on the nature of the enhancement of the SHJ specimens under light soaking is investigated. It is identified that the application of the corona charge on the surface can affect the lifetime changes for SHJ specimens under 1 sun illumination at room temperature. For SHJ symmetric lifetime samples with a-Si (n) / a-Si (i) on both sides, a positive corona charge can accelerate

and enhance the improvement of the sample lifetime. In contrast, a negative charge has almost no impact on the change. For SHJ lifetime samples with a-Si (n) / a-Si (i) and a-Si (p) / a-Si (i) on different sides, negative corona charge on the *in* side will cause loss of lifetime. It is proposed that the cause of this instability is the migration of mobile hydrogen near the c-Si / s-Si(i) interface. The movement of hydrogen is controlled by the charge state of hydrogen atoms in the substrate and the applied electric field, provided by the doped layer and surface electric field. The application of the surface electric field via the corona charge method can provide insights into the role of hydrogen-induced enhancement of the SHJ architectures and further improve the lifetime of the SHJ specimens in the actual field.

Chapter 7 Summary and Future Work

7.1 Overview

Degradation in silicon solar cell architectures is a critical factor affecting the total energy yield of solar installations in the field [27, 127, 145, 191, 253]. Studying the mechanism behind these degradations and finding methods to mitigate them is essential to maintain cell efficiency and thus boost the deployment of solar energy. In this work, the mechanisms of light-induced interface-related instabilities in three different architectures (PERC, TOPCon and SHJ) are investigated, with the specific focus on surface electric fields and assessing the links to hydrogen in silicon. Current-voltage measurement and photoconductance lifetime characterisation techniques were implemented to gain a detailed understanding of the kinetics of what I proposed as hydrogen passivation/depassivation. The H migration occurs in different architectures with injected carriers via bias or illumination.

Following the application of a forward/reverse bias cycle on the PERC and TOPCon cell architectures at elevated temperatures, a bias-controlled contact resistance change is observed at the Ag/n-type Si interface for both solar cells. This is the first time such interface instabilities have been reported for a TOPCon solar cell architecture. Experimental results showed that the concentration of the interface states at the silicon/metal contact interface can be controlled by the migration of hydrogen by the electric field across the whole cell. The application of the reverse bias was able to mitigate the increased contact resistance to a certain extent. A novel model was presented that predicted the redistribution and migration of the H with different charge states across the whole cell, and the subsequent drift of the H^- ions across the silicon/metal contact interface. It was concluded that instabilities of contact resistance change in PERC are caused by the flow of charged particles, with hydrogen as the most likely candidate. The ability to mitigate the unwanted increased contact resistance in the cell presents a new avenue to understand and potentially avoid the loss of cell efficiency in solar devices both during manufacturing and in the field.

Through the application of surface electric fields, this work demonstrated that a corona charge on surface dielectric layers influenced the minority carrier lifetime in TOPCon and SHJ cell structures. The lifetime changes were investigated during light soaking treatments with varying amounts and polarities of surface electric field. It was demonstrated that the chemical passivation of the interfaces can be impacted by the

polarity and strength of the surface polarisation on the dielectric layer. For TOPCon architectures, the combination of light soaking and positive charge on the SiO_X / n-type poly-Si / SiN_x surface drastically enhances the amount of degradation, which is identified as EFID. The EFID process can lead to severe recombination losses, however, these losses can be recovered by the standard light soaking treatments. It is hypothesised that the cause of such surface-related degradation (SRD) in TOPCon is the accumulation of excessive hydrogen near the c-Si / SiO_x interface. The surface polarisation impacts the migration of the residual hydrogen ions inside the dielectric layer and the concentration gradient of hydrogen atoms causes the diffusion to the interface.

For SHJ architectures, the combination of light soaking and positive charge on the *ni* side can lead to a 23% increase in the lifetime for the *ni*/Si/*in* specimens. However, loss of lifetime for the *ni*/Si/*ip* specimen is observed when light soaking is combined with the surface polarisation on *ni* side, independent of the polarity of the electric field. It is hypothesised that the lifetime changes are due to the H^- driven to/away c-Si/a-Si layer by the doped layers. The application of the surface electric field via the corona charge enhances the drift of H ions, accelerating such processes. It can be used as a characterisation method for detecting the presence of hydrogen and further controlling its migration across different interfaces to improve the properties of the cells in the field.

Comparing the observed changes in interface properties for these three solar cell architectures allows the identification of similarities between them:

1. The instability is caused by the migration of hydrogen across different interfaces:
    (i) H^- ions to n-type Si/Ag interface caused the increased contact resistance for the PERC and TOPCon cell.
    (ii) H^- and H^0 atoms reaching the poly-Si / SiO_X/ c-Si interfaces caused the deterioration of the surface passivation for TOPCon specimens.
    (iii) H^0 atoms at a-Si:H(i) / c-Si interface led to the increase of lifetime in the presence of doped layers
2. The migration of hydrogen is controlled by the charge state and electric field across it.

A key finding in this work is that the surface electric field can not only improve passivation from field-effect (FEP) but also lead to the change of the interface chemical composition, particularly on H-induced defects. For the FEP, the application of the electric field on the surface of crystalline silicon will lead to the

repulsion of the carriers with the same polarity, which reduces carrier recombination through the improvement of carrier selectivity [57, 254]. For the chemical passivation, the recombination centres are deactivated through a chemical reaction [56, 138, 254], as discussed in Section 2.3. It is well-reported that hydrogen passivation is a highly effective chemical passivation method, yet the excess hydrogen can also cause undesirable recombination (Section 2.6). In this work, the application of the surface electric field impacted the redistribution of the holes and electrons in the dielectric layer. Further, it impacted the fraction of the concentration of hydrogen atoms with different charge states inside it. Through the potential difference caused by the concentration gradient and electric field across the cell, the migration of hydrogen atoms is achieved, and the passivation properties are affected. It was demonstrated that the application of the electric field can be an effective method to control the migration of hydrogen across different interfaces and further impact the LeTID in PERC, SRD in TOPCon, and light-induced enhancement in SHJ specimens. The method by which a surface field is controlled shows great potential to tailor hydrogen within the different interfaces in silicon systems, helping maintain high efficiency in solar cells in the field.

Additionally, the combination of the electric field and current-voltage measurement shows great potential as method to enhance current techniques for inferring hydrogen effects in silicon solar cells [138, 255-257] . Hydrogen is extremely hard to detect. There are three main methods for detecting hydrogen in crystalline silicon samples. The first is vacuum-based techniques to detect the total hydrogen concentration chemically (including secondary ion mass spectroscopy [SIMS][258, 259], atom probe tomography [260]). The second is the detection of hydrogen complexes such as hydrogen-metal, hydrogen-defect, or hydrogen dimers, typically using infrared or Raman spectroscopy [261, 262]. A third is the observation of hydrogen deactivation of dopant impurities via changes in resistivity [138, 256, 263]. The main problem for the first two approaches is sensitivity. Typical hydrogen concentrations in the bulk of silicon solar cells have been estimated between 10^{14} and 10^{15} atoms/cm^3 with at most a few per cent of this being mobile and able to participate in reactions below 200°C [257]. The normal detection limit for H in SIMS can be achieved to 10^{19} atoms/cm^3, while the use of the H isotope deuterium greatly improves the detection limit to 10^{16} atoms/cm^3 [264]. Still, very few studies have been carried out using deuterium substitution in dielectric layers. It is difficult to get samples with deuterium substitution.

Such difficulties in tracking hydrogen explain the rationale behind my use of resistance measurement to detect hydrogen inside silicon cells. Hydrogen plays a highly important role in the passivation technique and

light-induced degradation in silicon solar cells [29, 160, 254]. Characterising and controlling the concentration of hydrogen at different interfaces will lead to a better understanding and enhancement of actual devices. The application of surface electric fields via the corona charge or direct bias shows a potential good method for inferring the effects of hydrogen and controlling the kinetics of hydrogen in PV systems.

7.2 Future work

The application of surface polarisation on the different cell architectures in this work has shown promise in controlling the migration of hydrogen across the various interfaces. The properties of the lifetime specimens under the light soaking treatment with the application of surface polarisation are investigated. This work mainly focuses on the passivation stack with the n-type doped Si layer and the n-type Si substrate interface. The study of the surface polarisation on the p-type doped Si layer (emitter) side could also lead to further understanding of the hydrogen kinetics in the field.

More generally, the understanding of H at different interfaces of Si solar cells still requires a series of new experiments, including:

1. The current-voltage measurement results for the PERC specimens during bias annealing show increased contact resistance related to the charged ions with great mobilities in the cells, most likely hydrogen. However, it cannot be physically confirmed that hydrogen must be the response atoms. The repeated experiments with samples with deuterium substitution and the SIMS might confirm the actual responsible charged ions and improve the accuracy of the model.
2. The model of the hydrogen dynamics in TOPCon specimens presented focuses on the n-type poly-Si layer/ n-type Si interface. The results in the precursors without metallisation show a different trend compared with the symmetric specimen with n-type poly-Si layer. The surface polarisation test should be repeated in the symmetric specimen with p-type poly-Si layer. The passivation performance and kinetics of the charged ions in the p-type doped layer should be explored.
3. For the hydrogen migration model of the TOPCon in this work, it is hypothesised that the residual hydrogen in the dielectric layer was impacted by the surface polarisation and caused further hydrogen diffusion across the c-Si / SiO_X interface. The SiN_X layer of the TOPCon specimens after the EFID process could be etched off and deposited with the new charge-holding layer. Then, the experiment in Chapter 5 can be repeated to confirm whether the EFID effect comes from the H in

the SiN_X layer. A suitable etching method for the dielectric layer should be developed to achieve this without damaging the poly-Si layer.

4. Chapter 6 showed that surface polarisation can enhance the lifetime of SHJ specimens during light soaking, but the stability of the charge-holding of the PECVD deposited SiO_X is not good. The corona-charged ions could penetrate the pinhole of the dielectric layer and impact the doped layer. A better charge-holding dielectric layer deposition method for the SHJ specimens could be developed and the atomic layer deposition method is a viable candidate.
5. The kinetics of hydrogen in the *ni*/Si interface of SHJ specimens is investigated here. The surface polarisation test could be repeated in *pi*/Si/*ip* specimens. Then, a better understanding of the kinetics of the charged ions in SHJ specimens could be explored.

References

1. Warner, K.J. and G.A. Jones, *A population-induced renewable energy timeline in nine world regions.* Energy Policy, 2017. **101**: p. 65-76.
2. Agency, I.E., *World Energy Outlook 2017*. 2017.
3. *Statistical Review of World Energy 2023*. 2023, Energy Institute.
4. Bach, W., *Fossil fuel resources and their impacts on environment and climate.* International Journal of Hydrogen Energy, 1981. **6**(2): p. 185-201.
5. Perera, F., *Pollution from Fossil-Fuel Combustion is the Leading Environmental Threat to Global Pediatric Health and Equity: Solutions Exist.* International Journal of Environmental Research and Public Health, 2018. **15**(1): p. 16.
6. Shafiee, S. and E. Topal, *When will fossil fuel reserves be diminished?* Energy Policy, 2009. **37**(1): p. 181-189.
7. Xu, B., et al., *The environmental consequences of fossil fuels in China: National and regional perspectives.* **0**(0).
8. Wenham, S.R. and M.A. Green, *Silicon solar cells.* Progress in Photovoltaics: Research and Applications, 1996. **4**(1): p. 3-33.
9. Jackson, P., et al., *New world record efficiency for Cu(In,Ga)Se2 thin-film solar cells beyond 20%.* 2011. **19**(7): p. 894-897.
10. Aghaei, M., *A Review on Comparison between Traditional Silicon Solar Cells and Thin-Film CdTe Solar Cells*. 2012.
11. Kojima, A., et al., *Organometal Halide Perovskites as Visible-Light Sensitizers for Photovoltaic Cells.* Journal of the American Chemical Society, 2009. **131**(17): p. 6050-6051.
12. Zhou, J., et al., *Highly efficient and stable perovskite solar cells via a multifunctional hole transporting material.* Joule, 2024.
13. Wang, D., et al., *Stability of perovskite solar cells.* Solar Energy Materials and Solar Cells, 2016. **147**: p. 255-275.
14. Li, M., et al., *Recent Progress on the Stability of Perovskite Solar Cells in a Humid Environment.* The Journal of Physical Chemistry C, 2020. **124**(50): p. 27251-27266.
15. Seo, B., J.Y. Kim, and J. Chung, *Overview of global status and challenges for end-of-life crystalline silicon photovoltaic panels: A focus on environmental impacts.* Waste Management, 2021. **128**: p. 45-54.
16. Deng, R., et al., *A techno-economic review of silicon photovoltaic module recycling.* Renewable and Sustainable Energy Reviews, 2019. **109**: p. 532-550.
17. Liu, J., et al., *Review of status developments of high-efficiency crystalline silicon solar cells.* Journal of Physics D: Applied Physics, 2018. **51**(12): p. 123001.
18. *NREL Best Research-Cell efficiency chart*. Available from: https://www.nrel.gov/pv/cell-efficiency.html.
19. Dada, M. and P. Popoola, *Recent advances in solar photovoltaic materials and systems for energy storage applications: a review.* Beni-Suef University Journal of Basic and Applied Sciences, 2023. **12**(1): p. 66.

20. *Global Market Outlook For Solar Power 2023 - 2027*. 2023; Available from: https://www.solarpowereurope.org/insights/outlooks/global-market-outlook-for-solar-power-2023-2027/detail.
21. *International Technology Roadmap for Photovoltaic (ITRPV) page*. Available from: https://www.vdma.org/international-technology-roadmap-photovoltaic.
22. Aberle, A.G., *Surface passivation of crystalline silicon solar cells: a review.* Progress in Photovoltaics: Research and Applications, 2000. **8**(5): p. 473-487.
23. Dingemans, G., et al., *Influence of annealing and Al2O3 properties on the hydrogen-induced passivation of the Si/SiO2 interface.* Journal of Applied Physics, 2012. **111**(9).
24. Hyun, J.Y., et al. *Study on hydrogen passivation behavior of SiNx film and its thermal annealing effect*. in *2018 IEEE 7th World Conference on Photovoltaic Energy Conversion (WCPEC) (A Joint Conference of 45th IEEE PVSC, 28th PVSEC & 34th EU PVSEC)*. 2018.
25. Panigrahi, J. and V.K. Komarala, *Progress on the intrinsic a-Si:H films for interface passivation of silicon heterojunction solar cells: A review.* Journal of Non-Crystalline Solids, 2021. **574**: p. 121166.
26. Zhao, Y., et al., *Effects of (i)a-Si:H deposition temperature on high-efficiency silicon heterojunction solar cells.* Progress in Photovoltaics: Research and Applications, 2023. **31**(12): p. 1170-1180.
27. Wenham, A.C.n., et al. *Hydrogen-Induced Degradation*. in *2018 IEEE 7th World Conference on Photovoltaic Energy Conversion (WCPEC) (A Joint Conference of 45th IEEE PVSC, 28th PVSEC & 34th EU PVSEC)*. 2018.
28. Chen, D., et al., *Progress in the understanding of light- and elevated temperature-induced degradation in silicon solar cells: A review.* Progress in Photovoltaics: Research and Applications, 2021. **29**(11): p. 1180-1201.
29. Chen, D., et al., *Hydrogen-induced degradation: Explaining the mechanism behind light- and elevated temperature-induced degradation in n- and p-type silicon.* Solar Energy Materials and Solar Cells, 2020. **207**: p. 110353.
30. Hamer, P., et al., *Hydrogen induced contact resistance in PERC solar cells.* Solar Energy Materials and Solar Cells, 2018. **184**: p. 91-97.
31. Yang, Y., et al., *Effect of carrier-induced hydrogenation on the passivation of the poly-Si/SiOx/c-Si interface.* AIP Conference Proceedings, 2018. **1999**(1).
32. Winter, M., et al., *Degradation and Regeneration of n+-Doped Poly-Si Surface Passivation on p-Type and n-Type Cz-Si Under Illumination and Dark Annealing.* IEEE Journal of Photovoltaics, 2020. **10**(2): p. 423-430.
33. Kang, D., et al., *Firing stability of phosphorus-doped polysilicon passivating contacts: Factors affecting the degradation behavior.* Solar Energy Materials and Solar Cells, 2022. **234**: p. 111407.
34. Kang, D., et al., *Optimum Hydrogen Injection in Phosphorus-Doped Polysilicon Passivating Contacts.* ACS Applied Materials & Interfaces, 2021. **13**(46): p. 55164-55171.
35. Mahtani, P., et al., *Light induced changes in the amorphous—crystalline silicon heterointerface.* Journal of Applied Physics, 2013. **114**(12): p. 124503.
36. Kobayashi, E., et al., *Light-induced performance increase of silicon heterojunction solar cells.* Applied Physics Letters, 2016. **109**(15).
37. Wright, M., et al., *High-Intensity Illuminated Annealing of Industrial SHJ Solar Cells: A Pilot Study.* IEEE Journal of Photovoltaics, 2022. **12**(1): p. 267-273.
38. He, Q., et al., *Light soaking-induced performance enhancement in a-Si:H/c-Si heterojunction solar cells.* Science China Materials, 2022. **65**(12): p. 3513-3517.

39. Bludau, W., A. Onton, and W. Heinke, *Temperature dependence of the band gap of silicon.* 1974. **45**(4): p. 1846-1848.
40. Shockley, W. and W.T. Read, *Statistics of the Recombinations of Holes and Electrons.* Physical Review, 1952. **87**(5): p. 835-842.
41. Goetzberger, A., J. Knobloch, and B. Voß, *The Physics of Solar Cells*, in *Crystalline Silicon Solar Cells*. 2014. p. 67-86.
42. Dziewior, J. and W. Schmid, *Auger coefficients for highly doped and highly excited silicon.* Applied Physics Letters, 1977. **31**(5): p. 346-348.
43. Yablonovitch, E. and T. Gmitter, *Auger recombination in silicon at low carrier densities.* Applied Physics Letters, 1986. **49**(10): p. 587-589.
44. Hangleiter, A. and R. Häcker, *Enhancement of band-to-band Auger recombination by electron-hole correlations.* Physical Review Letters, 1990. **65**(2): p. 215-218.
45. Richter, A., et al., *Improved quantitative description of Auger recombination in crystalline silicon.* Physical Review B, 2012. **86**(16): p. 165202.
46. Altermatt, P.P., et al., *Assessment and parameterisation of Coulomb-enhanced Auger recombination coefficients in lowly injected crystalline silicon.* Journal of Applied Physics, 1997. **82**(10): p. 4938-4944.
47. Niewelt, T., et al., *Reassessment of the intrinsic bulk recombination in crystalline silicon.* Solar Energy Materials and Solar Cells, 2022. **235**: p. 111467.
48. Black, L.E. and D.H. Macdonald, *On the quantification of Auger recombination in crystalline silicon.* Solar Energy Materials and Solar Cells, 2022. **234**: p. 111428.
49. Hall, R., *Electron-Hole Recombination in Germanium.* Physical Review - PHYS REV X, 1952. **87**: p. 387-387.
50. Chen, J. and T. Sekiguchi, *Carrier Recombination Activity and Structural Properties of Small-Angle Grain Boundaries in Multicrystalline Silicon.* Japanese Journal of Applied Physics, 2007. **46**(10R): p. 6489.
51. Raghunathan, R., E. Johlin, and J.C. Grossman, *Grain Boundary Engineering for Improved Thin Silicon Photovoltaics.* Nano Letters, 2014. **14**(9): p. 4943-4950.
52. Faughnan, B. and A.C. Ipri, *A study of hydrogen passivation of grain boundaries in polysilicon thin-film transistors.* IEEE Transactions on Electron Devices, 1989. **36**(1): p. 101-107.
53. Smirnov, A.D. and V.V. Kalaev, *Analysis of impurity transport and deposition processes on the furnace elements during Cz silicon growth.* Journal of Crystal Growth, 2009. **311**(3): p. 829-832.
54. Hideo, O., et al. *Quantifying yield impact of polishing induced defect on the silicon surface*. in *2009 IEEE/SEMI Advanced Semiconductor Manufacturing Conference*. 2009.
55. Liu, A., S.P. Phang, and D. Macdonald, *Gettering in silicon photovoltaics: A review.* Solar Energy Materials and Solar Cells, 2022. **234**: p. 111447.
56. Bonilla, R.S., et al., *Dielectric surface passivation for silicon solar cells: A review.* physica status solidi (a), 2017. **214**(7): p. 1700293.
57. Aber, et al., *Field effect passivation of high efficiency silicon solar cells.* Solar Energy Materials and Solar Cells, 1993. **29**(2): p. 175-182.
58. Lüdemann, R., *Hydrogen passivation of multicrystalline silicon solar cells.* Materials Science and Engineering: B, 1999. **58**(1): p. 86-90.
59. Bauer, G., *Absolutwerte der optischen Absorptionskonstanten von Alkalihalogenidkristallen im Gebiet ihrer ultravioletten Eigenfrequenzen.* Annalen der Physik, 2006. **411**: p. 434-464.

60. Kim, Y.T., J.Y. Cho, and J. Heo, *Formation of antireflection structures for silicon in near-infrared region using AlOx/TiOx bilayer and SiNx single-layer.* Journal of Non-Crystalline Solids, 2018. **489**: p. 22-26.
61. Han, S., et al., *Comparison of different approaches to texturing monocrystalline silicon wafers for solar cell applications.* Surface Science, 2024. **748**: p. 122540.
62. Schmidt, J., et al., *Advances in the Surface Passivation of Silicon Solar Cells.* Energy Procedia, 2012. **15**: p. 30-39.
63. Jan, S., K. Mark, and C. Andrés, *Surface passivation of silicon solar cells using plasma-enhanced chemical-vapour-deposited SiN films and thin thermal SiO2/plasma SiN stacks.* Semiconductor Science and Technology, 2001. **16**(3): p. 164.
64. Hiller, D., et al., *Structural Properties of Al–O Monolayers in SiO2 on Silicon and the Maximization of Their Negative Fixed Charge Density.* ACS Applied Materials & Interfaces, 2018. **10**(36): p. 30495-30505.
65. Matsunaga, K., et al., *First-Principles Calculations of Intrinsic Defects in Al2O3.* Phys. Rev. B, 2003. **68**.
66. Dingemans, G., et al., *Effective passivation of Si surfaces by plasma deposited SiOx/a-SiNx:H stacks.* Applied Physics Letters, 2011. **98**(22).
67. Bonilla, R.S., F. Woodcock, and P.R. Wilshaw, *Very low surface recombination velocity in n-type c-Si using extrinsic field effect passivation.* Journal of Applied Physics, 2014. **116**(5).
68. Bonilla, R.S., et al., *Corona Charge in SiO2: Kinetics and Surface Passivation for High Efficiency Silicon Solar Cells.* Energy Procedia, 2016. **92**: p. 326-335.
69. Schofthaler, M., et al. *High-quality surface passivation by corona-charged oxides for semiconductor surface characterization*. in *Proceedings of 1994 IEEE 1st World Conference on Photovoltaic Energy Conversion - WCPEC (A Joint Conference of PVSC, PVSEC and PSEC)*. 1994.
70. Shahin, M.M., *Mass ‐Spectrometric Studies of Corona Discharges in Air at Atmospheric Pressures.* The Journal of Chemical Physics, 1966. **45**(7): p. 2600-2605.
71. Chapin, D.M., C.S. Fuller, and G.L. Pearson, *A New Silicon p ‐n Junction Photocell for Converting Solar Radiation into Electrical Power.* Journal of Applied Physics, 1954. **25**(5): p. 676-677.
72. Kim, K., et al., *Record high efficiency of screen-printed silicon aluminum back surface field solar cell: 20.29%*. Japanese Journal of Applied Physics, 2017. **56**: p. 08MB25.
73. Shockley, W. and H.J. Queisser, *Detailed Balance Limit of Efficiency of p ‐n Junction Solar Cells.* Journal of Applied Physics, 1961. **32**(3): p. 510-519.
74. Glunz, S.W., *High-Efficiency Crystalline Silicon Solar Cells.* Advances in OptoElectronics, 2007. **2007**: p. 097370.
75. Battaglia, C., A. Cuevas, and S. De Wolf, *High-efficiency crystalline silicon solar cells: status and perspectives.* Energy & Environmental Science, 2016. **9**(5): p. 1552-1576.
76. *Trina Solar achieves 24.5% efficiency for 210 mm p-type PERC solar cell*. 2022; Available from: https://www.pv-magazine.com/2022/07/13/trina-solar-achieves-24-5-efficiency-for-210-mm-p-type-perc-solar-cell/.
77. Blakers, A., *Development of the PERC Solar Cell.* IEEE Journal of Photovoltaics, 2019. **9**(3): p. 629-635.
78. Allen, T.G., et al., *Passivating contacts for crystalline silicon solar cells.* Nature Energy, 2019. **4**(11): p. 914-928.

79. Feldmann, F., et al., *Passivated rear contacts for high-efficiency n-type Si solar cells providing high interface passivation quality and excellent transport characteristics.* Solar Energy Materials and Solar Cells, 2014. **120**: p. 270-274.
80. Yousuf, H., et al. *Tunnel Oxide Deposition Techniques and Their Parametric Influence on Nano-Scaled SiOx Layer of TOPCon Solar Cell: A Review*. Energies, 2022. **15**, DOI: 10.3390/en15155753.
81. Glunz, S.W., et al., *Silicon-based passivating contacts: The TOPCon route.* Progress in Photovoltaics: Research and Applications, 2023. **31**(4): p. 341-359.
82. Chen, R., et al., *24.58% efficient commercial n-type silicon solar cells with hydrogenation.* Progress in Photovoltaics: Research and Applications, 2021. **29**(11): p. 1213-1218.
83. *JinkoSolar's High-efficiency N-Type Monocrystalline Silicon Solar Cell Sets New Record with Maximum Conversion Efficiency of 26.89%*. 2023; Available from: https://www.prnewswire.com/news-releases/jinkosolars-high-efficiency-n-type-monocrystalline-silicon-solar-cell-sets-new-record-with-maximum-conversion-efficiency-of-26-89-301971256.html.
84. Peibst, R., et al., *Working principle of carrier selective poly-Si/c-Si junctions: Is tunnelling the whole story?* Solar Energy Materials and Solar Cells, 2016. **158**: p. 60-67.
85. Haase, F., et al., *Laser contact openings for local poly-Si-metal contacts enabling 26.1%-efficient POLO-IBC solar cells.* Solar Energy Materials and Solar Cells, 2018. **186**: p. 184-193.
86. Lin, H., et al., *Silicon heterojunction solar cells with up to 26.81% efficiency achieved by electrically optimized nanocrystalline-silicon hole contact layers.* Nature Energy, 2023. **8**(8): p. 789-799.
87. Glunz, S.W. and F. Feldmann, *SiO2 surface passivation layers – a key technology for silicon solar cells.* Solar Energy Materials and Solar Cells, 2018. **185**: p. 260-269.
88. De Wolf, S., et al., *High-efficiency Silicon Heterojunction Solar Cells: A Review.* 2012. **2**(1): p. 7-24.
89. Ballif, C., et al., *Status and perspectives of crystalline silicon photovoltaics in research and industry.* Nature Reviews Materials, 2022. **7**(8): p. 597-616.
90. Spear, W.E. and P.G. Le Comber, *Substitutional doping of amorphous silicon.* Solid State Communications, 1975. **17**(9): p. 1193-1196.
91. Fazal, M.A. and S. Rubaiee, *Progress of PV cell technology: Feasibility of building materials, cost, performance, and stability.* Solar Energy, 2023. **258**: p. 203-219.
92. Olsson, N.A., M.C. Richardson, and J. Hevelone. *Thin film PID field failures and root cause determination*. in *2014 IEEE 40th Photovoltaic Specialists Conference (PVSC) Volume 2*. 2014.
93. Bothe, K., R. Hezel, and J. Schmidt, *Recombination-enhanced formation of the metastable boron–oxygen complex in crystalline silicon.* Applied Physics Letters, 2003. **83**(6): p. 1125-1127.
94. Hashigami, H., Y. Itakura, and T. Saitoh, *Effect of illumination conditions on Czochralski-grown silicon solar cell degradation.* Journal of Applied Physics, 2003. **93**(7): p. 4240-4245.
95. Xi, X., et al., *Investigation of fast light-induced degradation of crystal silicon solar cells under the irradiation of a high-intensity monochromatic LED light source.* Journal of Renewable and Sustainable Energy, 2017. **9**(5).
96. Glunz, S.W., et al., *Minority carrier lifetime degradation in boron-doped Czochralski silicon.* Journal of Applied Physics, 2001. **90**(5): p. 2397-2404.
97. Wolny, F., et al., *Light Induced Degradation and Regeneration of High Efficiency Cz PERC Cells with Varying Base Resistivity.* Energy Procedia, 2013. **38**: p. 523-530.
98. Payne, D.N.R., et al., *Rapid passivation of carrier-induced defects in p-type multi-crystalline silicon.* Solar Energy Materials and Solar Cells, 2016. **158**: p. 102-106.

99. Herguth, A., C. Derricks, and D. Sperber, *A Detailed Study on Light-Induced Degradation of Cz-Si PERC-Type Solar Cells: Evidence of Rear Surface-Related Degradation.* IEEE Journal of Photovoltaics, 2018. **8**(5): p. 1190-1201.
100. Bredemeier, D., et al., *Understanding the Light-induced Lifetime Degradation and Regeneration in Multicrystalline Silicon.* Energy Procedia, 2016. **92**: p. 773-778.
101. Hallam, B., et al., *Eliminating Light-Induced Degradation in Commercial p-Type Czochralski Silicon Solar Cells.* Applied Sciences, 2018. **8**(1): p. 10.
102. Herguth, A., et al. *A New Approach to Prevent the Negative Impact of the Metastable Defect in Boron Doped CZ Silicon Solar Cells*. in *2006 IEEE 4th World Conference on Photovoltaic Energy Conference*. 2006.
103. Bredemeier, D., et al., *Impact of Hydrogen-Rich Silicon Nitride Material Properties on Light-Induced Lifetime Degradation in Multicrystalline Silicon.* physica status solidi (RRL) – Rapid Research Letters, 2019. **13**(8): p. 1900201.
104. Ramspeck, K., et al., *Light Induced Degradation of Rear Passivated mc-Si Solar Cells.* Proc. 27th Eur. Photovoltaic Solar Energy Conf., 2012: p. 861-865.
105. Chen, D., et al., *Evidence of an identical firing-activated carrier-induced defect in monocrystalline and multicrystalline silicon.* Solar Energy Materials and Solar Cells, 2017. **172**: p. 293-300.
106. Winter, M., et al., *Light-induced lifetime degradation effects at elevated temperature in Czochralski-grown silicon beyond boron-oxygen-related degradation.* Solar Energy Materials and Solar Cells, 2019. **201**: p. 110060.
107. Niewelt, T., et al., *Understanding the light-induced degradation at elevated temperatures: Similarities between multicrystalline and floatzone p-type silicon.* Progress in Photovoltaics: Research and Applications, 2018. **26**(8): p. 533-542.
108. Sperber, D., A. Herguth, and G. Hahn, *A 3-state defect model for light-induced degradation in boron-doped float-zone silicon.* physica status solidi (RRL) – Rapid Research Letters, 2017. **11**(3): p. 1600408.
109. Sio, H.C., et al., *Light and elevated temperature induced degradation in p-type and n-type cast-grown multicrystalline and mono-like silicon.* Solar Energy Materials and Solar Cells, 2018. **182**: p. 98-104.
110. Chen, D., et al., *Hydrogen induced degradation: A possible mechanism for light- and elevated temperature- induced degradation in n-type silicon.* Solar Energy Materials and Solar Cells, 2018. **185**: p. 174-182.
111. Madumelu, C., et al., *Investigation of light-induced degradation in N-Type silicon heterojunction solar cells during illuminated annealing at elevated temperatures.* Solar Energy Materials and Solar Cells, 2020. **218**: p. 110752.
112. Schmidt, J., D. Bredemeier, and D.C. Walter, *On the Defect Physics Behind Light and Elevated Temperature-Induced Degradation (LeTID) of Multicrystalline Silicon Solar Cells.* IEEE Journal of Photovoltaics, 2019. **9**(6): p. 1497-1503.
113. Kersten, F., et al., *Degradation of multicrystalline silicon solar cells and modules after illumination at elevated temperature.* Solar Energy Materials and Solar Cells, 2015. **142**: p. 83-86.
114. Ciesla, A., et al., *A case study on accelerated light- and elevated temperature-induced degradation testing of commercial multi-crystalline silicon passivated emitter and rear cell modules.* Progress in Photovoltaics: Research and Applications, 2021. **29**(11): p. 1202-1212.
115. Winter, M., et al., *Light and elevated temperature induced degradation and recovery of gallium-doped Czochralski-silicon solar cells.* Scientific Reports, 2022. **12**(1): p. 8089.

116. Grant, N.E., et al., *Gallium-Doped Silicon for High-Efficiency Commercial Passivated Emitter and Rear Solar Cells.* Solar RRL, 2021. **5**(4): p. 2000754.
117. Kwapil, W., et al., *Influence of Dopant Elements on Degradation Phenomena in B- and Ga-Doped Czochralski-Grown Silicon.* Solar RRL, 2021. **5**(5): p. 2100147.
118. Lin, D., et al., *Investigation on the light and elevated temperature induced degradation of gallium-doped Cz-Si.* Solar Energy, 2021. **225**: p. 407-411.
119. Winter, M., D.C. Walter, and J. Schmidt, *Carrier Lifetime Degradation and Regeneration in Gallium- and Boron-Doped Monocrystalline Silicon Materials.* IEEE Journal of Photovoltaics, 2021. **11**(4): p. 866-872.
120. Eberle, R., et al., *Impact of the firing temperature profile on light induced degradation of multicrystalline silicon.* physica status solidi (RRL) – Rapid Research Letters, 2016. **10**(12): p. 861-865.
121. Varshney, U., et al., *Evaluating the Impact of SiN_x Thickness on Lifetime Degradation in Silicon.* IEEE Journal of Photovoltaics, 2019. **9**(3): p. 601-607.
122. Sen, C., et al., *Eliminating light- and elevated temperature-induced degradation in P-type PERC solar cells by a two-step thermal process.* Solar Energy Materials and Solar Cells, 2020. **209**: p. 110470.
123. Mäckel, H. and P.P. Altermatt, *Current Transport Through Lead–Borosilicate Interfacial Glass Layers at the Screen–Printed Silver-Silicon Front Contact.* IEEE Journal of Photovoltaics, 2015. **5**(4): p. 1034-1046.
124. Chan, C., et al., *Instability of Increased Contact Resistance in Silicon Solar Cells Following Post-Firing Thermal Processes.* Solar RRL, 2017. **1**(11): p. 1700129.
125. Sopori, B.L., et al., *Hydrogen in silicon: A discussion of diffusion and passivation mechanisms.* Solar Energy Materials and Solar Cells, 1996. **41-42**: p. 159-169.
126. Yang, Y., et al., *Effect of carrier-induced hydrogenation on the passivation of the poly-Si/SiOx/c-Si interface.* AIP Conference Proceedings, 2018. **1999**(1): p. 040026.
127. Kang, D., et al., *Long-term stability study of the passivation quality of polysilicon-based passivation layers for silicon solar cells.* Solar Energy Materials and Solar Cells, 2020. **215**: p. 110691.
128. Chen, D., et al., *Investigating the degradation behaviours of n+-doped Poly-Si passivation layers: An outlook on long-term stability and accelerated recovery.* Solar Energy Materials and Solar Cells, 2022. **236**: p. 111491.
129. Hollemann, C., et al., *Firing stability of tube furnace-annealed n-type poly-Si on oxide junctions.* Progress in Photovoltaics: Research and Applications, 2022. **30**(1): p. 49-64.
130. Sperber, D., et al., *Bulk and surface instabilities in boron doped float-zone samples during light induced degradation treatments.* Energy Procedia, 2017. **124**: p. 794-798.
131. Hamer, P., D. Chen, and R.S. Bonilla, *Thermal Processes and their Impact on Surface-Related Degradation.* physica status solidi (RRL) – Rapid Research Letters, 2022. **16**(2): p. 2100464.
132. Hamer, P., et al., *Modelling of hydrogen transport in silicon solar cell structures under equilibrium conditions.* 2018. **123**(4): p. 043108.
133. Liu, D., et al., *Observations of contact resistance in TOPCon and PERC solar cells.* Solar Energy Materials and Solar Cells, 2022. **246**: p. 111934.
134. Al-Dhahir, I., et al., *The influence of surface electric fields on the chemical passivation of Si-SiO2 interfaces after firing.* AIP Conference Proceedings, 2022. **2487**(1).
135. Kobayashi, E., et al., *Light-induced performance increase of silicon heterojunction solar cells.* Applied Physics Letters, 2016. **109**(15): p. 153503.

136. Cattin, J., et al., *Influence of Light Soaking on Silicon Heterojunction Solar Cells With Various Architectures.* IEEE Journal of Photovoltaics, 2021. **11**(3): p. 575-583.
137. Hoex, B., et al., *Silicon surface passivation by atomic layer deposited Al2O3.* Journal of Applied Physics, 2008. **104**(4).
138. Hallam, B.J., et al., *Development of advanced hydrogenation processes for silicon solar cells via an improved understanding of the behaviour of hydrogen in silicon.* Progress in Photovoltaics: Research and Applications, 2020. **28**(12): p. 1217-1238.
139. Beyer, W., et al., *Comparative study of hydrogen evolution from amorphous hydrogenated silicon films.* Thin Solid Films, 1982. **90**(2): p. 145-152.
140. Lucovsky, G., et al., *Properties of bonded hydrogen in hydrogenated amorphous silicon and other hydrogenated amorphous silicon alloys.* Journal of Non-Crystalline Solids, 1995. **182**(1): p. 90-102.
141. Pearton, S.J., J.W. Corbett, and T.S. Shi, *Hydrogen in crystalline semiconductors.* Applied Physics A, 1987. **43**(3): p. 153-195.
142. Estreicher, S.K., J.L. Hastings, and P.A. Fedders, *Hydrogen-defect interactions in Si.* Materials Science and Engineering: B, 1999. **58**(1): p. 31-35.
143. Johnson, N.M., *Mechanism for hydrogen compensation of shallow-acceptor impurities in single-crystal silicon.* Physical Review B, 1985. **31**(8): p. 5525-5528.
144. Lee, S.H., et al., *Review of advanced hydrogen passivation for high efficient crystalline silicon solar cells.* Materials Science in Semiconductor Processing, 2018. **79**: p. 66-73.
145. Krugel, G., et al., *Impact of Hydrogen Concentration on the Regeneration of Light Induced Degradation.* Energy Procedia, 2011. **8**: p. 47-51.
146. Nampalli, N., et al., *Evidence for the role of hydrogen in the stabilization of minority carrier lifetime in boron-doped Czochralski silicon.* Applied Physics Letters, 2015. **106**(17).
147. Hallam, B.J., et al., *Hydrogen Passivation of B-O Defects in Czochralski Silicon.* Energy Procedia, 2013. **38**: p. 561-570.
148. Duerinckx, F. and J. Szlufcik, *Defect passivation of industrial multicrystalline solar cells based on PECVD silicon nitride.* Solar Energy Materials and Solar Cells, 2002. **72**(1): p. 231-246.
149. Herring, C., N.M. Johnson, and C.G. Van de Walle, *Energy levels of isolated interstitial hydrogen in silicon.* Physical Review B, 2001. **64**(12): p. 125209.
150. Pearton, S.J., et al., *Hydrogen Passivation of Oxygen Donors in Si.* MRS Online Proceedings Library, 1985. **59**(1): p. 475-480.
151. Huang, Y.L., et al., *Hydrogen diffusion at moderate temperatures in p-type Czochralski silicon*. Vol. 96. 2004.
152. Fedders, P.A., *Diffusion of hydrogen in different charge states in realistic models of a-Si: H*. Vol. 66. 2002.
153. Branz, H., et al., *Fermi-level dependence of the charge state of diffusing hydrogen in amorphous silicon*. Vol. 299-302. 2002. 191-195.
154. Sun, C., F.E. Rougieux, and D. Macdonald, *A unified approach to modelling the charge state of monatomic hydrogen and other defects in crystalline silicon.* Journal of Applied Physics, 2015. **117**(4).
155. Johnson, N.M., *Electric field dependence of hydrogen neutralization of shallow‐acceptor impurities in single‐crystal silicon.* Applied Physics Letters, 1985. **47**(8): p. 874-876.
156. Rizk, R., et al., *Hydrogen diffusion and passivation processes in p- and n-type crystalline silicon.* Physical Review B, 1991. **44**(12): p. 6141-6151.
157. Zhu, X., et al., *Quantification of characteristic parameters for the dissociation kinetics of iron–boron pairs in Czochralski silicon.* Scripta Materialia, 2011. **64**(3): p. 217-220.

158. Haller, E.E., *Hydrogen in crystalline semiconductors.* Semiconductor Science and Technology, 1991. **6**(2): p. 73-84.
159. Kersten, F., et al., *System performance loss due to LeTID.* Energy Procedia, 2017. **124**: p. 540-546.
160. Liu, D., et al., *Investigating the link between LeTID and hydrogen induced contact resistance in PERC devices.* AIP Conference Proceedings, 2022. **2487**(1).
161. Sheoran, M., A. Upadhyaya, and A. Rohatgi, *Bulk lifetime and efficiency enhancement due to gettering and hydrogenation of defects during cast multicrystalline silicon solar cell fabrication.* Solid-State Electronics, 2008. **52**(5): p. 612-617.
162. Dingemans, G., et al., *Hydrogen induced passivation of Si interfaces by Al2O3 films and SiO2/Al2O3 stacks.* Applied Physics Letters, 2010. **97**(15).
163. Chan, C.E., et al., *Rapid Stabilization of High-Performance Multicrystalline P-type Silicon PERC Cells.* IEEE Journal of Photovoltaics, 2016. **6**(6): p. 1473-1479.
164. Bredemeier, D., et al., *Lifetime degradation and regeneration in multicrystalline silicon under illumination at elevated temperature.* AIP Advances, 2016. **6**(3).
165. Murphy, E.L. and R.H. Good, *Thermionic Emission, Field Emission, and the Transition Region.* Physical Review, 1956. **102**(6): p. 1464-1473.
166. Sperber, D., A. Herguth, and G. Hahn, *Instability of Dielectric Surface Passivation Quality at Elevated Temperature and Illumination.* Energy Procedia, 2016. **92**: p. 211-217.
167. Green, M.A., *The Passivated Emitter and Rear Cell (PERC): From conception to mass production.* Solar Energy Materials and Solar Cells, 2015. **143**: p. 190-197.
168. Feldmann, F., et al., *Industrial TOPCon Solar Cells Realized by a PECVD Tube Process*. 2020.
169. Chang, J.S., P.A. Lawless, and T. Yamamoto, *Corona discharge processes.* IEEE Transactions on Plasma Science, 1991. **19**(6): p. 1152-1166.
170. Xu, X., et al., *A comparison of structures and properties of SiNx and SiOx films prepared by PECVD.* Journal of Non-Crystalline Solids, 2012. **358**(1): p. 99-106.
171. Mazzarella, L., et al. *Optimization of PECVD process for ultra-thin tunnel SiOx film as passivation layer for silicon heterojunction solar cells*. in *2016 IEEE 43rd Photovoltaic Specialists Conference (PVSC)*. 2016.
172. Sigmond, R.S., *Simple approximate treatment of unipolar space‐charge‐dominated coronas: The Warburg law and the saturation current.* Journal of Applied Physics, 1982. **53**(2): p. 891-898.
173. Elmquist, R.E., A.M. Jeffery, and D.G. Jarrett, *Characterization of four-terminal-pair resistance standards: a comparison of measurements and theory.* IEEE Transactions on Instrumentation and Measurement, 2001. **50**(2): p. 267-271.
174. Naem, A.A. and D.A. Smith, *Accuracy of the Four‐Terminal Measurement Techniques for Determining Contact Resistance.* Journal of The Electrochemical Society, 1986. **133**(11): p. 2377.
175. Heaney, M., *Electrical Conductivity and Resistivity*. 2003. p. 7-1 to 7.
176. Guo, S., et al., *Detailed investigation of TLM contact resistance measurements on crystalline silicon solar cells.* Solar Energy, 2017. **151**: p. 163-172.
177. Berger, H.H., *Contact Resistance and Contact Resistivity.* Journal of The Electrochemical Society, 1972. **119**(4): p. 507.
178. *Contact Resistance and Schottky Barriers*, in *Semiconductor Material and Device Characterization*. 2005. p. 127-184.
179. Zisman, W.A., *A NEW METHOD OF MEASURING CONTACT POTENTIAL DIFFERENCES IN METALS.* Review of Scientific Instruments, 1932. **3**(7): p. 367-370.

180. Kelvin, L., *V. Contact electricity of metals.* The London, Edinburgh, and Dublin Philosophical Magazine and Journal of Science, 1898. **46**(278): p. 82-120.
181. Baikie, et al., *Noise and the Kelvin method.* Review of Scientific Instruments, 1991.
182. Sinton, R.A., A. Cuevas, and M. Stuckings, *Quasi-steady-state photoconductance, a new method for solar cell material and device characterization.* Conference Record of the Twenty Fifth IEEE Photovoltaic Specialists Conference - 1996, 1996: p. 457-460.
183. Klein, D., F. Wuensch, and M. Kunst, *The determination of charge-carrier lifetime in silicon.* physica status solidi (b), 2008. **245**(9): p. 1865-1876.
184. Sinton, R.A. and A. Cuevas, *Contactless determination of current‐voltage characteristics and minority‐carrier lifetimes in semiconductors from quasi‐steady‐state photoconductance data.* Applied Physics Letters, 1996. **69**(17): p. 2510-2512.
185. Cuevas, A. and R.A. Sinton, *Prediction of the open-circuit voltage of solar cells from the steady-state photoconductance.* Progress in Photovoltaics: Research and Applications, 1997. **5**(2): p. 79-90.
186. Janssen, G.J.M., et al., *Extraction of Recombination Properties from Lifetime Data.* Energy Procedia, 2016. **92**: p. 88-95.
187. Trupke, T., et al., *Photoluminescence imaging of silicon wafers.* Applied Physics Letters, 2006. **89**(4).
188. Trupke, T., et al., *Photoluminescence Imaging for Photovoltaic Applications.* Energy Procedia, 2012. **15**: p. 135-146.
189. Bredemeier, D., et al., *Impact of Hydrogen‐Rich Silicon Nitride Material Properties on Light‐Induced Lifetime Degradation in Multicrystalline Silicon.* physica status solidi (RRL) - Rapid Research Letters, 2019. **13**: p. 1900201.
190. Sen, C., et al., *Eliminating light-and elevated temperature-induced degradation in P-type PERC solar cells by a two-step thermal process.* Solar Energy Materials and Solar Cells, 2020. **209**: p. 110470.
191. Ning, L., L. Song, and J. Zhang, *Research progress of light and elevated temperature-induced degradation in silicon solar cells: A review.* Journal of Alloys and Compounds, 2022. **912**: p. 165120.
192. Hamer, P., et al., *A novel source of atomic hydrogen for passivation of defects in silicon.* physica status solidi (RRL) – Rapid Research Letters, 2017. **11**(5): p. 1600448.
193. Schön, J., et al., *Hydrogen in Silicon Solar Cells: The Role of Diffusion.* Solar RRL. **n/a**(n/a): p. 2400668.
194. Yli-Koski, M., et al., *Low-temperature dark anneal as pre-treatment for LeTID in multicrystalline silicon.* Solar Energy Materials and Solar Cells, 2019. **192**: p. 134-139.
195. Pritchard, R., et al., *Hydrogen molecules in boron-doped crystalline silicon.* Semiconductor Science and Technology, 1999. **14**: p. 77.
196. Voronkov, V.V. and R. Falster, *Formation, dissociation, and diffusion of various hydrogen dimers in silicon.* physica status solidi (b), 2017. **254**(6): p. 1600779.
197. Hamer, P., et al., *Modelling of hydrogen transport in silicon solar cell structures under equilibrium conditions.* Journal of Applied Physics, 2018. **123**(4): p. 043108.
198. Chan, C., et al., *Instability of Increased Contact Resistance in Silicon Solar Cells Following Post-Firing Thermal Processes.* 2017. **1**(11): p. 1700129.
199. Peral, A., et al., *Impact of Extended Contact Cofiring on Multicrystalline Silicon Solar Cell Parameters.* IEEE Journal of Photovoltaics, 2017. **7**(1): p. 91-96.
200. Hammann, B., et al., *The Impact of Different Hydrogen Configurations on Light- and Elevated-Temperature- Induced Degradation.* IEEE Journal of Photovoltaics, 2023. **13**(2): p. 224-235.
201. Dieter, K.S., *Contact Resistance and Schottky Barriers*, in *Semiconductor Material and Device Characterization*. 2006, IEEE. p. 127-184.

202. Hamer, P., et al., *Hydrogen passivation mechanisms in silicon solar cells.* Proc. 28th Eur. Photovoltaic Sol. Energy Conf. Exhib., 2013: p. 982-987.
203. Lahti, A., et al., *Polycrystalline silicon, a molecular dynamics study: II. Grains, grain boundaries and their structure.* Modelling and Simulation in Materials Science and Engineering, 2024. **32**(6): p. 065026.
204. Wang, L., et al. *Suppression of LeTID in P type multi crystalline PERC silicon solar cells by biased annealing process*. in *11th International Conference on Crystalline Silicon Photovoltaics*. 2021. AIP Conference Proceedings.
205. Chen, D., et al., *24.58% total area efficiency of screen-printed, large area industrial silicon solar cells with the tunnel oxide passivated contacts (i-TOPCon) design.* Solar Energy Materials and Solar Cells, 2020. **206**: p. 110258.
206. Kane, D.E. and D. Swanson, *Measurement of the Emitter Saturation Current by a Contactless Photoconductivity Decay Method.* Conference Record of the IEEE Photovoltaic Specialists Conference, 1985: p. 578-583.
207. Ushasree, P.M. and B. Bora, *Silicon Solar Cells*, in *Solar Energy Capture Materials*, E.A. Gibson, Editor. 2019, The Royal Society of Chemistry. p. 0.
208. Green, M.A., *The path to 25% silicon solar cell efficiency: History of silicon cell evolution.* Progress in Photovoltaics: Research and Applications, 2009. **17**(3): p. 183-189.
209. Liu, Z.-b., et al., *Effect of firing process on electrical properties and efficiency of n-TOPCon solar cells.* Solar Energy, 2024. **267**: p. 112205.
210. Sekar, S., et al., *A Critical Review of The Process and Challenges of Silicon Crystal Growth for Photovoltaic Applications.* Crystal Research and Technology, 2024. **59**(1): p. 2300131.
211. Padhamnath, P., et al., *Impact of firing temperature on fire-through metal contacts to P-doped (n+) and B-doped (p+) poly-Si.* Solar Energy Materials and Solar Cells, 2021. **230**: p. 111217.
212. Höffler, H., et al., *Enlarged firing window and efficiency boosting of PERC solar cells by 'laser enhanced contact optimization' (LECO).* AIP Conference Proceedings, 2022. **2487**(1).
213. Dullweber, T. and J. Schmidt, *Industrial Silicon Solar Cells Applying the Passivated Emitter and Rear Cell (PERC) Concept—A Review.* IEEE Journal of Photovoltaics, 2016. **6**(5): p. 1366-1381.
214. Hallam, B., et al., *The role of hydrogenation and gettering in enhancing the efficiency of next-generation Si solar cells: An industrial perspective.* physica status solidi (a), 2017. **214**(7): p. 1700305.
215. Jensen, M.A., et al., *Evaluating root cause: The distinct roles of hydrogen and firing in activating light- and elevated temperature-induced degradation.* Journal of Applied Physics, 2018. **124**(8).
216. Varshney, U., et al., *Evaluating the Impact of SiNx Thickness on Lifetime Degradation in Silicon.* IEEE Journal of Photovoltaics, 2019. **9**(3): p. 601-607.
217. Kersten, F., J. Heitmann, and J.W. Müller, *Influence of Al2O3 and SiNx Passivation Layers on LeTID.* Energy Procedia, 2016. **92**: p. 828-832.
218. Sperber, D., et al., *Degradation of Surface Passivation on Crystalline Silicon and Its Impact on Light-Induced Degradation Experiments.* IEEE Journal of Photovoltaics, 2017. **7**(6): p. 1627-1634.
219. Kim, K., et al., *Degradation of Surface Passivation and Bulk in p-Type Monocrystalline Silicon Wafers at Elevated Temperature.* IEEE Journal of Photovoltaics, 2019. **9**(1): p. 97-105.
220. Sen, C., et al., *Impact of surface doping profile and passivation layers on surface-related degradation in silicon PERC solar cells.* Solar Energy Materials and Solar Cells, 2022. **235**: p. 111497.
221. Mehler, M., et al., *Delay of Regeneration by Adding Aluminum in Boron-Doped Crystalline Si.* physica status solidi (a), 2021. **218**(22): p. 2100603.

222. Steingrube, S., et al., *Interpretation of recombination at c-Si/SiNx interfaces by surface damage.* Journal of Applied Physics, 2010. **108**(1).
223. Fritz, J.M., et al., *Temperature dependent degradation and regeneration of differently doped mc-Si materials.* Energy Procedia, 2017. **124**: p. 718-725.
224. Fertig, F., et al., *Stability of the regeneration of the boron–oxygen complex in silicon solar cells during module integration.* Solar Energy Materials and Solar Cells, 2013. **115**: p. 189-198.
225. Niewelt, T., et al., *Degradation of Crystalline Silicon Due to Boron–Oxygen Defects.* IEEE Journal of Photovoltaics, 2017. **7**(1): p. 383-398.
226. Burgelman, M., P. Nollet, and S. Degrave, *Modelling polycrystalline semiconductor solar cells.* Thin Solid Films, 2000. **361-362**: p. 527-532.
227. Bonilla, R.S., et al., *Enhancing dielectric-silicon interfaces through surface electric fields during firing.* Solar Energy Materials and Solar Cells, 2024. **269**: p. 112799.
228. Hollemann, C., et al., *Changes in hydrogen concentration and defect state density at the poly-Si/SiOx/c-Si interface due to firing.* Solar Energy Materials and Solar Cells, 2021. **231**: p. 111297.
229. Tavendale, A., D. Alexiev, and A. Williams, *Field drift of the hydrogen‐related, acceptor‐neutralizing defect in diodes from hydrogenated silicon.* Applied Physics Letters, 1985. **47**: p. 316-318.
230. Johnson, N. and C. Herring, *Diffusion of negatively charged hydrogen in silicon.* Physical review. B, Condensed matter, 1993. **46**: p. 15554-15557.
231. De Wolf, S., C. Ballif, and M. Kondo, *Kinetics of a-Si:H bulk defect and a-Si:H/c-Si interface-state reduction.* Physical Review B, 2012. **85**(11): p. 113302.
232. Branz, H.M., et al., *Fermi-level dependence of the charge state of diffusing hydrogen in amorphous silicon.* Journal of Non-Crystalline Solids, 2002. **299-302**: p. 191-195.
233. Chau, T.T., S.R. Mejia, and K.C. Kao, *The effects of deposition temperature on properties of SiO2 films fabricated by a new electron cyclotron resonance microwave plasma-enhanced chemical-vapor deposition process.* Canadian Journal of Physics, 1991. **69**(3-4): p. 165-169.
234. Pan, Y., et al., *Optical Constant and Conformality Analysis of SiO2 Thin Films Deposited on Linear Array Microstructure Substrate by PECVD.* Coatings, 2021. **11**(5): p. 510.
235. Pankove, J.I. and M.L. Tarng, *Amorphous silicon as a passivant for crystalline silicon.* Applied Physics Letters, 1979. **34**(2): p. 156-157.
236. Nagata, H., et al., *Effect of substrate heating on elimination of pinholes in sputtering deposited SiO2 films on LiNbO3 single crystal substrates.* Thin Solid Films, 1998. **335**(1): p. 117-121.
237. Reusch, M., et al., *Fill Factor Limitation of Silicon Heterojunction Solar Cells by Junction Recombination.* Energy Procedia, 2013. **38**: p. 297-304.
238. Balaji, P., et al., *Improving surface passivation on very thin substrates for high efficiency silicon heterojunction solar cells.* Solar Energy Materials and Solar Cells, 2020. **216**: p. 110715.
239. Lozac'h, M., et al., *Passivation property of ultrathin SiOx:H / a-Si:H stack layers for solar cell applications.* Solar Energy Materials and Solar Cells, 2018. **185**: p. 8-15.
240. Ruan, T., et al., *Achieving high efficiency silicon heterojunction solar cells by applying high hydrogen content amorphous silicon as epitaxial-free buffer layers.* Thin Solid Films, 2020. **711**: p. 138305.
241. Sun, C., et al., *Origins of hydrogen that passivates bulk defects in silicon heterojunction solar cells.* Applied Physics Letters, 2019. **115**(25).
242. Soman, A., et al., *Correlation between in Situ Diagnostics of the Hydrogen Plasma and the Interface Passivation Quality of Hydrogen Plasma Post-Treated a-Si:H in Silicon Heterojunction Solar Cells.* ACS Applied Materials & Interfaces, 2019. **11**(17): p. 16181-16190.

243. Wu, Z., et al., *Role of hydrogen in modifying a-Si:H/c-Si interface passivation and band alignment for rear-emitter silicon heterojunction solar cells.* Journal of Materials Science: Materials in Electronics, 2020. **31**(12): p. 9468-9474.
244. Stuckelberger, M., et al., *Comparison of amorphous silicon absorber materials: Light-induced degradation and solar cell efficiency*. Journal of Applied Physics, 2013. **114**(15).
245. Wehrspohn, R.B., et al., *Relative importance of the Si–Si bond and Si–H bond for the stability of amorphous silicon thin film transistors.* Journal of Applied Physics, 2000. **87**(1): p. 144-154.
246. Ling, S., et al., *A computational study of Si－H bonds as precursors for neutral E′ centres in amorphous silica and at the Si/SiO2 interface.* Microelectronic Engineering, 2013. **109**: p. 310-313.
247. Toneva, A., T. Marinova, and V. Krastev, *XPS investigation of a-Si:H thin films after light soaking.* Journal of Luminescence, 1998. **80**(1): p. 455-459.
248. Street, R.A., et al., *Hydrogen diffusion in amorphous silicon.* Philosophical Magazine B, 1987. **56**(3): p. 305-320.
249. Staebler, D.L. and C.R. Wronski, *Reversible conductivity changes in discharge‐produced amorphous Si.* Applied Physics Letters, 1977. **31**(4): p. 292-294.
250. Gageot, T., et al., *Improvement of silicon heterojunction module efficiency using fast illumination post-treatments.* Solar Energy Materials and Solar Cells, 2023. **257**: p. 112395.
251. Wang, F., et al., *Silicon solar cells with bifacial metal oxides carrier selective layers.* Nano Energy, 2017. **39**: p. 437-443.
252. De Wolf, S. and M. Kondo, *Nature of doped a-Si:H/c-Si interface recombination.* Journal of Applied Physics, 2009. **105**(10).
253. Peters, I.M., et al., *The Value of Efficiency in Photovoltaics.* Joule, 2019. **3**(11): p. 2732-2747.
254. Muduli, S.P. and P. Kale, *State-of-the-art passivation strategies of c-Si for photovoltaic applications: A review.* Materials Science in Semiconductor Processing, 2023. **154**: p. 107202.
255. Herguth, A. and C. Winter, *Methodology and Error Analysis of Direct Resistance Measurements Used for the Quantification of Boron–Hydrogen Pairs in Crystalline Silicon.* IEEE Journal of Photovoltaics, 2021. **11**(4): p. 1059-1068.
256. Winter, C., J. Simon, and A. Herguth, *Study on Boron–Hydrogen Pairs in Bare and Passivated Float-Zone Silicon Wafers.* physica status solidi (a), 2021. **218**(23): p. 2100220.
257. Walter, D.C., et al., *Easy-to-apply methodology to measure the hydrogen concentration in boron-doped crystalline silicon.* Solar Energy Materials and Solar Cells, 2019. **200**: p. 109970.
258. Schnabel, M., et al., *Hydrogen passivation of poly-Si/SiOx contacts for Si solar cells using Al2O3 studied with deuterium.* Applied Physics Letters, 2018. **112**(20).
259. Lehmann, M., et al., *Analysis of hydrogen distribution and migration in fired passivating contacts (FPC).* Solar Energy Materials and Solar Cells, 2019. **200**: p. 110018.
260. Pal, S., et al., *Quantification of hydrogen in nanostructured hydrogenated passivating contacts for silicon photovoltaics combining SIMS-APT-TEM: A multiscale correlative approach.* Applied Surface Science, 2021. **555**: p. 149650.
261. Liu, S., et al., *Raman Spectroscopy for the Competition of Hydrogen Bonds in Ternary (H2O–THF–DMSO) Aqueous Solutions.* Molecules, 2019. **24**(20): p. 3666.
262. Haryanto, A., et al., *In situ infrared, Raman and X-ray spectroscopy for the mechanistic understanding of hydrogen evolution reaction.* Journal of Energy Chemistry, 2024. **90**: p. 632-651.
263. Capizzi, M. and A. Mittiga, *Hydrogen in Si: Diffusion and shallow impurity deactivation.* Physica B+C, 1987. **146**(1): p. 19-29.

264. Stevie, F.A., et al., *SIMS measurement of hydrogen and deuterium detection limits in silicon: Comparison of different SIMS instrumentation.* Journal of Vacuum Science & Technology B, 2016. **34**(3).

Appendix

Optimisation of Low-temperature PECVD recipe

In this section, the other three processing parameters (the gas ratio, chamber pressure and RF power) were varied to be optimised from the standard recipe. Each recipe had only one parameter changed, as shown in Table 7. Table 7 summarises all the tested recipes and Figure 59 shows the thickness and the charge-holding ability of all the deposited SiO_X layers with these recipes. For each deposition, 4 cm × 4 cm specimens from group 72 were used.

Table 7 Low temperature PECVD SiO_X recipes

Recipe	**Group**	**Silane (SiH_4) flow rate (sccm)**	**Nitrous Oxide (N_2O) flow rate (sccm)**	**Pressure (mTorr)**	**RF power (W)**	**T (℃)**	**Time (min)**
Standard		170	710	1000	20	350	1 min 51 s
RF power test							
1	72A	170	710	1000	20	200	1 min 51 s
2		170	710	1000	40	200	1 min 51 s
3		170	710	1000	80	200	1 min 51 s
80 W RF power							
4	72 B	120	760	1000	80	200	1 min 51 s
5		150	730	1000	80	200	1 min 51 s
3		170	710	1000	80	200	1 min 51 s
6		200	680	1000	80	200	1 min 51 s
7		250	630	1000	80	200	1 min 51 s
8		300	580	1000	80	200	1 min 51 s
9	72C	120	760	1200	80	200	1 min 51 s
10		150	730	900	80	200	1 min 51 s
11		170	710	800	80	200	1 min 51 s
20 W RF power							
12	72 D	120	760	1000	80	200	1 min 51 s
13		150	730	1000	80	200	1 min 51 s
14		170	710	1000	80	200	1 min 51 s
15		200	680	1000	80	200	1 min 51 s
16		250	630	1000	80	200	1 min 51 s
17		300	580	1000	80	200	1 min 51 s
18	72E	200	680	800	80	200	1 min 51 s

19		200	680	900	80	200	1 min 51 s
20		200	680	1100	80	200	1 min 51 s
21		200	680	1200	80	200	1 min 51 s
Optimisation							
22	72F	150	730	1000	80	200	70.75 s
23		170	710	1000	80	200	65.45 s
24		200	680	1000	80	200	57.65 s
25		150	730	1200	80	200	70.75 s
26		170	710	1200	80	200	65.45 s
27		200	680	1200	80	200	57.65 s
28		120	760	1000	20	200	70.75 s
29		150	730	1000	20	200	65.45 s
30		170	710	1000	20	200	57.65 s
31		120	760	800	20	200	70.75 s
32		150	730	800	20	200	65.45 s
33		170	710	800	20	200	57.65 s

I varied RF power at first. 20 W RF power shows the best stability of charge holding, while 80 W RF power shows the biggest amount of charge holding. Considering the stability of the passivation layer at 200 ℃ and the charge-holding ability, 20 W and 80 W RF power are used for further tests.

Then I varied the gas ratio and pressure with constant RF power.

For the recipes with the 80W RF power:

a) Gas ratio with recipe 5 (150 sccm of SiH_4 and 730 sccm of N_2O) leads to the biggest change in PCD
b) Pressure with 1200 mTorr leads to the biggest change in PCD

For the recipes with the 20W RF power:

a) Gas ratio with recipe 12 (120 sccm of SiH_4 and 760 sccm of N_2O) leads to the biggest change in PCD
b) Pressure with 800 mTorr leads to the biggest change in PCD

In the end, I combined all these parameters to get the best recipe. Recipe 28 shows a good ability for charge holding and the best stability of the charge storage among all the recipes, identified as the recipe A in Table 5. Recipe 28 shows the best ability for charge holding and a good stability of the charge storage among all the recipes, identified as the recipe B in Table 5.

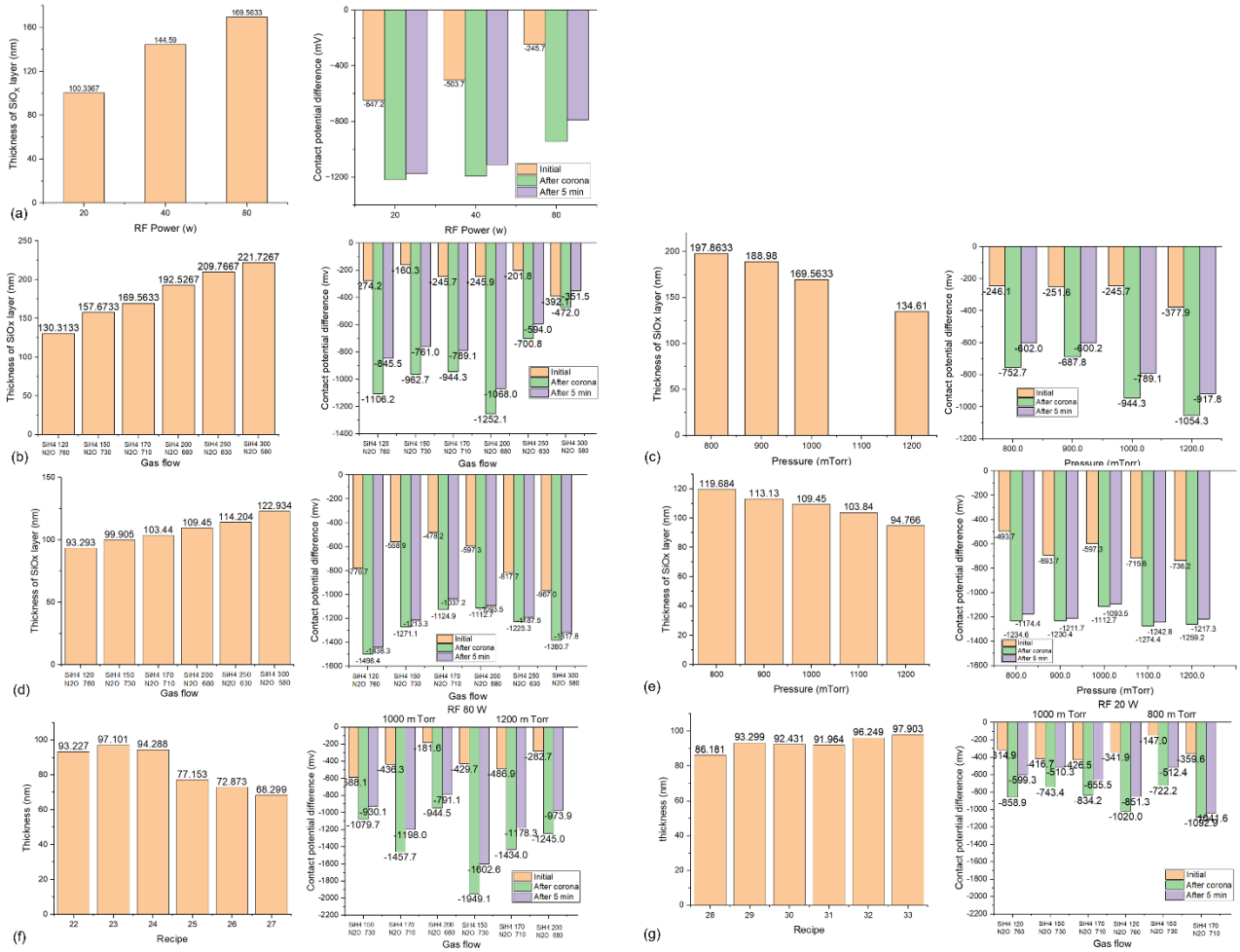

Figure 59. The thickness and charge-holding ability of PECVD SiO_X with different recipes. (a) Recipes 1-3 with different RF power and the application of constant gas ratio and pressure. (b) Recipes 4-8 with different gas ratio and the application of 80W RF power and constant pressure. (c) Recipes 9-11 with different pressure and the application of 80W RF power and constant gas ratio. (d) Recipes 12-17 with different gas ratio and the application of 80W RF power and constant pressure. (e) Recipes 18-21 with different pressure and the application of 80W RF power and constant gas ratio. (f) Recipes 22-27 with optimisation of gas ratio and pressure for 80W RF power. (g) Recipes 28-33 with optimisation of gas ratio and pressure for 80W RF power.